A study of particles-flow interactions based on the numerical solution of the Boltzmann equation

Citation for published version (APA):
Livi, C. (2023). *A study of particles-flow interactions based on the numerical solution of the Boltzmann equation*. [Phd Thesis 1 (Research TU/e / Graduation TU/e), Applied Physics and Science Education]. Eindhoven University of Technology.

Document status and date:
Published: 19/04/2023

Document Version:
Publisher’s PDF, also known as Version of Record (includes final page, issue and volume numbers)

Please check the document version of this publication:

• A submitted manuscript is the version of the article upon submission and before peer-review. There can be important differences between the submitted version and the official published version of record. People interested in the research are advised to contact the author for the final version of the publication, or visit the DOI to the publisher's website.
• The final author version and the galley proof are versions of the publication after peer review.
• The final published version features the final layout of the paper including the volume, issue and page numbers.

Link to publication

General rights
Copyright and moral rights for the publications made accessible in the public portal are retained by the authors and/or other copyright owners and it is a condition of accessing publications that users recognise and abide by the legal requirements associated with these rights.

- Users may download and print one copy of any publication from the public portal for the purpose of private study or research.
- You may not further distribute the material or use it for any profit-making activity or commercial gain
- You may freely distribute the URL identifying the publication in the public portal.

If the publication is distributed under the terms of Article 25fa of the Dutch Copyright Act, indicated by the “Taverne” license above, please follow below link for the End User Agreement:

www.tue.nl/taverne

Take down policy
If you believe that this document breaches copyright please contact us at:

openaccess@tue.nl

providing details and we will investigate your claim.

Download date: 04. Oct. 2023

A study of particles-flow interactions based on the numerical solution of the Boltzmann Equation

Cosimo Livi

This research was supported by the Netherlands Organization for scientific research (NWO-TTW in Dutch), Grant No. 15376. The use of supercomputing facilities (Snellius) was supported by the SURF Cooperative, Grant No. 2021.035.

Copyright © 2023, Cosimo Livi
All rights reserved

Cover designed by Cosimo Livi
Printed by Persephone Edizioni - Italy

A catalogue record is available from the Eindhoven University of Technology library
ISBN: 978-90-386-5718-9
NUR: 925

A study of particles-flow interactions based on the numerical solution of the Boltzmann Equation

PROEFSCHRIFT

ter verkrijging van de graad van doctor aan de Technische Universiteit
Eindhoven, op gezag van de rector magnificus prof.dr.ir. F.P.T. Baaijens, voor
een commissie aangewezen door het College voor Promoties, in het openbaar
te verdedigen op woensdag 19 april 2023 om 13:30 uur

door

Cosimo Livi

geboren te Bagno a Ripoli, Italië

Dit proefschrift is goedgekeurd door de promotoren en de samenstelling van de promotiecommissie is als volgt:

Voorzitter:	prof.dr.ir. G. M. W. Kroesen
1e promotor:	prof.dr. F. Toschi,
2e promotor:	prof.dr. H. J. H. Clercx
leden:	prof.dr.ir. E. H. van Brummelen
	prof.dr.ir. C. R. Kleijn (Universiteit Delft)
	dr. A. Lyulin
	prof. dr. A. L. Garcia (San José State University)
adviseur:	dr. G. Di Staso

Het onderzoek of ontwerp dat in dit proefschrift wordt beschreven is uitgevoerd in overeenstemming met de TU/e Gedragscode Wetenschapsbeoefening.

Contents

1 Introduction 7

2 Theoretical Background 15

2.1 The Boltzmann Equation 15
2.2 From the microscopic to the macroscopic description 18
2.3 Surface interactions in the continuum and low Reynolds number regime 23
2.4 Surface interactions in the free-molecular regime 31
2.5 From the continuum to the free molecular limits: the transition regime 41
2.6 Concluding remarks 44

3 Numerical Methods 47

3.1 Introduction to the LBM and DSMC methods: analogies and differences 47
3.2 Basics of the LBM 50
3.3 Fluid-surface interactions in the LBM: no-slip conditions for particle-transport algorithm 60
3.4 Basics of the DSMC method 65
3.5 Fluid-surface interactions in the DSMC: boundary conditions and cut-cell method 69
3.6 Concluding remarks 73
3.7 Appendix A: lattice weights and Hermite Polynomials 75
3.8 Appendix B: Two-way coupled representation of ellipsoidal particles 76

4 Influence of numerical resolution on the dynamics of finite-size particles with the Lattice Boltzmann Method 81

4.1 Introduction 82
4.2 Adaptive boundary conditions to simulate Stokes settling 84
  4.2.1 Accuracy as a function of the simulation box size at fixed resolution 86
  4.2.2 Convergence analysis and velocity fluctuations 90
  4.2.3 Complete Interpolation: sub-grid particle simulations and accuracy 92
4.3 Rotational dynamics of a spheroidal particle in a shear flow 94
4.4 Concluding remarks 102

4.5 Appendix A: recovering effects of inertia at finite Reynolds numbers 104

5 Drag and lift coefficients of ellipsoidal particles under rarefied flow conditions with the DSMC method 109

5.1 Introduction 110
5.2 Validation of the cut-cell algorithm 114
5.3 Drag correlations for ellipsoidal particles at finite Knudsen number . 117
5.4 Predictive model for the Drag and Lift coefficients 121
5.5 Concluding remarks 128
5.6 Appendix A: accuracy scaling of the cut-cell algorithm 130

6 Extension of drag model for ellipsoidal particles in complex scenarios 133

6.1 Introduction 134
6.2 Effects of the aspect ratio and gas-surface interactions at finite Knudsen number 136
6.3 Drag corrections from near-wall effects 146
6.4 Concluding remarks 151
6.5 Appendix A 152

7 Concluding remarks and outlook 155

7.1 Conclusions 155
7.2 Outlook 158

Bibliography 161

Curriculum Vitae 170

List of publications and conferences 171

Acknowledgments 173

Chapter 1

Introduction

Nano- and micro-particle and droplet transport phenomena in complex flows are crucial for many environmental [1, 2], industrial [3–9] and medical applications [10–12]. This class of particles can be released or suspended in fluids due to a large variety of causes during materials production, handling, processing, and during machine operations. Their release into the environment is often unintentional and/or undesired and, in many cases, the suspending fluid is a gas. For example, submicron-sized particles are released in the ambient air in large scale production processes involving different materials (rubbers, plastic and paints) and from the use of fossil fuel, becoming a major contribution to air pollution. In the semiconductor industry, with its extreme requirements, contamination from submicron particles is a major challenge, and a large effort is dedicated to improve modelling capabilities and fundamental understanding of the dynamics of suspended particles. Macroscopic gas properties such as viscosity and density are often not affected by the presence of these particles due to their small size and relatively low volume loading in gases.

Particularly relevant for the scope of this thesis work are applications related to the emerging high-tech industry: in [3] the problem of contamination from particles during vacuum-loss in ITER, the new experimental reactor for nuclear fusion research, is addressed; in [5, 6] the authors investigate the phenomena of back-flows of particles from thrusters of satellites, which creates pollution or damages to the thruster nozzle. In [7–9] the effects from contamination from particle debris in modern lithography systems are discussed. In the latter case contamination from nanoparticles is particularly important as the latest technology lithography scanner systems have entered High-Volume Manufacturing. This technology uses 13.5nm Extreme Ultra Violet (EUV) radiation, which is transmitted and focused through a hydrogen background gas at near-vacuum conditions. The hydrogen gas can be excited into a low-density plasma due to the interactions with the EUV light and the complex interactions between solid surfaces, gas and plasma can lead to the release of particulate and molecular contamination. Such contaminant release can have a negative impact on product quality and productivity, leading to significant economic impact. An example of a typical particle contaminant that is found in modern lithography machines is shown in Fig. 1.1, where

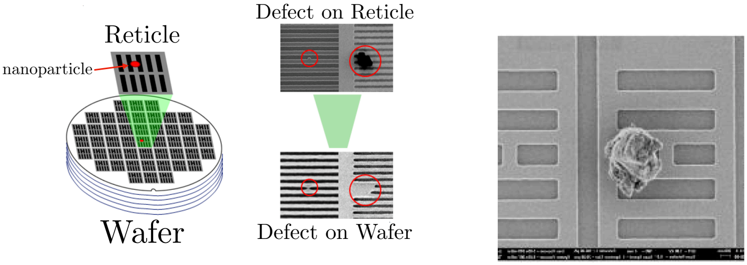

Figure 1.1: On the left side: sketch of a particle debris that reached the reticle of a lithography machine, where the feature to imprint on the wafer is located. The presence of the particle on the reticle leads to multiple defect printing on the wafer [9]. On the right, field picture of real debris nanoparticle on the reticle [8].

also a sketch of the effects of particle contamination on the reticle and the wafer is presented.

Another relevant source of contamination is the EUV source itself [13]. The 13.5nm light is, in fact, obtained via complex high-energy interactions between a high-power infrared laser and tin droplets. The fundamental physical processes behind such interactions are still not well understood and represent an active research topic [14–19]. In very few words, the incoming infra-red radiation quickly warms up the tin droplet, generating a hot and dense plasma whose emission spectrum is centered at the desired 13.5nm wave length required to imprint the small features of commercial microchips. During the irradiation process, some of the high-energy tin residuals can enter in the low-pressure chamber where the light is guided and focalized to the wafer, creating sources of defects (see Fig. 1.1).

In modern lithography systems, gas flows are used to protect sensitive regions from particle contamination and range from continuum to rarefied conditions. The spectrum of physical regimes is, thus, extremely wide and there is a continuous effort from the scientific community to improve the mathematical and numerical modeling required to accurately describe the transport of contaminant in such a variety of conditions. In this context, the main aim of this thesis work is to develop advanced numerical techniques that contribute to improved modelling and prediction of the transport of particles in a wide range of applications, from continuum to rarefied flows. Since the numerical methods developed in this work, as well as their mathematical foundations, will be extensively described in the following chapters, in this Chapter we will provide a bird-eye overview about some of the mathematical models commonly used to describe flows ranging from continuum to rarefied conditions.

Gas flows are traditionally classified accordingly to the so-called Knudsen number, which represents a measure of the departure from the local thermodynamic equilibrium typical of continuum flows. The Knudsen number is defined as the ratio between a molecular length scale, i.e. the mean free path, λ, and a characteristic flow-related length scale, L:

$$Kn = \frac{\lambda}{L}. \tag{1.1}$$

Depending on the value of this dimensionless parameter, gas flows are typically classified in continuum ($Kn < 0.01$), slip ($0.01 < Kn \leq 0.1$), transition ($0.1 < Kn < 10$) and free molecular ($Kn \geq 10$) regimes. In continuum flows, we can imagine that for each element of fluid (which evolution in time and space is described by the macroscopic equations) there are a large amount of molecules and that local thermodynamic equilibrium is preserved. More precisely, the fluid element must be preserved, in terms of its constituent molecules, during the typical lengths and time scales of the investigated phenomenon. This allows to derive macroscopic laws, embodied by the Navier-Stokes Equations (NSE), that describe the evolution in time and space of the fluid elements. In low pressure environments, however, a further degree of complexity arises as rarefaction and non-equilibrium effects have to be taken into account. In such conditions, more fundamental approaches based on a kinetic description of gases must be used to properly capture the physical phenomena that appear when departing from the continuum case. While for continuum flows, in fact, the standard Navier-Stokes (NS) level of description is proven to be an adequate model to describe the dynamics of the macroscopic properties of the flow (such as density, velocity and pressure), when rarefaction effects are larger than a certain threshold, it is not possible anymore to describe the higher order moments, such as the shear stresses and the heat flux, in terms of the lower-order macroscopic quantities. This leads to the impossibility to have a closed set of conservation equations and, thus, defines the validity limits of the continuum description. When such condition is met, it is required to adopt a lower level of description based on the solution of the Boltzmann Equation (BE). The BE describes the fundamental physics in the whole range of Kn, but it is extremely complex to solve both analytically and numerically to the point that some analytical solutions can be obtained only for very simple cases in the free-molecular regime (i.e. when the fluid is so diluted that inter-molecular collisions are absent).

From a numerical point of view, it is typically unpractical or inaccurate to describe the whole spectrum of Kn-based regimes with a single model, and different techniques must be employed accordingly to the regime of interest. A graphical representation of the discussed physical regimes, as well as some numerical techniques typically employed for gas flow simulations are presented in Fig. 1.2.

The two main categories of solvers can be identified as continuous and particle-based. To the first group belong all the approaches that solve a system of partial differential equations (PDEs) describing the evolution of the macroscopic flow fields in time

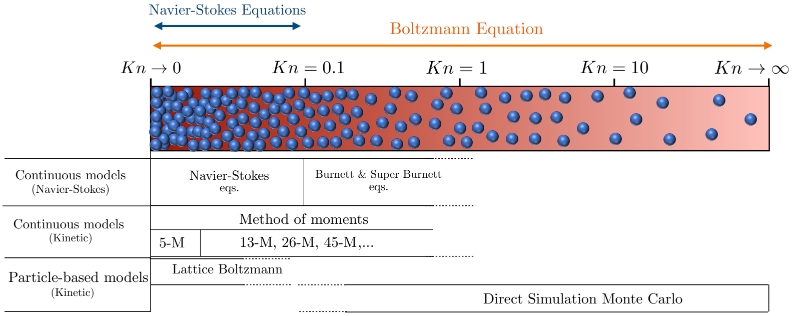
Navier-Stokes Equations
Boltzmann Equation
$Kn \to 0$
$Kn = 0.1$
$Kn = 1$
$Kn = 10$
$Kn \to \infty$
Continuous models (Navier-Stokes)
Navier-Stokes eqs.
Burnett & Super Burnett eqs.
Continuous models (Kinetic)
Method of moments
5-M
13-M, 26-M, 45-M,...
Particle-based models (Kinetic)
Lattice Boltzmann
Direct Simulation Monte Carlo

Figure 1.2: Schematic representation of the mathematical and numerical methods (with their validity limits) used to model various regimes of gas flows. Rarefaction effects, quantified by the dimensionless parameter Kn, can be related to an increase in the mean free path of the gas molecules to the point that it becomes comparable, or larger, than the typical macroscopic length-scale of the system and the Navier-Stokes Equation cease to be valid. In such regimes, solvers based on the solution of the Boltzmann Equation (as the DSMC method) must be employed. Figure is adapted with permission from [20].

and space. To the second group belong, instead, methods that directly model the dynamics of a collection of microscopic molecules, and the macroscopic properties of the gas flows are derived from averages or integrals of the dynamics of individual particles. Solvers based on the continuous NSE (such as finite-elements [21] and finite-volume [22] solvers) fall in the first category and cannot be safely extended beyond the slip-flow regime. Some advancement in this sense can be obtained via the Burnett and Super Burnett models [23–25], which represent, from a theoretical point of view, the governing macroscopic equations in the transition regime. The Burnett Equations are, however, not widely used for a number of reasons, including that no proper boundary conditions are known and they are unstable for transient problems [26].

Continuous approaches can also include kinetic models, i.e. models based on the solution of the BE. A prominent example in this sense is the Method of Moments [27], which attempts to solve additional transport equations for the stress and heat flux variables. This is done by coupling systems of equations involving an increasing number of moments of the BE (the meaning of this will be explained in Chapter 2). The Method of Moments is actively developed by the scientific community [28–30] as it represents a promising approach to model rarefied flows. Since the number of moments to be included quickly rises with the rarefaction levels [27], this method becomes numerically less feasible for increasing Kn.

When dealing with particle-based solvers, the Lattice-Boltzmann method (LBM) and the Direct Simulation Monte Carlo (DSMC) are among the most relevant approaches. The former is an efficient BE solver that is mostly used in the low Kn regime as it formally recovers the NSE, while the latter is the de-facto standard to model rarefied flows as it correctly describes dilute gas flows in all regimes, but becomes computationally unfeasible for low values of Kn. Since the entirety of Chapter 3 will be dedicated to the description of these two approaches, we will omit their discussion here.

This thesis specifically focuses on the development of different numerical methods to address the interactions between flows and solid particles under various flow conditions based on the Lattice-Boltzmann (for continuum and near-continuum flows) and the Direct Simulation Monte Carlo (for highly rarefied flows) methods. The reason of this choice is related not only to the predisposition of these numerical approaches to describe arbitrary shaped solid particles (avoiding complicated meshing of their surface), but also because they are both based on the numerical solution of the discretized BE. This aspect is particularly desirable in relation to the possibility of developing a hybrid LBM-DSMC solver that includes the dynamics of fully-resolved particles. The possibility to couple the two solvers has, in fact, been successfully addressed by Di Staso [20, 31, 32], showing that it is possible to efficiently increase the LBM capabilities in modelling flows with increasing rarefaction by dedicating a portion of the gas volume to DSMC calculation. A natural outlook of this work would then be (as discussed in the Conclusions Chapter) to include a particle transport algorithm to the LBM-DSMC hybrid solver.

More specifically, in this work we aim to address the following research questions:

- **Mesh-free uniform approach for flow-particle interactions:** we aim to develop a framework to describe two-way coupled particle-flow interactions in the LBM and DSMC which is based on a common mathematical and numerical approach. Such approach does not involve constant re-meshing of the surface of the particle, facilitating the future development of hybrid kinetic solvers that include particle transport algorithms.

- **Investigate accuracy of LBM particle transport algorithms in dynamics conditions:** in the framework of the LBM various boundary treatments are available which offer different degrees of accuracy. While many benchmarks are available in the literature featuring static particles in different flows, it is still unclear what accuracy is expected when particles can move in the fluid domain. This difficulty is partially related to the absence of a clear benchmark for dynamic conditions. We aim to provide such benchmark to investigate and improve moving boundary treatment in the LBM.

- **Improve Euler-Lagrangian Point Particles simulations of non-spherical particles in rarefied conditions:** in many practical applications particles are orders of magnitude smaller than the geometry of the flow and are typically modelled as spherical point particles transported in the flow. In these conditions rarefaction effects are dominant on the drag of the particles and, currently, only drag corrections for spherical particles are available for the whole range of Kn. We will adopt the DSMC method to derive drag corrections on different ellipsoidal particles, including complex aspect ratios with shapes close to needles and disks.

The thesis is organized as follows: in Chapter 2 we cover the fundamental theory behind gas flow modelling, starting from the derivation of the BE to its connection to the macroscopic models represented by the Navier-Stokes Equations via the so-called transfer equation. In this framework, we also cover the basic theory of interactions between flows and solid particles, focusing on the continuum and free molecular regimes, showing some fundamental analytical results. Through this chapter it will become evident how flow-particle interactions in the transition regime are the most difficult to model, as analytical solutions are not available and the typical approach is to employ heuristic relations obtained experimentally.

In Chapter 3, we focus entirely on the description of the numerical methods used and developed during this thesis work, namely the Lattice-Boltzmann Method (LBM) and the Direct Simulation Monte Carlo (DSMC) method. In this context, we introduce the similarities and differences between these two BE solvers, focusing on providing the details of the respective implementations and working principles. Particular care is dedicated to the description of the numerical schemes used to model the two-way coupling between flows and solid particles, which represents the main contribution, from the numerical point of view, of this work.

Chapter 4 will be fully dedicated to the analysis performed with the LBM related to the accuracy assessment of the particle transport algorithm in Stokes flows. We propose a systematic approach, based on the development of novel boundary conditions to apply at the simulation box, to accurately estimate the degree of accuracy of the two-way coupled numerical schemes used to include solid colloidal particles in the framework of the LBM. Different boundary treatments at the fluid-solid interface are evaluated, and an improvement of existing schemes is proposed.

In Chapter 5, we transition from the LBM to the DSMC method. We employ our novel scheme to model fully-resolved colloidal particles in the DSMC algorithm to perform an aerodynamic study of drag and lift coefficients of ellipsoidal particles immersed in ambient flow in rarefied conditions. The main objective of this Chapter is to develop and discuss a methodology to obtain heuristic models that capture rarefaction effects on the drag and lift of such particles. These models are obtained via interpolation and extrapolation of DSMC results and we show that their predictions correctly recovers results from DSMC simulations in a broad range of Kn.

In Chapter 6, we further develop the discussion presented in Chapter 5 by first improving the mathematical formulation of the proposed heuristic model for the drag and lift of ellipsoidal particles in rarefied ambient flow conditions and then by extending it to particles with different aspect ratios (up to very pronounced needle or flake shapes) and gas-surface interactions. Additionally, we perform a study of the impact of the vicinity of a wall to the drag experienced by the particles. The predictive models discussed in Chapters 5 and 6 are, in fact, formally derived for particles immersed in unbounded fluid and it is important to estimate the degree of variation from the predictions when particles are instead closer to a solid surface. We show that near-wall effects take the form of a drag increase when compared to the unbounded case, but such effects quickly vanish as the particle-wall distance increases, and are weaker for increasing rarefaction. The heuristic models obtained in this study can strongly improve the accuracy and capabilities of Euler-Lagrangian point particles simulation typically employed in contamination control studies of particles transport.

Finally, in Chapter 7 we discuss and summarize our main results, underlying the possible outlooks and applications from the results presented in this thesis work.

Chapter 2

Theoretical Background

In this thesis we will rely on different numerical approaches to address the problem of flow-particle interactions, namely the Lattice-Boltzmann method (LBM) and the Direct-Simulation Monte Carlo (DSMC) method, which are both based on a numerical solution of the Boltzmann Equation (BE).

This chapter provides an introduction to the modeling of the interactions between flows and solid objects in different flow regimes, starting from the connection between the microscopic dynamics of a gas flow, based on a kinetic description, with the macroscopic variables. We will show how the BE describes the underlying physics of gas flows at any level of rarefaction. Its limiting cases, in fact, yield the continuum description, typically modeled via the Navier-Stokes Equations (NSE), and the collisionless (or free-molecular) flows. Most problems in rarefied gas dynamics involve, however, the central region of these two extremes (transition regime), which is the most challenging to address numerically, theoretically and experimentally due to the interplay of non-equilibrium effects and non-vanishing intermolecular collisions probability. In this chapter we will introduce the most common techniques to address particles-flow interactions in the transition regime, highlighting their strengths and limitations. To address the transition regime, in fact, advanced numerical techniques, such as the DSMC method, are often required due to the lack of analytical models. For this reason, the continuum and free-molecular regimes represent the most natural starting point to understanding the fundamental physics behind gas-surface interactions from a theoretical perspective.

2.1 The Boltzmann Equation

In this Section we provide a brief introduction to the physical modeling at the basis of the BE. For an in-depth derivation of the BE from the fundamental mathematical principles, we refer to the seminal textbooks of Bird [33], Cercignani [34–36] and Succi [37, 38], on which this Chapter is based.

The practical impossibility to describe a gas flow, in a classical sense, by the Newtonian equations of each individual molecule led to the necessity of a statistical descrip-

tion based on probability distributions.
In a sample of gas with N identical gas molecules, a typical molecule has a velocity $\mathbf{c}$ with components $u,\ v$ and w in the $x,\ y$ and z directions, respectively. The number of molecules dN with velocity components in the range u to $u + du$, v to $v + dv$ and w to $w + dw$ can be expressed as:

$$dN = Nf(\mathbf{c})d\mathbf{c}, \tag{2.1}$$

where $d\mathbf{c} = dudvdw$ is the volume element in the velocity space and $f(\mathbf{c})$ is the single particle distribution function. From now on, the functional statement is omitted and $f \equiv f(\mathbf{c})$. It can be easily proven that f is normalized, and that it cannot have negative values. The macroscopic properties of the gas can then be related to f by computing the average value over the desired microscopic quantity Q:

$$\overline{Q} = \frac{1}{N}\int_N QdN = \int\limits_{-\infty}^{+\infty} Qfd\mathbf{c}. \tag{2.2}$$

The rightmost integral is called a moment of the distribution function and, as it will be shown in more detail later, the macroscopic quantities are referred to as moments of the distribution function. For example, by setting $Q = \mathbf{c}$, the streaming macroscopic velocity can be computed via Eq. (2.2) as the average of the microscopic velocity $\mathbf{c}$.
In most cases of interest, it is desirable to express the explicit dependence of f with respect to position and time, as the macroscopic flow properties are usually related to these variables. Following [33], the 6-dimensional space that includes the three spatial dimensions, as well as the three velocity dimensions, is called phase space, and the single particle distribution function in phase space, $\mathcal{F}(\mathbf{c}, \mathbf{r}, t) \equiv \mathcal{F}$ can be defined as

$$dN = \mathcal{F}(\mathbf{c}, \mathbf{r}, t)d\mathbf{c}d\mathbf{r}, \tag{2.3}$$

where d$\mathbf{r} = dxdydz$ is the volume element in physical space. Now dN represents the number of molecules with velocity components in the range u to $u + du$, v to $v + dv$ and w to $w + dw$ and with spatial positions ranging from x to $x + dx$, y to $y + dy$ and z to $z + dz$. A relation between f and $\mathcal{F}$ can be easily obtained by combining Eqs. (2.1) and (2.3), and reads

$$nf = \mathcal{F}, \tag{2.4}$$

where $n = N/d\mathbf{r}$ is the gas number density. This relation must be used in cases where $f(\mathbf{c})$ is used in a context in which it also depends on the position, $\mathbf{r}$ and time, t. A straightforward application of Eq. (2.4) is the derivation of the macroscopic density field, ρ, by combining it with Eq. (2.2) and by setting $Q = m$:

$$\rho(\mathbf{r},t) = \int_{-\infty}^{+\infty} mnf d\mathbf{c} = mn(\mathbf{r},t). \tag{2.5}$$

From a rigorous point of view, the most complete level of description of a monoatomic gas composed of N indistinguishable particles is obtained by considering the $6N$ dimensional phase space and its relative N-particle distribution function $F^{(N)}$, which allows to define the probability for the whole system to be in a specific state. The statistical mechanics of such system is described by the Liouville equation [39], which expresses the conservation of $F^{(N)}$ in the $6N$ dimensional phase. However, the enormous mathematical complexity required by this description makes it impossible for practical use and the only distribution function that can have some hope to be solved is the single-particle distribution function, $F^{(1)} = \mathcal{F}/N$, which thus represents a normalized version of $\mathcal{F}$. This can be achieved by repeatedly integrating the Liouville equation in order to obtain the BBGKY [40] set of equations which, ultimately, lead to an equation for $\mathcal{F}$. This approach, however, allows to express $\mathcal{F}$ as a function of the two-particle distribution function $F^{(2)}$ and the physical assumption of *molecular chaos* must be invoked to obtain a closed equation for $\mathcal{F}$. In a dilute gas, only a small fraction of space is actually occupied by the gas molecules. Assuming that the system is in molecular chaos means that each molecule is statistically independent from the others and the probability to find them in a specific two-particle configuration is just the product of each individual molecule in their respective one particle configuration, so that

$$F^{(2)}(\mathbf{c}_1,\mathbf{r}_1,\mathbf{c}_2,\mathbf{r}_2,t) = F^{(1)}(\mathbf{c}_1,\mathbf{r}_1)F^{(1)}(\mathbf{c}_2,\mathbf{r}_2). \tag{2.6}$$

To describe the time evolution of $\mathcal{F}$ (equivalent to $NF^{(1)}$), three main aspects must be taken into account: firstly, the flow of molecules across the surface of $d\mathbf{r}$ of phase space induced by the molecular velocity $\mathbf{c}$. Additionally, the flow of molecules across the surface of $d\mathbf{c}$ as a result of the external force per unit mass $\mathbf{F}$. Finally, the in- and outflow of molecules from $d\mathbf{c}d\mathbf{r}$ due to the scattering from molecular collisions, that are assumed to be binary and instantaneous in a dilute gas.

The final form of the equation that governs the evolution of the single particle distribution function f in terms of the aforementioned microscopic interactions was firstly obtained by Ludwig Boltzmann [41] in 1872, and takes his name. The famous BE reads:

$$\frac{\partial}{\partial t}(nf) + \mathbf{c}\cdot\frac{\partial}{\partial \mathbf{r}}(nf) + \mathbf{F}\cdot\frac{\partial}{\partial \mathbf{c}}(nf) = C, \tag{2.7}$$

where the left-hand terms represent the streaming motion of the molecules in the 6-dimensional phase space and the right-hand side is the integral collision operator. Under the assumption of molecular chaos, C can be expressed as

$$C = \int\limits_{-\infty}^{+\infty} \int\limits_{0}^{4\pi} n^2 (f_1' f_2' - f_1 f_2) \mathbf{c}_r \sigma d\Omega d\mathbf{c}_1, \tag{2.8}$$

where the subscripts 1 and 2 refer to the two molecules involved in the collision, the primed quantities are the post-collisional distributions, $\mathbf{c}_r = \mathbf{c}_1 - \mathbf{c}_2$ is the relative velocity of the colliding molecules and $d\Omega$ is the unit solid angle about $\mathbf{c}_r' = \mathbf{c}_1' - \mathbf{c}_2'$. The integral form of the collision operator, in contrast with the partial differential form of the left-hand side of Eq. (2.7), is responsible for most of the mathematical and numerical complexities associated with the solution of the Boltzmann Equation.

2.2 From the microscopic to the macroscopic description

In the previous Section we showed the basic concepts behind the BE. We will now focus on its applications, showing how to derive the continuum level of description, represented by the Navier-Stokes Equations (NSE), as well as how to apply it in cases where non-equilibrium effects are so relevant that the continuum limit is not a valid model anymore.

Given any microscopic quantity, Q, which is either a constant or a function of the molecular velocity, we can compute the moments of the BE with respect to this quantity. In the same way as the moments of the distribution function, given by Eq. (2.2), allow to obtain the macroscopic properties of the gas, the moments of the BE include the conservation equations of the continuum gas dynamics. By multiplying the BE by Q and integrating in the velocity space, we obtain the so-called transfer equation:

$$\frac{\partial}{\partial t}(n\overline{Q}) + \frac{\partial}{\partial \mathbf{r}} \cdot \left(n\overline{\mathbf{c}Q}\right) - n\mathbf{F} \cdot \overline{\frac{\partial Q}{\partial \mathbf{c}}} = \Delta\left[Q\right], \tag{2.9}$$

where $\Delta\left[Q\right]$ is called the collision integral, which computation is in general very complicated. Luckily, there are quantities for which the collisional integral is zero. This happens thanks to the two symmetries associated to $\Delta\left[Q\right]$, namely the symmetry between collision partners and between post- and pre-collision velocities (see [33]). Such quantities, called collisional invariants, are the mass m, momentum $m\mathbf{c}$ and energy $\frac{1}{2}m\mathbf{c}^2$.

To compute Eq. (2.9) on the aforementioned collisional invariants, it is useful to first derive some fundamental quantities from the microscopic velocity. The first of these quantities is the macroscopic fluid density ρ obtained in Eq. (2.5). The second, then, is the *macroscopic stream velocity*, which can be obtained by separating the molecular velocity in its average (or stream) and thermal components, given by $\mathbf{u}$ and $\mathbf{c}'$, respectively:

$$\mathbf{u} = \overline{\mathbf{c}}, \tag{2.10}$$

$$\mathbf{c}' = \mathbf{c} - \mathbf{u}. \tag{2.11}$$

It is now appropriate to spend a few words about the notation used throughout this work. We introduced the microscopic velocity $\mathbf{c} = (u,\ v,\ w)$ to describe the velocity component of each individual gas molecule. When dealing with macroscopic properties, instead, we will use the typical notation $\mathbf{u} = (u_x,\ u_y,\ u_z)$, where the subscripts refer to the average velocity along the different Cartesian components. Here, some confusion might arise between the x component of the microscopic velocity, u, and the individual components of the macroscopic velocity $\mathbf{u}$. The latter, however, will always appear with the subscript associated with the Cartesian component, and we believe that the context of usage will be clear enough to avoid any misunderstanding. The next quantity of relevance is the *pressure tensor*, obtained as the momentum average over the thermal velocities:

$$\mathbf{P} = nm\overline{\mathbf{c}'\mathbf{c}'}. \tag{2.12}$$

The components of $\mathbf{P}$ are $P_{\alpha\beta} = nm\overline{c'_\alpha c'_\beta}$, where the subscripts α and β are used to represent the tensor in Einstein notation and refer to the three Cartesian components. The scalar pressure, P, is the average of the diagonal components of $\mathbf{P}$:

$$P = \frac{1}{3}\rho\left(\overline{u'^2} + \overline{v'^2} + \overline{w'^2}\right) = \frac{1}{3}\rho\overline{\mathbf{c}'^2}. \tag{2.13}$$

If we imagine that a solid surface is present inside the gas, Eq. (2.13) represents the normal force per unit area that the gas exerts on the surface. From the pressure tensor, following the derivation from [33], the *viscous stress tensor* can be defined as the negative of the pressure tensor with the scalar pressure subtracted from the normal components:

$$\boldsymbol{\tau} \equiv \tau_{\alpha\beta} = -\left(nm\overline{c'_\alpha c'_\beta} - \delta_{\alpha\beta}P\right), \tag{2.14}$$

where $\delta_{\alpha\beta}$ is the Kronecker delta, which represents the identity matrix, $\mathbb{1}$, in Einstein notation. The identity matrix can, in fact, be defined as $\mathbb{1}_{\alpha,\beta} = \delta_{\alpha,\beta}$.

Finally, by computing Eq. (2.9) setting Q to one of the collisional invariants and by using the definitions from Eqs. (2.10)-(2.14), we obtain the conservation equations for the macroscopic quantities of a fluid, more commonly known as the Navier-Stokes equations:

$$\text{Mass:} \quad \frac{\partial \rho}{\partial t} + \boldsymbol{\nabla} \cdot (\rho \mathbf{u}) = 0, \tag{2.15}$$

$$\text{Momentum:} \quad \frac{\partial (\rho \mathbf{u})}{\partial t} + \mathbf{u} \cdot \boldsymbol{\nabla} (\rho \mathbf{u}) = -\boldsymbol{\nabla} \boldsymbol{P} + \boldsymbol{\nabla} \cdot \boldsymbol{\tau} + \rho \mathbf{F}, \tag{2.16}$$

where we limited our derivation to the first order moment (momentum equation), as the energy equation is not relevant for this work (we refer the reader to [33] for its derivation).

For Newtonian fluids in the continuum regime, the stress tensor $\boldsymbol{\tau}$ can be written as a function of the lower order moments:

$$\tau_{\alpha\beta} = \mu \left(\frac{\partial u_\alpha}{\partial r_\beta} + \frac{\partial u_\beta}{\partial r_\alpha} \right) + \delta_{\alpha\beta} \chi \frac{\partial u_\gamma}{\partial r_\gamma}, \tag{2.17}$$

where μ and χ are dynamic and volume viscosity (also known as bulk or second viscosity), respectively. For incompressible Newtonian fluids, we have that μ is a constant, $\chi = 0$ and, ultimately, $\boldsymbol{\nabla} \cdot \mathbf{u} = 0$. In this regime, Eq. (2.16) assumes the more popular form:

$$\frac{\partial (\rho \mathbf{u})}{\partial t} + \mathbf{u} \cdot \boldsymbol{\nabla} (\rho \mathbf{u}) = -\boldsymbol{\nabla} P + \mu \boldsymbol{\nabla}^2 \mathbf{u} + \rho \mathbf{F}, \tag{2.18}$$

which represents, together with $\boldsymbol{\nabla} \cdot \mathbf{u} = 0$, the incompressible Navier-Stokes equation of motion for the fluid parcel.

A fundamental application of Eq. (2.9) in a case where $\Delta[Q] \neq 0$ is given by setting $Q = H$, where H is the Boltzmann's H-function given by [41]:

$$H = \overline{\ln(nf)}. \tag{2.19}$$

The physical meaning of H can be understood by observing that over a small interval Δt, f changes to $f + \Delta f$ and the fractional change can be expressed as $\Delta f / f = \Delta(\ln f)$, so that H is the mean value of this infinitesimal variation and it is related to the thermodynamic entropy of the system.

By considering a dilute gas in its equilibrium state and without any external forcing, the only term different from zero in the left-hand side of Eq. (2.9) is the partial derivative with respect to time, while it can be shown that the collision integral on the right-hand side is always negative [33]. This result recovers the Boltzmann's H-theorem, i.e.

$$\frac{\partial H}{\partial t} < 0, \tag{2.20}$$

which states that the entropy of the system can only increase and recovers the second principle of thermodynamics from a statistical mechanical point of view. Due to the finite energy of the system, it can be shown that H will decrease monotonically to a finite lower bond, after which

$$\frac{\partial H}{\partial t} = 0. \tag{2.21}$$

From this relation, combined with Eq. (2.9), we can obtain the equilibrium, or Maxwellian distribution function f_0, which reads [41]

$$f^{eq} = \frac{\beta^3}{\pi^{3/2}} e^{-\beta^2 \mathbf{c}'^2}, \tag{2.22}$$

where $\beta = m/(2k_B T)$.

The NSE given by Eqs. (2.15) and (2.16), which describe the temporal and spatial evolution of the macroscopic fields, can be expressed as a closed set only when shear stresses can be defined in terms of the lower-order quantities, such as the velocity or the density fields, as shown in Eq. (2.17) for the viscous stress. When the gradients of the macroscopic variables become comparable to the typical distance traveled from molecules between collisions, which is called the mean free path λ, the aforementioned condition is not met and the continuum description is not valid anymore (continuum breakdown). In such cases, the gas flow is called rarefied, and the Knudsen number, namely the ratio between λ and a typical size of the system L, is the parameter that defines the rarefaction degree:

$$Kn = \frac{\lambda}{L}. \tag{2.23}$$

The mean free path, λ, is defined as [42]:

$$\lambda = \frac{2\mu}{\bar{c}_m \rho}, \tag{2.24}$$

where $\bar{c}_m = \sqrt{8k_B T/\pi m}$ is the mean thermal velocity for a gas molecule with temperature T and mass m.

Care must be taken in choosing the most significant value of L: while for simple geometries and uniform flows a general Kn number can be defined using a relevant size of the system, such as the channel width, a more precise approach can be established by using a local definition of Kn based on the characteristic scale length of the macroscopic gradients, so that for example $L = \rho/|\boldsymbol{\nabla}\rho|$ (or, similarly, using other macroscopic fields).

The NSE are generally considered accurate for $Kn < 0.1$, while the upper validity limit can be taken to be $Kn \simeq 0.2$. In the range of $0 < Kn \leq 0.2$ (slip flow regime), rarefaction effects are generally modeled through the introduction of second-order slip boundary conditions to capture the slip velocity, U_{slip}, that appears at the solid-fluid interface due to non equilibrium effects. These boundary conditions read:

$$U_{slip} = A_1 \lambda \left(\frac{\partial \mathbf{u}}{\partial \mathbf{n}} \right)_{wall} - A_2 \lambda^2 \left(\frac{\partial^2 \mathbf{u}}{\partial^2 \mathbf{n}} \right)_{wall}, \tag{2.25}$$

where $\mathbf{n}$ is the unit vector normal to the solid surface and pointing into the flow and A_1 and A_2 are parameters related to the gas-wall interaction. As an example of the breakdown of the continuum model, in Fig. 2.1 we show a comparison between the NS prediction of simple rectangular Poiseuille flow and the results from Direct Simulation Monte Carlo (DSMC) computations, which are able to correctly capture rarefaction effects without extra modeling since it is a BE solver (details of the numerical method will be extensively discussed in Chapter 3). The NS solution at a given vertical location y inside the channel for this kind of flow is given by

$$\frac{U(y)}{U_0} = \frac{4}{H^2} y(H - y) + U_{slip}^{norm}, \tag{2.26}$$

where $U_0 = \frac{\rho a}{8\mu} H^2$ is the centerline velocity at $Kn = 0$ obtained using a body force a on the fluid (e.g. gravity), H is the total height of the channel and $U_{slip}^{norm} = U_{slip}/U_0$ is the normalized slip velocity. For a Poiseuille flow the, U_{slip}^{norm} can be written as

$$U_{slip}^{norm} = 4A_1 Kn + 8A_2 Kn^2, \tag{2.27}$$

so that the final NS prediction is obtained by inserting the value of U_{slip} given by Eq. (2.27) into Eq. (2.26). The value of the coefficients is set to $A_1 = 0.8183$ and $A_2 = 0.65311$ following [43].

As can be seen from Fig. 2.1, the NS prediction with the addition of the slip model is accurate only for very small values of Kn, as important deviations appear for $Kn \gtrsim 0.2$. For $Kn > 0.2$, the continuum model must be replaced with a molecular based one, as the slip model embodied by Eq. (2.25) is no longer able to describe rarefaction effects.

Besides the Kn number, other two fundamental dimensionless quantities that define the physics of fluid flows are the Mach number and the Reynolds number:

$$Ma = \frac{u}{c_s}, \tag{2.28}$$

$$Re = \frac{uL}{\nu}, \tag{2.29}$$

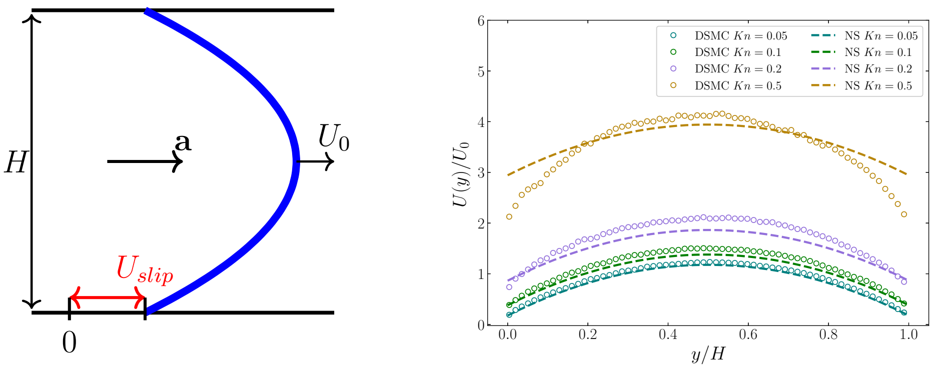

Figure 2.1: On the left, a sketch of the geometry of a rectangular force-driven Poiseuille flow. The distance between the channel walls is H, and a flow is driven by the presence of an external body force $\mathbf{a}$, which generates the typical parabolic velocity profile with centerline velocity U_0 as described in Eq. (2.26). In presence of a finite Kn number, non-equilibrium effects appear close to the walls and induce the appearance of a slip velocity U_{slip} at the fluid-solid interface. On the right, the comparison between the NS predictions (dashed lines) for a Poiseuille flow from Eq. (2.26) at finite Kn with the results from DSMC simulations (empty circles). The NS predictions are obtained using the second-order slip model from Eq. (2.27) using the values of the coefficients $A_1 = 0.8183$ and $A_2 = 0.65311$ [43]. The NS solution is reliable only for small values of Kn, as for $Kn \gtrsim 0.2$ the slip model is no more adequate to describe rarefaction effects in the flow.

where u and L are the characteristic velocity and length of the flow, respectively, c_s is the sound speed and $\nu = \mu/\rho$ is the kinematic viscosity. The Mach number measures the ratios of velocities in the flow, whereas the Reynolds number is a measure of inertial versus dissipative effects. In this work we will focus on quasi-incompressible Stokes flows, so that $Ma \ll 1$ and $Re \ll 1$.

2.3 Surface interactions in the continuum and low Reynolds number regime

In this Section, we will cover some fundamental examples of solid surface-flow interactions in the framework of vanishing Kn (continuum regime) and Re. A flow with vanishing Re is called a Stokes flow (or creeping flow) and in this regime the inertial and acceleration terms in Eq. (2.16) vanish, leading to the Stokes equations:

$$\nabla \cdot \mathbf{u} = 0, \tag{2.30}$$

$$\boldsymbol{\nabla} \cdot \boldsymbol{\sigma}^a = -\boldsymbol{\nabla} P + \mu \boldsymbol{\nabla}^2 \mathbf{u} = -\mathbf{F}, \tag{2.31}$$

where $\boldsymbol{\sigma}^a$ is called *absolute stress tensor* and it is related to the pressure and viscous stress tensor from Eqs. (2.12) and (2.14) by

$$\sigma^a_{\alpha\beta} = -P\delta_{\alpha\beta} + \tau_{\alpha\beta} = -P_{\alpha\beta}. \tag{2.32}$$

The most relevant difference between the Stokes Eqs. (2.30)-(2.31) and the NSE (2.15)- (2.16) is the disappearance of the non-linear advection term, so that the former set is linear. Linearity also implies that motions are reversible in the driving force (e.g gravity) and instantaneous, meaning that the flow will adapt very quickly (instantaneously) to modifications in the boundary conditions (such as a moving particle). The only requirements to determine the flow are, thus, given by the boundary conditions (on the particle and on the external boundaries of the flow), and the external forcing. To begin, we will present the solutions of simple relevant cases, such as the problems involving a single particle immersed in Stokes flow. For a more detailed explanation of the topic we refer to [44, 45].

The drag force on a particle in Stokes flow

The influence of the particle on the fluid flow arises from the surface interactions between the fluid in contact with the solid surface, which from a mathematical point of view are described by the boundary conditions that the solid particle imposes to the fluid motion. When Kn vanishes, these conditions are embodied by the so-called *no-slip boundaries*, meaning that the velocity of a fluid parcel in contact with an area of the solid surface is locally the same as the velocity of the surface element itself. For a particle with center of mass $\mathbf{r}_P$, this condition can be expressed, mathematically, as

$$\mathbf{u}(\mathbf{r}) = \mathbf{U}^P + \boldsymbol{\omega}^P \times (\mathbf{r} - \mathbf{r}_P), \tag{2.33}$$

where $\mathbf{r}$ is a point on the surface of the particle, $\mathbf{U}^P$ is the translational velocity and $\boldsymbol{\omega}^P$ is the rotational velocity of the particle.

The force acting on the particle due to the interactions with the fluid is called the *drag force* and is defined as the integral over the surface of the particle of the dynamic stress $\boldsymbol{\sigma} = \boldsymbol{\sigma}^a - \mathbf{F} \cdot \mathbf{r}\mathbb{1}$, i.e.

$$\mathbf{F}_D = \int_{S_P} (\boldsymbol{\sigma}^a - \mathbf{F} \cdot \mathbf{r}\mathbb{1}) \cdot \mathbf{n} dS = \int_{S_P} \boldsymbol{\sigma} \cdot \mathbf{n} dS, \tag{2.34}$$

where $\mathbf{n}$ is the outward unit vector normal from the surface of the particle and $\mathbf{F}$ represents an external body force (e.g. gravity). The reason of subtracting the hydrostatic stress field, given by the term $\mathbf{F} \cdot \mathbf{r}\mathbb{1}$, is to consider only the stress due to the relative motion between the fluid and the solid particle.

Motion of a single sphere in a general flow

In the most general case, and up to linear order, the form of the velocity and pressure fields at position $\mathbf{r}$ in a reference system centered on a particle moving in an unbounded fluid is given by:

$$\mathbf{u}(\mathbf{r}) = \mathbf{u}^{\infty} + \boldsymbol{\Omega}^{\infty} \times \mathbf{r} + \mathbf{E}^{\infty} \cdot \mathbf{r} + \mathbf{u}', \tag{2.35}$$

$$p = p^{\infty} + p', \tag{2.36}$$

where $\mathbf{u}^{\infty}$ and p^{∞} are the fluid velocity and pressure at infinity (i.e. far from the particle), $\boldsymbol{\Omega}^{\infty}$ and $\mathbf{E}^{\infty}$ are the ambient vorticity and strain and the primed quantities represent the perturbation induced by the presence of the moving particle, which can be decomposed into:

$$\mathbf{u}' = \mathbf{u}'_t + \mathbf{u}'_r + \mathbf{u}'_s, \tag{2.37}$$

$$p' = p'_t + p'_s, \tag{2.38}$$

where the subscripts t, r and s are abbreviations for *translation, rotation* and *strain*, respectively. It has to be noted that the rotational term in Eq. (2.38) is zero, as rotational motion does not influence the pressure field.

In the case of a spherical particle moving at velocity $\mathbf{U}_P$ and rotating at angular velocity $\boldsymbol{\omega}_P$, the analytical expressions for the perturbations in Eqs. (2.37)-(2.38) can be obtained by enforcing the no-slip conditions given by Eq. (2.33) [44], and read as:

$$u'_{t,\alpha} = \frac{3R}{4} U_{P,\beta} \left(\frac{\delta_{\alpha\beta}}{r} + \frac{x_\alpha x_\beta}{r^3} \right) + \frac{3R^3}{4} U_{P,\beta} \left(\frac{\delta_{\alpha\beta}}{3r^3} + \frac{x_\alpha x_\beta}{r^5} \right), \tag{2.39}$$

$$u'_{r,\alpha} = \left(\frac{R}{r} \right)^3 \varepsilon_{\alpha\beta\gamma} (\omega_{P,\beta} - \Omega^{\infty}_{\beta}) x_\gamma, \tag{2.40}$$

$$u'_{s,\alpha} = -\frac{5R^3}{2} \frac{x_\alpha (x_\beta E^{\infty}_{\beta\gamma} x_\gamma)}{r^5} - \frac{R^5}{2} E^{\infty}_{\beta\gamma} \left[\frac{\delta_{\alpha\beta} x_\gamma + \delta_{\alpha\gamma} x_\beta}{r^5} - \frac{5 x_\alpha x_\beta x_\gamma}{r^7} \right], \tag{2.41}$$

where u'_α is the component α of the fluid velocity at position $\mathbf{r}$ in the reference system centered on the particle, R is the particle radius and r is the distance between $\mathbf{r}$ and the particle center and $\varepsilon_{\alpha\beta\gamma}$ is the Levi-Civita tensor. A graphical representation of

Eqs (2.39)-(2.41) is presented in Fig. 2.2.
Analogously, for the pressure the analytical solutions read [44]:

$$p_t' = \frac{3\mu R}{2}\frac{U_{P,\alpha}x_\alpha}{r^3}, \tag{2.42}$$

$$p_s' = -5\mu R^3 \frac{x_\alpha E^\infty_{\alpha\beta} x_\beta}{r^5}, \tag{2.43}$$

where μ is the dynamic viscosity of the fluid.

The hydrodynamic force, torque and stresslet (i.e. the symmetric first moment of the surface stress) acting on the particle are obtained by the integration of the stress tensor, $\boldsymbol{\sigma}$, over the normal vector to the surface elements:

$$\mathbf{F}^h = \int_{S_p} \boldsymbol{\sigma} \cdot \boldsymbol{n} dS = 6\pi\mu R \boldsymbol{U}^\infty, \tag{2.44}$$

$$\mathbf{T}^h = \int_{S_p} \mathbf{r} \times \boldsymbol{\sigma} \cdot \boldsymbol{n} dS = 8\pi\mu R^3 \boldsymbol{\omega}^\infty, \tag{2.45}$$

$$S_{\alpha\beta} = \frac{1}{2}\int_{S_p} \left[\sigma_{\alpha\gamma}x_\beta + \sigma_{\beta\gamma}x_\alpha\right] n_k dS = \frac{20\pi}{3}\mu R^3 E^\infty_{\alpha\beta}. \tag{2.46}$$

An important application of these relations is the case of a spherical particle settling in an unbounded and quiescent fluid by the action of an external force, such as gravity. In this case, and under steady conditions, the drag force will balance the excess weight of the particle and Eq. (2.34) can be written as

$$F_D = \int_{S_p} (\boldsymbol{\sigma}^a + \rho \mathbf{g} \cdot \mathbf{r}\delta_{\alpha\beta}) \cdot \mathbf{n} dS = -\frac{4}{3}\pi R^3 (\rho_P - \rho)\mathbf{g}. \tag{2.47}$$

By combining Eq. (2.44) with the result from Eq. (2.47), and by substituting $\mathbf{U}^\infty$ with $-\mathbf{U}_P$ (which is always possible in Stokes flows thanks to their linearity), we can obtain a relation for the final equilibrium velocity of the settling particle, commonly referred at as the *settling velocity*:

$$\mathbf{U}_s = \frac{2}{9}\frac{(\rho_P - \rho)R^2}{\mu}\mathbf{g}. \tag{2.48}$$

Motion of ellipsoidal particles

When particles with more complex shape are considered, it is in general not straightforward (and in most cases not possible at all) to derive an exact expression for the

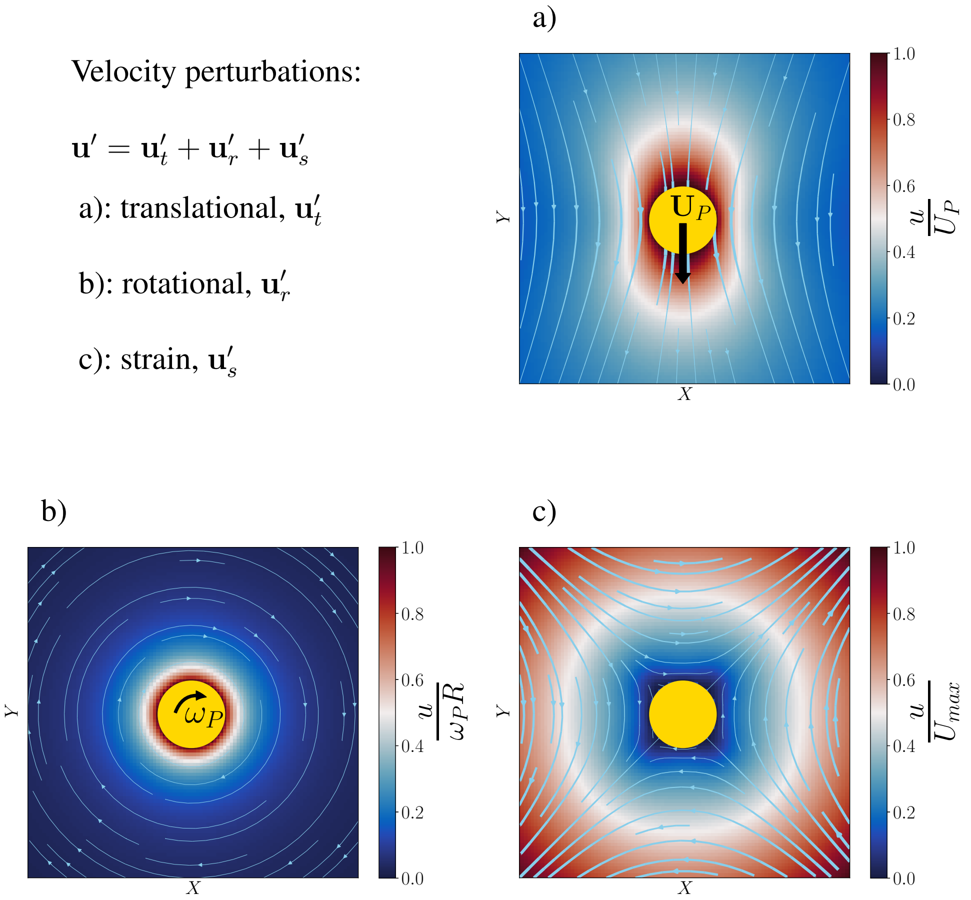

Figure 2.2: Examples of different velocity perturbations in the xy plane induced by the presence of a spherical particle with radius R in an unbounded fluid. On the top right (a), the perturbations given by Eq. (2.39) induced by a sphere translating at velocity U_P along the negative y direction in a quiescent fluid are plotted. The flow field is normalized with respect to U_P. In the bottom left (b), we show the perturbations given by Eq. (2.40) produced by a rotating sphere with angular velocity ω_P in a quiescent fluid, normalized with respect to the velocity at the boundaries of the sphere given by $\omega_P R$. At the bottom right (c), we present the flow fields in presence of an ambient strain with only non-zero components given by $E_{xy} = E_{yx} = 1$, obtained by inserting Eq. (2.41) into the general expression for the flow given by Eq. (2.35).

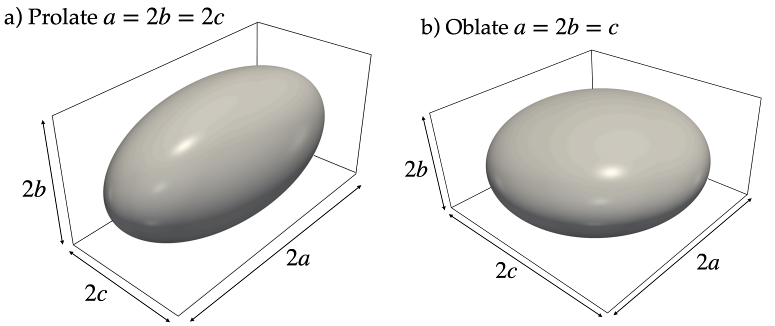

Figure 2.3: Sketch of a prolate (a) and oblate (b) ellipsoids with major axis a, minor axes b and focal radius $c = \sqrt{a^2 - b^2}$.

perturbation induced by the particle on the flow field. Luckily, the drag and torque integrals for ellipsoidal particles can be solved analytically in the case of prolate or oblate particles immersed in uniform flows. Ellipsoidal particles are of extreme interest in many practical applications, as not only they include a large variety of shapes, such as needles and flakes, but also because most of the physical cross-section geometries can be described as ellipsoidal shapes, so that ellipsoidal particles with different aspect ratios can be used as good approximation for a large variety of complex shapes.

The first derivation of the drag force experienced by a prolate or oblate ellipsoidal particle translating in a fluid was derived by Oberbeck [46]. Some years later, Happel and Brenner [45] obtained the same result by solving the axisymmetrical creeping flow past a spheroidal particle in ellipsoidal coordinates. An example of a prolate and oblate ellipsoid with major axis a, minor axes b and focal radius $c = \sqrt{a^2 - b^2}$, is presented in Fig. 2.3. The drag force acting on this class of particles, for the case in which their symmetry axis is aligned along an external flow with velocity U^{∞}, reads:

$$F_D^{pr} = -\frac{8\pi\mu c U^{\infty}}{(A_{pr}^2 - 1)\coth^{-1} A_{pr} - A_{pr}}, \tag{2.49}$$

$$F_D^{ob} = -\frac{8\pi\mu c U^{\infty}}{A_{ob} - (A_{ob}^2 - 1)\cot^{-1} A_{ob}}, \tag{2.50}$$

where $A_{pr} = a/c$ and $A_{ob} = b/c$ are shape-dependent quantities for the prolate and oblate case, respectively.

Concerning the rotational dynamics, the first analytical solution of an ellipsoid rotating in a shear flow has been derived by Jeffery [47], who solved the rotational problem in ellipsoidal coordinates. The angular velocity $\omega(t)$ of a general spheroidal particle set into motion by an unbounded shear flow is given by

$$\omega(t) = \frac{C}{a^2 + b^2} \left(a^2 \cos^2 \theta(t) + b^2 \sin^2 \theta(t) \right), \tag{2.51}$$

$$\tan \theta(t) = \frac{a}{b} \tan \left[\frac{Cabt}{a^2 + b^2} \right], \tag{2.52}$$

where a and b are the major and minor axes of the ellipsoid in the plane of the shear, respectively. Here, $C = 2U_{shear}/L$ is the shear rate, assuming that the shear flow is driven by two moving parallel walls separate by a distance L with respective velocities $\pm U_{shear}$. The variable $\theta(t)$ describes the angle between the major axis and one of the main directions in the shear plane. The angular velocity $\omega(t)$ of the ellipsoid is then described by a family of curves that depend on the shear rate and on the starting orientation of the particle, and in general it will show periodic oscillations with period

$$T_{jef} = \frac{\pi(a^2 + b^2)}{abC}. \tag{2.53}$$

Two particular cases are shown in Fig. 2.4, where the analytical trajectory of the angular velocity is plotted for a sphere and for an ellipsoid with internal aspect ration $a/b = 2$ and $a/b = 4$.

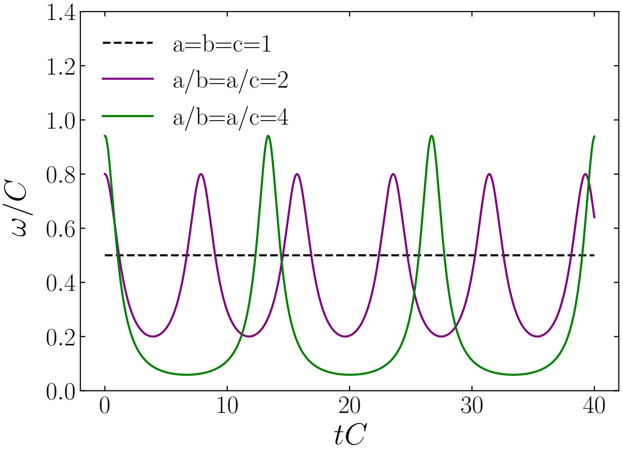

Figure 2.4: Analytical prediction given by Eq. (4.8) of the angular frequency as a function of time for a sphere with $a/b = a/c = 1$ (black dashed line) and for a prolate ellipsoid with aspect ratio $a/b = a/c = 2$ (purple) and one with $a/b = a/c = 4$ (green) originally oriented with the major axis a parallel to the flow. The angular frequency and time are normalized with respect to the shear rate $C = 2U_{shear}/L$.

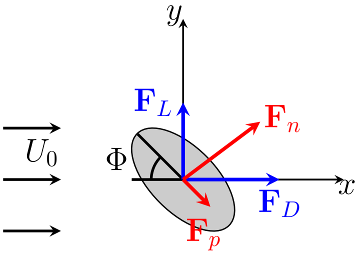

Figure 2.5: Decomposition of forces acting on an arbitrary-shaped particles (depicted as ellipsoidal for simplicity) oriented with angle Φ with respect to the ambient flow $\mathbf{U}_0$. The drag and lift forces ($\mathbf{F}_D$ and $\mathbf{F}_L$, repetitively) are always oriented parallel (drag) and perpendicular (lift) to the ambient flow, while normal ($\mathbf{F}_n$) and parallel ($\mathbf{F}_p$) forces are aligned with, or orthogonal to, the principal axis of the particle, respectively.

The sine-squared drag law

One fundamental application of the linearity of Stokes flows is related to the derivation of a general scaling law, with respect to the relative orientation between an arbitrary shaped particle and a uniform ambient flow, for the drag and lift forces acting on the particle. According to Happel and Brenner [45], who first derived such relations, the general expression for the drag force on a particle with an arbitrary shape immersed in uniform ambient flow can be expressed as

$$\mathbf{F}_D = 6\pi\mu R_{eq}\mathbf{U}_0 K, \tag{2.54}$$

where $R_{eq} = \sqrt[3]{3V/3\pi}$ is the radius of the sphere with equivalent volume, V, of the investigated particle and K is a shape-dependent correction factor to be determined. Happel and Brenner [45] then show that Eq. (2.54) can be applied to describe orientation effects as a function of only the drag force at 0°, the drag force at 90° and a trigonometric function of the relative orientation between the particle and the ambient flow.

To derive this relation, we consider the general problem of the drag exerted by a flow with ambient velocity $\mathbf{U}_0$ on a generic particle oriented with angle Φ with respect to the flow, sketched in Fig. 2.5. It is always possible to define a reference frame xyz in which the x axis is in the same direction of $\mathbf{U}_0$. In this way the drag force $\mathbf{F}_D$ lies on x and it forms an angle Φ with respect to the principal axis of the particle, while the lift force $\mathbf{F}_L$ lies on y. Additionally, the resistance forces along the parallel and normal directions with respect of the major axis of the particle can be defined as $\mathbf{F}_p$ and $\mathbf{F}_n$, respectively.

The drag and lift forces can then be expressed as a combination of F_p and F_n:

$$\mathbf{F}_D = \mathbf{F}_p \cos\Phi + \mathbf{F}_n \sin\Phi \tag{2.55}$$

$$\mathbf{F}_L = \mathbf{F}_n \cos\Phi - \mathbf{F}_p \sin\Phi, \tag{2.56}$$

So that the total force acting on the particle can be obtained as $\mathbf{F}_{tot} = \mathbf{F}_D + \mathbf{F}_L$, or, similarly, as $\mathbf{F}_{tot} = (F_D, F_L)$. In the latter notation the vector notation is dropped as F_D and F_L now refer to the total force components along x and y, respectively. For the rest of this work, we will adopt this notation, referring to the drag and lift forces as components. Using Eq. (2.54) we can directly obtain the expressions for F_p and F_n in the xyz reference frame:

$$\mathbf{F}_p = 6\pi\mu R_{eq}\mathbf{U}_0 \cos\Phi K_{0^\circ}, \tag{2.57}$$

$$\mathbf{F}_n = 6\pi\mu R_{eq}\mathbf{U}_0 \sin\Phi K_{90^\circ}, \tag{2.58}$$

where we specified different correction terms K for the case at 0° and 90°. By inserting Eqs. (2.57)-(2.58) into the Eqs. (2.55)-(2.56) we obtain the general relation for F_D and F_L with respect to the orientation Φ as originally derived by Happel and Brenner [45]

$$F_D = F_{D,0^\circ} + (F_{D,90^\circ} - F_{D,0^\circ}) \sin^2\Phi, \tag{2.59}$$

$$F_L = (F_{D,90^\circ} - F_{D,0^\circ}) \sin\Phi \cos\Phi, \tag{2.60}$$

where we indicated with $F_{D,0^\circ}$ and $F_{D,90^\circ}$ the drag force experienced by the particle at $\Phi = 0^\circ$ and $\Phi = 90^\circ$, respectively. These relations are extremely important as not only they show the explicit Φ-dependence of the drag and lift forces, but also that it is sufficient to know $\mathbf{F}_{D,0^\circ}$ and $\mathbf{F}_{D,90^\circ}$ to obtain a complete knowledge of the orientation effects on the drag and lift on any kind of particle.

The relation expressed by Eq. (2.59) is commonly referred to as *sine-squared drag law*, and it is not only valid in the continuum, low Reynolds number regime. Recent studies [48,49], in fact, show that this relation holds for non-spherical particles such as fibers and ellipsoids also at larger values of Re, and we will show later that it appears unchanged also in collisionless flows for which the streaming velocity is sufficiently small.

2.4 Surface interactions in the free-molecular regime

In the previous Section we showed how to apply the NSE in the continuum regime to address some basics particle-flow interaction problems. In this Section we will show, instead, how to directly apply the BE to obtain solutions of surface-gas interactions problems in such cases where an analytical solution is obtainable. One fundamental example of such cases is given by free-molecular (or collisionless) flows, i.e. flows for which the Knudsen number tends to infinity:

$$Kn = \frac{\lambda}{L} \to \infty. \tag{2.61}$$

Collisionless flows are thus associated with either very low densities (which lead to a large mean free path) or very small characteristic lengths. For this kind of flows, the collisional term in Eq. (2.7) vanishes and, in the absence of external force fields, the collisionless Boltzmann equation reads

$$\frac{\partial}{\partial t}(nf) + \mathbf{c} \cdot \frac{\partial}{\partial \mathbf{r}}(nf) = 0, \tag{2.62}$$

and it can be solved analytically for simple steady [33] and unsteady [50] flows.

In the rest of this Section we are interested in showing how to apply the gas-kinetic description, from an analytic point of view, to investigate the aerodynamics of different bodies immersed in a free-molecular flow. This class of problems is of great interest in many real-case applications related to particle contamination in high-tech systems, where the typical size of the particles is of few μm (or even nm), while the mean free path of the gas is typical on the order of mm. This leads to an extremely large particle-based Knudsen number, and the particle-flow interaction can be regarded as free-molecular.

The basic assumption required to derive the fundamental quantities related to the gas-surface interactions in the free-molecular limit is that the gas is in an equilibrium state, so that its distribution function is given by the Maxwell-Boltzmann distribution from Eq. (2.22). The collisionless assumption imposes that the gas molecules that are reflected from the surface of the solid object do not interact with the incoming flow and, thus, the surface quantities are obtained by using Eq. (2.22) in the calculation of the transfer equation, given by Eq. (2.9).

Derivation of fluxal quantities

In order to derive the description of the interactions between a collisionless gas in thermal equilibrium with a solid surface, we need to define some fundamental flux quantities across a surface element. Following the derivation from Bird [33], the geometry of the problem is as follows: the stream velocity $\mathbf{u}$ of the gas is inclined with an angle θ with respect to unit normal vector $\mathbf{n}$ to the surface element, as sketched in Fig. 2.6. The reference system is chosen in a way, and without loss of generality, that the x axis goes in the opposite direction of $\mathbf{n}$ and that the streaming velocity lies in the $xy-$plane. In this way, each molecule has velocity components

$$u = u' + \mathbf{u}\cos\theta, \tag{2.63}$$

$$v = v' + \mathbf{u}\sin\theta, \tag{2.64}$$

$$w = w', \tag{2.65}$$

where $u,\ v$ and w refer to the velocity components along the $x,\ y$ and z coordinates respectively (as discussed in Section 2.2).

The inward, i.e. along the negative direction of $\mathbf{n}$, flux of some quantity $\mathbf{Q}$ can then be obtained by directly computing Eq. (2.9), using the equilibrium distribution f^{eq} in place of f, i.e.

$$\begin{aligned}\overline{n\mathbf{Q}u} &= n \int_{-\infty}^{+\infty}\int_{-\infty}^{+\infty}\int_{0}^{+\infty} \mathbf{Q}uf^{eq}dudvdw = \\ &= \frac{n\beta^3}{\pi^{3/2}} \int_{-\infty}^{+\infty}\int_{-\infty}^{+\infty}\int_{0}^{+\infty} Que^{-\beta^2(u'^2+v'^2+w'^2)}dudvdw.\end{aligned} \tag{2.66}$$

The three main quantities related to gas-surface interactions are the *inward number flux*, N_i, the *inward normal momentum flux*, p_i, and the *inward parallel momentum flux*, τ_i and they can be obtained by setting $\mathbf{Q}$ in Eq. (2.66) to 1, mu and mv, respectively. In the computation we used Eqs. (2.63)-(2.65) to expand the molecular velocities (and relative integration limits) and to transform the differential operators. The expressions for the aforementioned fluxes, as obtained by Bird [33], are given below:

$$\begin{aligned}N_i &= \frac{n\beta^3}{\pi^{3/2}} \int_{-\infty}^{+\infty} e^{-\beta^2 w'^2}dw' \int_{-\infty}^{+\infty} e^{-\beta^2 v'^2}dv' \int_{-\mathbf{u}\cos\theta}^{+\infty} (u' + \mathbf{u}\cos\theta)e^{-\beta^2 u'^2}du' = \\ &= \frac{n}{2\pi^{1/2}\beta}\left[e^{-s^2\cos^2\theta} + \pi^{1/2}s\cos\theta\{1 + \mathrm{erf}(s\cos\theta)\}\right],\end{aligned} \tag{2.67}$$

$$\begin{aligned}p_i &= \frac{nm\beta^3}{\pi^{3/2}} \int_{-\infty}^{+\infty} e^{-\beta^2 w'^2}dw' \int_{-\infty}^{+\infty} e^{-\beta^2 v'^2}dv' \int_{-\mathbf{u}\cos\theta}^{+\infty} (u' + \mathbf{u}\cos\theta)^2 e^{-\beta^2 u'^2}du' = \\ &= \frac{\rho}{2\pi^{1/2}\beta^2}\left[s\cos\theta e^{-s^2\cos^2\theta} + \pi^{1/2}\{1 + \mathrm{erf}(s\cos\theta)\}\left(\frac{1}{2} + s^2\cos^2\theta\right)\right],\end{aligned} \tag{2.68}$$

$$\tau_i = \frac{nm\beta^3}{\pi^{3/2}} \int_{-\infty}^{+\infty} e^{-\beta^2 w'^2} dw' \int_{-\infty}^{+\infty} (v' + \mathbf{u} \sin\theta) e^{-\beta^2 v'^2} dv' \times$$
$$\times \int_{-\mathbf{u}\cos\theta}^{+\infty} (u' + \mathbf{u}\cos\theta) e^{-\beta^2 u'^2} du' =$$
$$= \frac{\rho}{2\pi^{1/2}\beta^2} s \sin\theta \left[\theta e^{-s^2\cos^2\theta} + \pi^{1/2} s \cos\theta \{1 + \mathrm{erf}(s\cos\theta)\} \left(\frac{1}{2} + s^2 \cos^2\theta \right) \right], \tag{2.69}$$

where

$$s = |\mathbf{u}|\beta = \frac{|\mathbf{u}|}{c'_m} \tag{2.70}$$

is the molecular speed ratio, i.e. the ratio between the streaming velocity and the most probable molecular speed, and

$$\mathrm{erf}(x) = \frac{2}{\pi^{1/2}} \int_0^x e^{-t^2} dt \tag{2.71}$$

is the error function.
As it will be shown later, Eqs. (2.67)-(2.69) provide the fundamental quantities required to compute the drag and lift force exerted by an equilibrium gas flow on a solid body.

Surface interactions in collisionless flows

The surface pressure and shear stress expressed in Eqs. (2.68)-(2.69) can be directly integrated over the surface of the solid body to obtain the aerodynamics forces acting on it. In order to perform such calculation, we first need to obtain the same fluxal quantities related to the reflected molecules, which will be indicated with the subscript r, as the total momentum exchanged by the gas on the surface will be the sum of the contributions from incoming and reflected particles. In the absence of absorption or emission effects at the surface, the incident number flux must be equal to the reflected one, therefore we have that the total fluxes read:

$$N = N_i + N_r = 0, \tag{2.72}$$

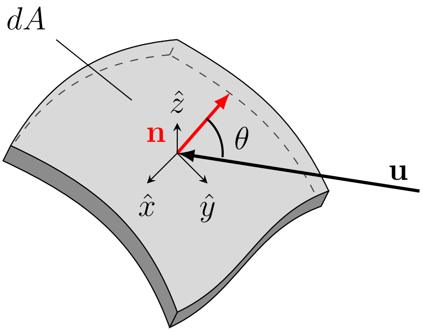

Figure 2.6: Coordinate system used for the derivation of fluxal quantities from Eqs. (2.67)-(2.69) across a surface element dA.

$$p = p_i + p_r = 0, \tag{2.73}$$

$$\tau = \tau_i + \tau_r = 0. \tag{2.74}$$

To evaluate the reflected quantities, we need to define the type of reflection that the gas molecules undergo when they hit the solid surface. Maxwell [51] proposed two models to describe this interaction: specular reflection, in which collisions are perfectly elastic and the normal component of the velocity with respect to the solid surface is reversed, and diffusive reflections, in which the velocity of each molecule is reset to a Maxwell-Boltzmann distribution after the collision event. The most general way to describe gas-surface interactions is typically to consider a combination of the aforementioned models, as a comprehensive general theory of such interactions is absent. More complex models of gas-surface interactions have been introduced in the attempt to cover this gap, such as the Cercignani-Lampis-Lord model [52], but the mathematical complexity of these models is often difficult to connect with experimental data. The values of the reflected fluxal quantities for specular reflections are:

$$p_r = p_i \tag{2.75}$$

$$\tau_r = -\tau_i, \tag{2.76}$$

while for diffusive reflection, the only difference is given by

$$\tau_r = 0. \tag{2.77}$$

If a fraction σ of molecules undergoes diffusive reflection and the remaining $(1-\sigma)$ is reflected specularly, the above results can be combined to obtain the general expression for the pressure and shear stress acting on the surface element of the particle. In Eqs. (2.68)-(2.69) we express the orientation dependence through the angle θ, which is the angle between the streaming velocity and the normal component at the surface. It is more natural, however, to use the angle of attack $\Phi = \pi/2 - \theta$ for aerodynamics studies. The expressions of the pressure and shear stress then read [33]:

$$
\begin{aligned}
\frac{p}{p_0} = \frac{2\beta_0^2 p}{p_0} = & \left[(2-\sigma)\pi^{-1/2} s \sin\Phi + \frac{1}{2}\sigma\left(\frac{T_w}{T_0}\right)^{1/2}\right] \times \\
& \times e^{-s^2 \sin^2\Phi} + \left[(2-\sigma)\left(\frac{1}{2} + s^2\sin^2\Phi\right) + \right. \\
& \left. + \frac{1}{2}(2-\sigma)\left(\frac{T_w}{T_0}\right)^{-1/2} \pi^{1/2} s \sin\Phi\right][1 + \mathrm{erf}(s\sin\Phi)] \qquad (2.78)
\end{aligned}
$$

$$
\frac{\tau}{p_0} = \frac{2\beta_0^2 \tau}{p_0} = \pi^{-1/2}\sigma s \cos\Phi\left[e^{-s^2\sin^2\Phi} + \pi^{1/2} s \sin\Phi\{1 + \mathrm{erf}(s\sin\Phi)\}\right], \tag{2.79}
$$

where the subscript 0 refers to the ambient values (i.e. far from the solid surface) and T_w is the temperature of the solid surface, which is relevant only in the case of diffusive reflections. The drag and lift forces can then be obtained from the integration over the particle surface of Eqs. (2.78)-(2.79):

$$
F_D = \int_{S_p} (p\cos\theta + \tau\sin\theta) dS, \tag{2.80}
$$

$$
F_L = \int_{S_p} (p\sin\theta - \tau\cos\theta) dS, \tag{2.81}
$$

from which the drag and lift coefficients can be immediately obtained:

$$
C_D = \frac{F_D}{\frac{1}{2}\rho_0 U^2 A}, \tag{2.82}
$$

$$
C_L = \frac{F_L}{\frac{1}{2}\rho_0 U^2 A}, \tag{2.83}
$$

where U is a characteristic velocity of the flow (usually the streaming velocity) and A is a relevant area of the solid body (usually the cross-sectional area).

The evaluation of the integrals given by Eqs. (2.80)-(2.81) on complex surfaces is, however, a complicated task also using numerical techniques and can be carried on analytically only for the most simple surfaces. In the following of this paragraph we will present and comment some applications of this approach.

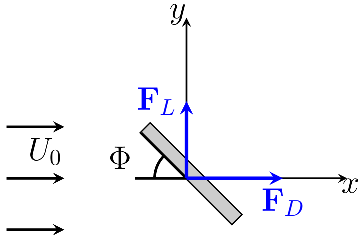

Figure 2.7: Sketch of aerodynamics of a thin plate oriented at angle of attack Φ with respect to uniform ambient flow with velocity U_0

Drag on a thin plate

The case of a rectangular plate is the first natural example as Eqs (2.78)-(2.79) can be directly applied (without integration) to determine its aerodynamic properties. A sketch of the problem is presented in Fig. 2.7.

The net force is obtained, in fact, by subtracting the pressure on the upper plate, for which the values of Φ are negative, to the pressure on the upper plate, for which Φ assumes positive values. The final results for the drag and lift coefficients are [33]:

$$\begin{aligned} C_D = {} & 2\frac{1-(1-\sigma)\cos(2\Phi)}{\pi^{1/2}s}e^{-s^2\sin^2\Phi} + \\ & + \frac{\sin\Phi}{s^2}\left[1+2s^2+(1-\sigma)\{1-2s^2\cos(2\Phi)\}\right]\mathrm{erf}(s\sin\Phi) + \\ & + \frac{\sigma}{s}\pi^{1/2}\sin^2\Phi\left(\frac{T_2}{T_0}\right)^{1/2} \end{aligned} \tag{2.84}$$

$$\begin{aligned} C_L = {} & \frac{3(1-\sigma)}{\pi^{1/2}s}\sin\Phi\cos\Phi e^{-s^2\sin^2\Phi} + \frac{\cos\Phi}{s^2}\{1+(1-\sigma)(1+4s^2\sin^2\Phi\}\times \\ & \times\,\mathrm{erf}(s\sin\Phi) + \frac{\sigma}{s}\pi^{1/2}\sin\Phi\cos\Phi\left(\frac{T_w}{T_0}\right)^{1/2}. \end{aligned} \tag{2.85}$$

The scaling of C_D and C_L, with respect to the angle of attach Φ, is presented in Fig. 2.8. It is interesting to observe that the correlations typical of the continuum regime from Eqs. (2.59)-(2.60) holds also for the collisionless regime, in the limit of low values of the speed ratio $s = U_0\left(\frac{m}{2k_BT}\right)^{1/2}$. This highlights that rarefaction effects do not depend on the orientation of the solid body with respect to the gas flow. This result is related to the fact that for low free stream velocities, the friction due to pressure effects and the one due to tangential effects are equally important in the interactions between the gas molecules and the surface of the solid object (see discussion in [33]).

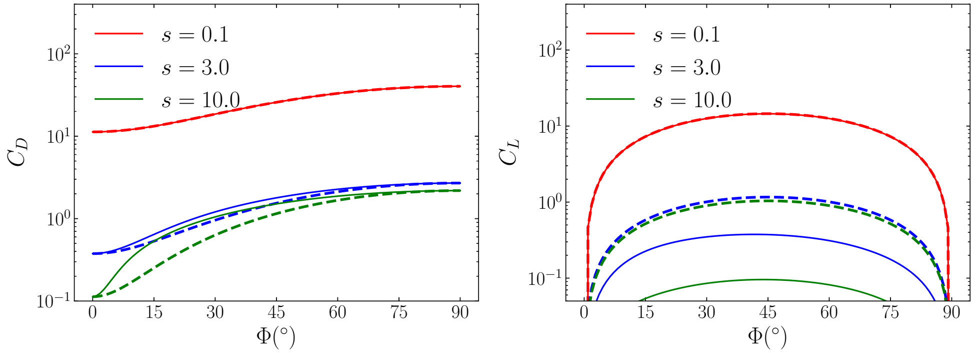

Figure 2.8: Drag (left) and lift (right) coefficients (solid lines) as obtained from Eqs (2.84)-(2.85) for a thin rectangular plate immersed in a collisionless gas flow for different speed ratios $s = U_0 \left(\frac{m}{2k_B T}\right)^{1/2}$ as a function of the angle of attack, Φ. The results, obtained for a fully diffusive surface, are compared with the analytical correlations (dashed lines) proposed by Happel and Brenner [45] and embodied in Eqs. (2.59)-(2.60). For small velocities the prediction from the continuum regime holds also in the collisionless case, highlighting that rarefaction effects do not depend on the relative orientation of the solid body with respect to the incoming flow in the limit of small speed ratios.

Drag on a sphere in the collisionless limit

For bodies different than flat plates, Eqs. (2.80)-(2.81) must be integrated over the solid surface. For a spherical particle, this is particularly straightforward as the integration can be performed in polar coordinates. In such reference system, the polar angle θ corresponds to angle θ in the flux Eqs. (2.67)-(2.69), so that the drag coefficient based on the cross-sectional area of the sphere is [33]

$$C_D = \frac{\int\limits_0^{\pi} (p\cos\theta + \tau\sin\theta) 2\pi r^2 \sin\theta d\theta}{\frac{1}{2} U^2 \pi R^2} =$$

$$= \frac{2s^2+1}{\pi^{1/2} s^3} e^{-s^2} + \frac{4s^4+4s^2-1}{2s^4} \operatorname{erf}(s) + \frac{2\sigma\pi^{1/2}}{3s} \left(\frac{T_w}{T_0}\right)^{1/2} . \qquad (2.86)$$

This result is an extension to the pioneering work of Epstein [53], who firstly obtained a relation for the drag force exerted by a gas on a spherical particle in the limit of low streaming velocities (i.e. for small values of s). From the scaling of Eq. (5.10) with respect to the molecular speed ratio s, presented in Fig. 2.9, we can observe that C_D decreases monotonically until the supersonic limit is reached, for which $s = 1$

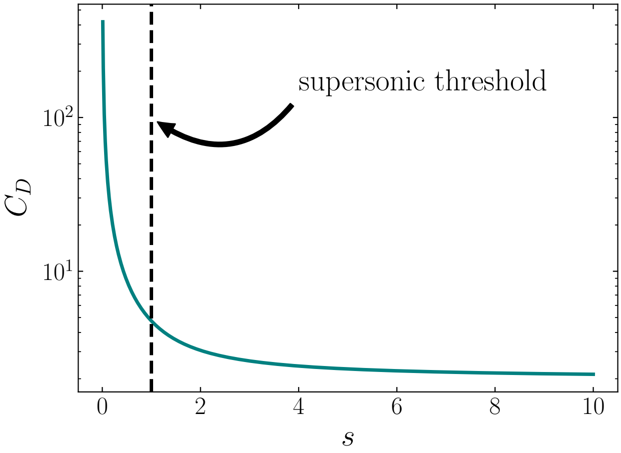

Figure 2.9: Drag coefficient C_D of a spherical particle, as obtained by Bird [33], in uniform collisionless flow for different values of the molecular speed ratio s, as described by Eq. (5.10). Results are obtained for a fully diffuse surface with $\sigma = 1$.

and $Ma \sim 1$. We then observe the onset of trend reversal, with a steady and fast monotonic increase of C_D as s reaches higher values.

Drag on an ellipsoid in the collisionless limit

When dealing with ellipsoidal particles, Eqs. (2.80)-(2.81) must be integrated using ellipsoidal coordinates, and a general expression similar to Eq. (5.10) is, up to our knowledge, not available in the literature. Dahnekë [54], however, presents a derivation valid in the limit of small streaming velocities (using a similar approach as Epstein did for spherical particles). The final expression of the drag force exerted by a flow with ambient velocity U_0 on a prolate ellipsoidal particle, as obtained by Dahnekë [54], reads:

$$\begin{aligned} F_{pr} = & \frac{\pi \mu a b U_0}{\lambda} \Bigg[\sin^2(\Phi) \times \left(A_{pr} \left\{ 4 + \left(\frac{\pi}{2} - 1 \right) \sigma \right\} + \frac{C_{pr}}{B_{pr}^2} \left\{ 2 + \frac{4B_{pr}^2 + \pi - 6}{4} \sigma \right\} \right) + \\ & + \cos^2(\Phi) \left(2 A_{pr} \sigma + \frac{C_{pr}}{B_{pr}^2} \left\{ B_{pr}^2 (4 - 2\sigma) - 4 + \left(3 - \frac{\pi b^2}{2a^2} \right) \sigma \right\} \right) \Bigg], \end{aligned} \tag{2.87}$$

where a and b are the ellipsoid major and minor axes, respectively, $B_{pr} = \sqrt{1 - b^2/a^2}$, $A_{pr} = \sin^{-1}(B_{pr})/B_{pr}$ and $C_{pr} = b/a - A_{pr}$. Similarly, the expression for the drag force on oblate ellipsoids reads:

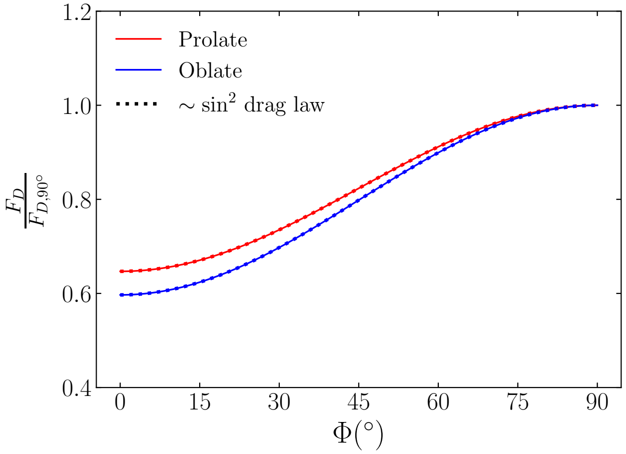

Figure 2.10: Drag force experienced by a prolate (red) and oblate (blue) ellipsoidal particle in the free molecular regime, as obtained from Eqs. (2.87) and (2.88), for a fully diffuse surface $\sigma = 1$, as function of the orientation Φ. Results, normalized with respect to the drag force at $\Phi = 90^\circ$, are obtained for a particle with volume $V = 6.5 \times 10^{-20}\mathrm{m}^3$ and aspect ratio $a/b = 2$ immersed in uniform argon gas flow with ambient velocity $U_0 = 100 m/s$ and temperature $T = 300K$. As it can be seen, the sine-squared drag law (dashed lines) given by Eq. (2.59) is still valid in the free molecular regime.

$$\begin{aligned}F_{ob} =& \frac{\pi \mu ab U_0}{\lambda}\Bigg[\sin^2(\Phi)\Bigg(A_{ob}^2 B_{ob}\Bigg\{\frac{6-\pi}{4}\sigma - 2\Bigg\} + C_{ob}\Bigg\{4 - \frac{4-\pi}{2}\sigma\Bigg\} + \frac{a}{b}\sigma\Bigg) + \\ &+ \cos^2(\Phi)\Bigg(A_{ob}^2 B_{ob}\Bigg\{4 - \frac{6-\pi}{2}\sigma\Bigg\}\frac{a^2}{b^2} + C_{ob}\sigma + \frac{a}{b}\sigma\Bigg)\Bigg],\end{aligned} \tag{2.88}$$

with $A_{ob} = 1/\sqrt{a^2/b^2 - 1}$, $C_{ob} = A_{ob}\log\left(a/b + 1/A_{ob}\right)$ and $B_{ob} = a/b - C_{ob}$. A relative comparison between Eqs. (2.87) and (2.88) is presented in Fig. 2.10, where it is shown that the sine-squared drag law from Eq. (2.59), valid in the continuum regime, is extendable to the free molecular case.

2.5 From the continuum to the free molecular limits: the transition regime

In the previous Section we presented how to model fluid-surface interactions in the free-molecular regime, i.e. neglecting inter-molecular collisions by setting the collision operator in the BE to zero. This approximation is valid only for very large values of the Knudsen number, Kn, and in many practical applications this condition is not met, as inter-molecular collisions still play an important role. An example of the impact of intermolecular collisions on the drag experienced by a sphere immersed in a uniform ambient gas flow is shown in Fig. 2.11, where the resulting drag force from DSMC collisional and collisionless simulations is compared for different values of Kn. In this kind of simulations, a fully resolved spherical particle is kept fixed in space at the center of the simulation box and a constant ambient flow is generated around it; the total drag exerted by the gas on the particle is then computed and compared for the different cases. In-depth details on the on how to setup this kind of DSMC simulations will be given in Chapter 5. From the results, it is evident that collisions are particularly relevant when $Kn \leq 10$, but their effect is still appreciable at $Kn = 10$, which typically is chosen as starting point of the free molecular regime.

When the mean free path λ of the gas is comparable with the size of the system, i.e. $0.2 < Kn < 10$, rarefaction effects are dominant, but the collision operator in the BE can not be regarded as vanishing. This regime is called the *transition regime*, and it represents the most challenging regime to be investigated numerically, theoretically and experimentally. Since the pioneering work of Cercignani and Daneri [55], different models based on the numerical approximation of the BE [56–58] have been proposed in the literature to describe flows in the transition regime in simple geometries, such as pipes and ducts. In terms of the interaction between gas and solid particles, some expressions for the scaling of the drag force, with respect to the Kn number, experienced by particles immersed in a rarefied gas flow has been obtained [42, 59], also in this case from a numerical solution of the BE. Due to the mathematical complexity of the boundary conditions, these approaches have been successfully applied only to spherical particles in unbounded fluid.

The most important advancement in the understanding and modeling of the drag force on spherical particles in the whole range of Kn comes without doubts from the monumental experimental work of Millikan [60, 61], who performed a fit of the correction function for the drag firstly proposed by Cunningham [62], and later improved by Weber [63]:

$$C(Kn) = 1 + A(Kn) \cdot Kn = 1 + (\alpha + \beta e^{-\gamma/Kn})Kn, \tag{2.89}$$

where A is called the *slip correction parameter*, α, β and γ are characteristic parameters that are somewhat dependent on particle surface and gas characteristics, and

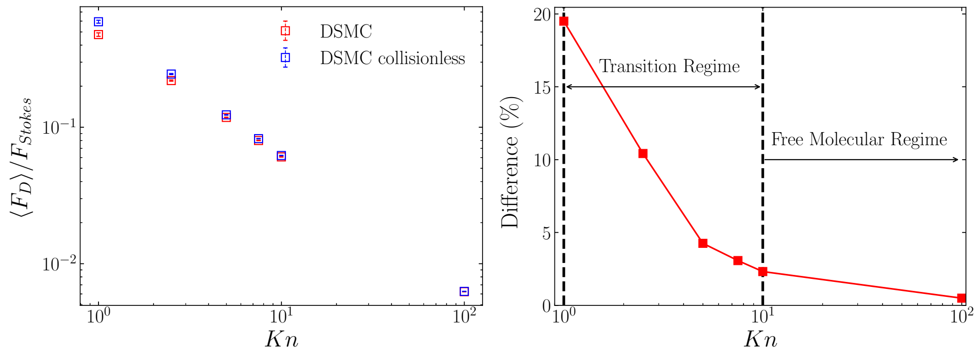

Figure 2.11: On the left: comparison between the drag force experienced by a sphere with radius $R = 0.25\mu$m immersed in an uniform argon gas flow for different values of the particle-based Kn number for the collisional (red squares) and collisionless (blue squares) cases, as obtained from DSMC simulations (more details in Chapter 5). On the right: relative difference between in the drag force between the collisional and the collisionless cases. Intermolecular collisions have an important impact for $1 \leq Kn < 10$, and their effect appears to be negligible for $Kn \geq 100$. Interestingly, for $Kn = 10$, which is considered the beginning of the free molecular regime, a relative difference of about 2.5% is still present between the collisional and the collisionless cases, stating that even at large values of Kn intermolecular collisions might still be relevant.

must be determined experimentally. The drag force on a spherical particle can then be written as the Stokes drag from the continuum regime, given by Eq. (2.44), divided by the correction term from Eq. (2.89):

$$F_D(Kn) = \frac{6\pi\mu R U_\infty}{C(Kn)}. \tag{2.90}$$

Through meticulous measurements of the drag force experienced by micro-metric oil droplets, Millikan obtained a value for the free parameters of $\alpha = 1.209$, $\beta = 0.406$ and $\gamma = 0.893$. A vast effort has been devoted to improve and extend Millikan's measurements [64–68] to a wider range of Kn and gas flows. Among the others, Allan and Raabe [69] proposed and improved version of the Millikan apparatus and measured the drag on micro-metric solid glass particles in a Knudsen range of $0.01 \leq Kn \leq 10$, obtaining the values of $\alpha = 1.142$, $\beta = 0.558$ and $\gamma = 0.999$. A graphical representation of the scaling of the slip correction parameter, A, as a function of Kn is presented in Fig. 2.12.

The drag correction, given by Eq. (2.90), also often referred to as the Cunningham correction, became the standard reference to model rarefaction effects on spherical particles, and has been extensively used in Lagrangian-point particle models [70–73],

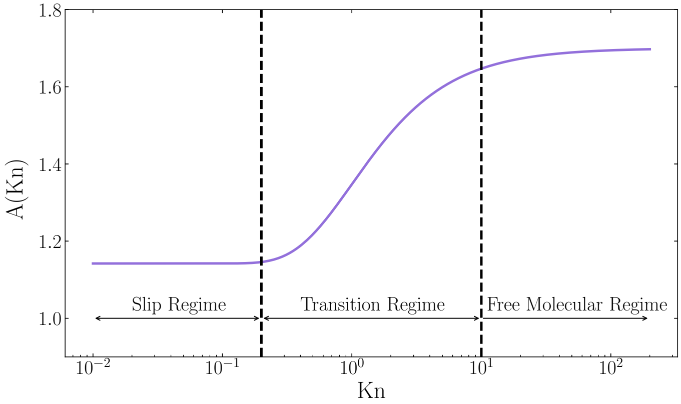

Figure 2.12: Slip factor (solid purple line) A from Eq. (2.89), as a function of Kn using the values of the free parameters of $\alpha = 1.142$, $\beta = 0.558$ and $\gamma = 0.999$, as obtained from Allan and Raabe [69]. The vertical dashed lines represent the conventional separation from the different regimes: slip flow regime for $0.01 \lesssim Kn \lesssim 0.2$, transition regime for $0.2 \lesssim Kn \lesssim 10$ and free molecular regime for $Kn \gtrsim 10$.

as well as to model the correction to the diffusion coefficient in the Brownian motion of point-particles in rarefied conditions [74]. To extend this approach to non-spherical particles, Dahnekë [54, 75] proposed two approaches, the Equivalent Sphere Approximation (ESA) and the Adjusted Sphere Approximation (ASA). The ESA simply consists in the direct application of Eq. (2.90), using an effective radius R_{eff} so that the volume of the particle under investigation matches the one of a sphere with R_{eff} (hence equivalent sphere). This approach is accurate only for slightly non-spherical bodies, and it quickly becomes poor as soon as the particle shape deviates significantly from the spherical shape. Moreover, no influence of the orientation is retained.
The ASA approximation is a more sophisticated approach that consists of the following steps:

1. For a specific body at a given orientation, the correction factor C must be obtained as the ratio between the continuum and the free molecular drag force.

2. The obtained expression for C is equated to the one of the sphere given by Eq. (2.89):

$$C = 1 + (\alpha + \beta e^{-\gamma/Kn_a}) Kn_a, \tag{2.91}$$

where $Kn_a = \lambda/R_a$ is the Knudsen number related to the adjusted sphere with radius R_a still to be determined. It can be obtained with the following relation:

$$\frac{Kn}{Kn_a} = \frac{R_a}{L^*}, \tag{2.92}$$

where L^* is a characteristic length of the body under investigation.

Once the value of the adjusted radius R_a is obtained for a specific body and for the orientation under consideration, the corrections on the drag force over the whole Kn range are obtained by combining Eqs.(2.92) and (2.91). A table with the values of R_a for different bodies and orientation is presented in [75].

While the Cunningham correction is widely used to model the drag force on different bodies with different shapes, any explicit relation to the momentum accommodation coefficient σ, i.e. the dependence on the type of reflections that the gas molecules undergo when they hit the solid surface, is lost. In his experiments, in fact, Millikan assumes that the large majority of reflections is diffusive. This assumption has been later verified by Buckley *et al.* [76], who found that a value for the tangential accommodation coefficient of $\sigma = 0.809$ described Millikan's results with good accuracy. If smaller particles, such as nano-particles, are considered, however, a larger fraction of specular reflections can appear [77], leading to a reduced accuracy of the Cunningham correction. Moreover, the determination of the correction curve in the transient regime is extremely susceptible to small variations in the fit coefficients, so that the accuracy of the Cunningham correction in this regime can vary when used to describe particles with a different material than the ones used for the experimental observations.

When dealing with non-spherical particles, as will be shown later in Chapter 5, the ASA approximation also shows some limitations, as not only it can be applied to the cases where both the continuum and free molecular drag force of the body are known, but it is also less accurate for bodies that highly deviates from the spherical shape, such as oblate spheroids. A large part of this thesis work, presented in Chapters 5 and 6, is devoted to address the possibility to obtain a predictive model for the drag and lift forces on ellipsoidal particles in the transition and free molecular regime using the DSMC method, which is also able to include effects of the momentum accommodation coefficient.

2.6 Concluding remarks

In this Chapter we presented the fundamental concepts behind the statistical description of a gas based on the single particle velocity distribution function and how its evolution in time and space can be modelled through the BE. A fundamental assumption, required to reach a closure of the BE, is that in a dilute gas individual gas molecules are statistically independent so that collisions can be regarded as binary events involving solely two molecules. This physical assumption is called molecular chaos and it allows to simplify the collision operator in the Boltzmann-Equation. From the evaluation of the moments of the BE we then show how to recover the NSE that govern the macroscopic dynamics of fluid parcels, highlighting the limitations (and eventually the breakdown) of such model in presence of rarefaction effects.

In the framework of the continuum description, we present the fundamental theory related to fluid-particles interactions in the Stokes-flow regime, with several examples such as the settling of a sphere in an unbounded fluid, to the rotational dynamics of an ellipsoidal particle in a shear flow, and the sine-squared relation for the drag force, with respect to the orientation, of a body immersed in uniform flow. The physical principle at the basis of the interactions between a fluid and a solid surface is found in the pressure and viscous effects that are ultimately originated from the microscopic interactions between the gas molecules and the surface of the body. Following this principle, we then derive the analytical description for the drag and lift forces, following literature results, in the free molecular regime which is at the opposite extreme of the continuum regime. For this purpose, different particle geometries have been considered. In the free molecular regime, intermolecular collisions can be neglected and analytical calculations can be performed by assuming that the incoming distribution of the gas molecules is unaffected by the molecules that are reflected by the solid body. Particularly relevant for the scope of this thesis work is the preservation of the sine-squared drag law, experienced by an arbitrary-shaped body immersed in a uniform flow, and typical for the continuum regime, also in the free molecular case. This aspect highlights the general validity of this law in the whole spectrum of Knudsen.

The most challenging regime in terms of rarefaction effects is given by the so-called transition regime, which connects the slip flow with the free molecular regime. In these conditions, in fact, rarefaction effects are dominant, but inter molecular collisions cannot be neglected. In the final part of this Chapter we discuss the most important techniques, as well as their limitations, to model the drag experienced by particles in the transition regime starting from the well-known Cunningham correction.

In this thesis work we will first show how to accurately model Stokes flows with the Lattice-Boltzmann method, presenting an improvement of the state-of-the-art algorithm related to the coupling between flow and particles. We will then focus on investigating rarefaction effects on the drag force experienced by different particles through DSMC simulations in the transition and free molecular regimes. Before digging into the main research topics of this thesis work, the fundamental concept at the basis of the aforementioned numerical models will be discussed in the next Chapter.

Chapter 3

Numerical Methods

In this thesis, we will adopt two numerical methods to simulate the interactions between flows and particles in different conditions, namely the Lattice Boltzmann Method (LBM) for flows in the continuum regime and the Direct Simulation Monte Carlo (DSMC) approach for rarefied flows.

This chapter is aimed to provide an introduction to these methods, starting from their connection to the kinetic theory of gases and, more specifically, to the Boltzmann Equation (BE). We first discuss the analogies and differences between the methods in the numerical approximation of the BE, focusing on the detailed explanation of the basic principles behind each approach. Particular attention will then be dedicated to the treatment of the particle-flow coupling algorithms specifically developed in this thesis work. The underlying modeling within each numerical method will be discussed, as well as the validations required to assess their accuracy. In this framework, this chapter contains some of the results published in the papers “Influence of numerical resolution on the dynamics of finite-size particles with the lattice Boltzmann method”, *Phys. Rev. E* **103**, 013303, (2021) and “On the drag and lift coefficients of ellipsoidal particles under rarefied flow conditions”, *Phys. Rev. E* **105**, 015306, (2022).

3.1 Introduction to the LBM and DSMC methods: analogies and differences

Since its first introduction by Bird [33], the DSMC method represents a de-facto standard in the modelling of rarefied gas dynamics and has been used for a wide range of applications. The principal drawback of the method is that it becomes numerically increasingly expensive as the flow approaches to the continuum regime. On the opposite side, the LBM has recently emerged as a powerful and reliable tool to model the Navier-Stokes Equations (NSE). Compared to the DSMC method, the LBM is, in fact, particularly accurate and efficient in modelling a continuum level of description. Examples of few outstanding applications of the LBM are simulations of arterial flows [78, 79], simulations of finite-size particle dynamics at low Reynolds

number [80, 81] and in particle-laden turbulent flows [82–84], as well as investigation of particle transport in micro-channels [85, 86], just to cite some works.
Regardless of their fundamental difference in terms of applications, both methods consist of a technique to approximate numerically the BE and the phase space associated with it. In the DSMC method this is done by "grouping" a large number of real gas molecules into computational particles, which have a given position and velocity. This is analogous to a Lagrangian discretization of the phase space, as the computational particles are free to move ballistically in a continuous physical and velocity space. On the other hand, the LBM adopts an Eulerian discretization of the phase space on the lattice grid, where both spatial and velocity coordinates are discretized. The gas molecules are then represented by components of the single particle Velocity Distribution Function (VDF) f, and they can propagate only along specific directions, defined by the lattice structure. This is equivalent to a mesoscopic representation of the gas dynamics, while the DSMC is a microscopic particle-based system. Both descriptions are equivalent in terms of the macroscopic properties of the flow, and both recover the macroscopic hydrodynamic fields by computing the momenta (or averages) of the distribution function, as sketched in Fig. 3.1.

In both methods, the evolution of the BE in time and space is then approximated

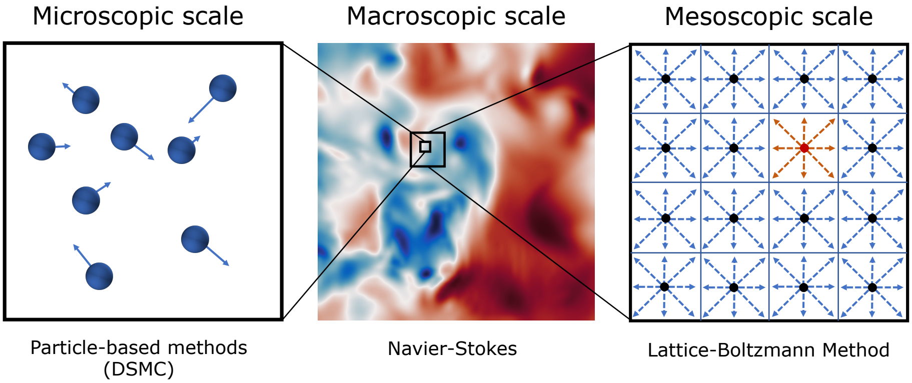

Figure 3.1: Overview of the typical length scales related to different numerical methods. The DSMC is based on a microscopic particle-based representation and, for this reason, becomes unpractical to simulate large scale systems. The LBM bridges the gap between the microscopic description and the macroscopic scales, typically represented through the Navier-Stokes Equations.

through a splitting algorithm scheme. At first, the streaming step (or free flow) in which the collisionless BE is solved over a time interval Δt:

$$\begin{cases} \frac{\partial f_s(\mathbf{r},\mathbf{c},t)}{\partial t} + \mathbf{c} \cdot \nabla f_s(\mathbf{r},\mathbf{c},t) = 0, \\ f_s(\mathbf{r},\mathbf{c},0) = f_0(\mathbf{r},\mathbf{c}), \end{cases} \tag{3.1}$$

where the subscript s refers to the streaming part of f and f_0 is a given initial condition. The streaming step is then followed by the collision step, in which the collision operator C of the BE (see right-hand side of Eq. (2.7)) is taken into account. This is done by solving the space homogeneous BE

$$\begin{cases} \frac{\partial f_c(\mathbf{r},\mathbf{c},t)}{\partial t} = C, \\ f_c(\mathbf{r},\mathbf{c},0) = f_s(\mathbf{r},\mathbf{c},\Delta t), \end{cases} \tag{3.2}$$

using as initial condition the solution from the streaming step calculated from the system of Eqs. (3.1). A schematic representation of the splitting algorithm for the two methods is presented in Fig 3.2.

Behind their evident analogies, the two methods present fundamental dissimilarities in both the streaming and the collision steps, and these dissimilarities are what ultimately distinguish and characterize each individual approach. For what concerns the streaming step, as already anticipated, the most evident difference is the drastic reduction in terms of degrees of freedom that appears in the LBM, as the components of the distribution function can move only along predetermined directions. The capability to recover a Navier-Stokes level of description with such a strong approximation of the velocity space is one of the most surprising features of the LBM, and certainly one of its strengths, as it allows to achieve outstanding numerical efficiency.

The most characteristic feature of the DSMC method, on the other hand, consists in the stochastic treatment of the collision term in the BE, which involves binary collisions between computational particles that are close enough. It has been proved [87] that this approach provides a reliable approximation of the collision term of the BE and, thus, the DSMC is able to capture its complicated effects without the need of numerical modeling of detailed collision processes. The drawback of this approach is that it becomes numerically unfeasible for systems close to the continuum limit and such formulation is adequate only for dilute gases, as it involves only binary collisions. In the LBM, instead, collisions are modeled through a relaxation towards an equilibrium distribution. This relaxation dynamics is generally controlled by a single parameter (the relaxation time), that contains all the information related to the collision process. While this approach is more suited to capture the dynamics of liquids and gases in the continuum regime, it suffers in capturing rarefaction effects. The next sections will provide a more detailed explanation of these numerical schemes.

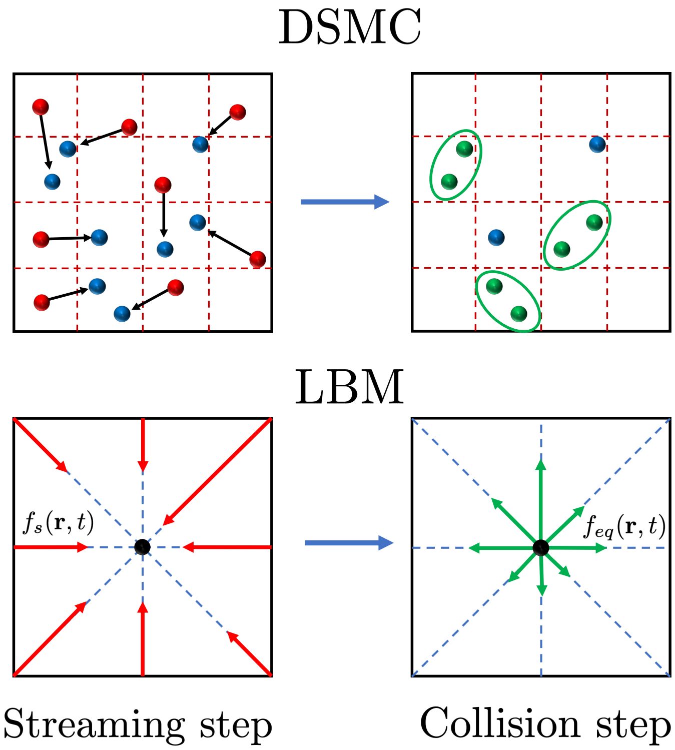

Figure 3.2: Sketch of the splitting scheme adopted by the DSMC and LBM to obtain an approximate solution of the BE, consisting of a streaming step and a collision step. In the former, the DSMC particles are advanced ballistically in the domain, while in the LBM the distribution functions are only allowed to move along specific directions, defined by the lattice typology (in the sketch a standard 2D lattice with 9 discrete speeds is presented). The collision step is instead very different among the two schemes: in the DSMC a stochastic method is used to simulate binary collisions between particles (highlighted in green) residing in the same computational grid cell, while in the LBM the collision step is performed through a relaxation towards the equilibrium distribution, described as f_{eq}.

3.2 Basics of the LBM

The fundamental concept of the LBM is the replacement of the single particle distribution function, $f(\mathbf{x}, \mathbf{c}, t)$, in its discrete counterpart $f_a(\mathbf{x}, t)$, where the subscript a refers to one of the discrete velocities $\mathbf{c}_a$ that characterize the lattice (note the slight change of notation with respect to Chapter 2: here we denote the space coordinates with $\mathbf{x}$, rather than $\mathbf{r}$, as it is more appropriate to describe an Eulerian grid). In fact, the space coordinates $\mathbf{x}$ at which f_a is defined are positioned on a Cartesian lattice, with lattice spacing Δx. Moreover, f_a is defined only at certain times t, separated by a time interval Δt. Typically Δx and Δt are expressed, without loss of generality, in *lattice units*, so that $\Delta x = \Delta t = 1$. There are different possibilities to convert lattice units into physical units, for a detailed explanation of how this process can be performed, we refer the reader to [88]. In few words, one possibility is to associate the lattice grid spacing Δx to a relevant physical unit and derive all the other quantities accordingly using the relation between Δx, Δt, the gas kinematic viscosity ν and the LBM relaxation time, τ. Alternatively, it is possible to exploit the law of similarity by simulating a system in lattice units with the same relevant dimensionless number as the physical system.

The discrete velocities $\mathbf{c}_a$, together with their associated weighting coefficients w_a, form the *velocity sets* $\{\mathbf{c}_a, w_a\}$. These velocity sets are usually denoted by DdQq, where d is the number of spatial dimensions of the lattice and q represents the number of discrete velocities. The most commonly used sets are the D2Q9 and the D3Q19, depicted in Fig. 3.3.

In the framework of the LBM, the BE is approximated in the so-called *lattice Boltzmann Equation* (LBE), which is obtained from a discretization of the BE in space,

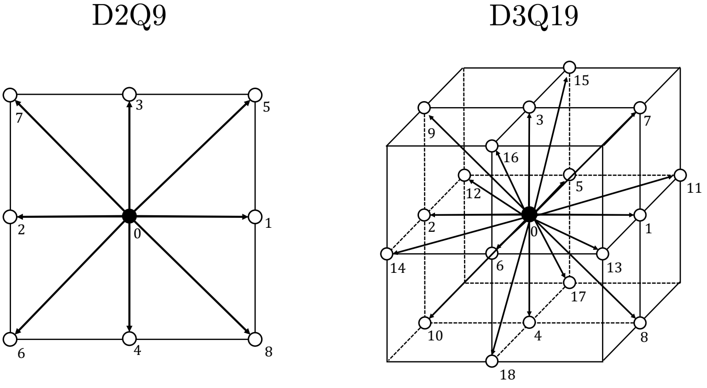

Figure 3.3: Sketch of the D2Q9 (left) and D3Q19 (right) lattice topologies. The space domain is divided into lattice nodes (circles), typically distributed on a Cartesian grid, while the velocity space is discretized along only the directions depicted by the black arrows, so that the population can travel only along the direction prescribed by the velocity sets. The D2Q9 and D3Q19 configurations are mathematically equivalent to a Navier-Stokes level of description, in 2D and 3D, respectively.

velocity and time:

$$f_a(\mathbf{x} + \mathbf{c}_a \Delta t, t + \Delta t) = f_a(\mathbf{x}, t) + \Omega_a(\mathbf{x}, t), \tag{3.3}$$

that expresses the combination of the streaming of the populations f_a to a neighboring lattice node with velocity $\mathbf{c}_a$, with the effects of collisions embodied by the discrete collision operator Ω_a.

The most common and simple collision operator Ω_a that allows to recover a Navier-Stokes level of description is the Bathnagar-Gross-Krook (BGK) operator [89], defined as follows

$$\Omega_a = -\frac{f_a - f_a^{eq}}{\tau} \Delta t. \tag{3.4}$$

The action of this operator is to relax the populations towards a local equilibrium, at a rate that is determined by the relaxation time τ. The local equilibrium is described by the distribution function f^{eq}. This equilibrium distribution function is obtained via a Taylor expansion in the limit small velocity (expressed in lattice units) of the Maxwell-Boltzmann distribution, see Eq. (2.22):

$$f_a^{eq} = w_a \rho \left[1 + \frac{\mathbf{c}_a \cdot \mathbf{u}}{c_s^2} + \frac{3(\mathbf{c}_a \cdot \mathbf{u})^2 - u^2}{2c_s^2} \right], \tag{3.5}$$

where the weights w_a are chosen depending on the velocity set, c_s is the lattice speed of sound, also depending on the choice of the velocity set, and ρ and $\mathbf{u}$ are the values of the macroscopic density and velocity, respectively, on the lattice node at position $\mathbf{x}$. The macroscopic hydrodynamic fields, in fact, are computed in the same way as they were obtained using the distribution function f (see Chapter 2), i.e. by computing the momenta of the discrete distribution function. The only difference is that the integral from Eq. (2.2) now is represented by a discrete sum over the populations a:

$$\rho(\mathbf{x}, t) = \sum_a f_a(\mathbf{x}, t), \tag{3.6}$$

$$\rho \mathbf{u}(\mathbf{x}, t) = \sum_a \mathbf{c}_a f_a(\mathbf{x}, t). \tag{3.7}$$

By combining Eq. (3.3) with Eq. (3.4), we obtain the LBE-BGK in its final form:

$$f_a(\mathbf{x} + \mathbf{c}_a \Delta t, t + \Delta t) = f_a(\mathbf{x}, t) - \frac{f_a(\mathbf{x}, t) - f_a^{eq}(\mathbf{x}, t)}{\tau} \Delta t. \tag{3.8}$$

Like any collision operator, the BGK operator must conserve mass and momentum, so that

$$\sum_a \left(f_a(\mathbf{x},t) - f_a^{eq}(\mathbf{x},t)\right) = 0; \qquad \sum_a \mathbf{c}_a \left(f_a(\mathbf{x},t) - f_a^{eq}(\mathbf{x},t)\right) = 0. \tag{3.9}$$

The great advantage of the BGK collisional operator is that it allows to approximate the complicated collision integral from the BE in terms of known variables, the populations f_a and the equilibrium populations f_a^{eq}. This operation allows to successfully capture not only gas behavior, but also liquids, for which the collision operator from Eq. (2.7) is not strictly valid as, due to the significantly larger densities, molecules in liquid can undergo more complicated interactions involving three and more particles. The consequence of having a single relaxation time, however, leads to some important limitations, such as that all gas diffusivities correspond to the same numerical value [37]. Moreover, as it will be discussed later, this simple treatment of the collision operator introduces spurious effects, which are detrimental for the numerical accuracy. To overcome such limitations, and improve the reliability of the LBM, more sophisticated collision operators have been proposed, such as the Multi-Relaxation Time (MRT) [90] or the Projection-Based Regularized LBM [91]. In this work we will adopt the latter, which will be discussed later in this Section.

From the LBE to Navier-Stokes: the Chapman-Enskog expansion

After having introduced the LBE-BGK in Eq. (3.8), it remains to show that it actually recovers the NSE from a rigorous point of view. The most common method to accomplish this task, closely following the derivation presented in [88] is to exploit the Chapman-Enskog analysis [92–95], which consists in a perturbation expansion of f_a around the equilibrium distribution, f_a^{eq}, with the Knudsen number as expansion parameter:

$$f_a = f_a^{eq} + Kn f_a^{(1)} + Kn^2 f_a^{(2)} + \dots . \tag{3.10}$$

The accurate procedure to show how to obtain NSE from the LBE-BGK is rather complex and here we will focus on the main passages and fundamental concepts. For a thorough derivation we refer to the textbook of Krüger [88], or the thesis work of Viggen [96]. By performing a Taylor expansion of Eq. (3.8) and by subtracting from the result the operator $(\Delta t/2)(\partial_t + c_{a\alpha}\partial_\alpha)$ applied to the equation itself (to remove second-order derivative terms), we obtain the equation that will be used for the rest of this analysis:

$$\Delta t(\partial_t + c_{a\alpha}\partial_\alpha) f_a = -\frac{\Delta t}{\tau} f_a^{neq} + \Delta t(\partial_t + c_{a\alpha}\partial_\alpha)\frac{\Delta t}{2\tau} f_a^{neq}, \tag{3.11}$$

where $f_a^{neq} = (f_a(\mathbf{x},t) - f_a^{eq}(\mathbf{x},t))$ represents the non-equilibrium contribution to f_a and all terms of order $\mathcal{O}(\Delta t^3)$ have been neglected. The next step is to also expand the time and space derivatives (in what is often called a multi-scale expansion):

$$\partial_t = Kn\partial_t^1 + Kn^2\partial_t^2 + \mathcal{O}(Kn^3), \tag{3.12}$$

$$\partial_\alpha = Kn\partial_\alpha^1 + \mathcal{O}(Kn^2). \tag{3.13}$$

By applying both expansions of f_a from Eq. (3.11) and Eqs. (3.12)-(3.13), and by separating the resulting relation into terms of different order in Kn, we obtain

$$\mathcal{O}(Kn): \qquad \left(\partial_t^{(1)} + c_{a\alpha}\partial_\alpha^{(1)}\right) f_a^{eq} = -\frac{1}{\tau} f_a^{(1)}, \tag{3.14}$$

$$\mathcal{O}(Kn^2): \qquad \partial_t^{(2)} f^{eq} + \left(\partial_t^{(1)} + c_{a\alpha}\partial_\alpha\right)\left(1 - \frac{\Delta t}{2\tau}\right) f_a^{(1)} = -\frac{1}{\tau} f_a^{(2)}. \tag{3.15}$$

Before proceeding with the derivation, we need to introduce the assumption, following the conservation relations from Eq. (3.9), that also the momenta of the higher order terms in f_a vanish [97]

$$\sum_a f_a^{(n)} = 0; \qquad \sum_a \mathbf{c}_a f_a^{(n)} = 0. \tag{3.16}$$

In this way, we can easily compute the zeroth (mass) and first (momentum) moments of Eqs. (3.14)- (3.15) to obtain the relations in terms of the density ρ and the velocity $\mathbf{u}$. By doing so, and then by summing the different order in the mass and momentum equations, we obtain

$$\left(Kn\partial_t^{(1)} + Kn^2\partial_t^{(2)}\right)\rho + Kn\partial_\alpha^{(1)}(\rho u_\alpha) = 0, \tag{3.17}$$

$$\left(Kn\partial_t^{(1)} + Kn^2\partial_t^{(2)}\right)(\rho u_\alpha) + Kn\partial_\beta^{(1)}\Pi_{\alpha\beta}^{eq} = -Kn^2\partial_\beta^{(1)}\left(1 - \frac{\Delta t}{2\tau}\right)\Pi_{\alpha\beta}^{(1)}. \tag{3.18}$$

The general expression of the momentum flux tensors $\mathbf{\Pi}$, as a function of f_a, is given by:

$$\Pi_{\alpha\beta}^{eq} = \sum_a c_{i\alpha} c_{a\beta} f_a^{eq}, \tag{3.19}$$

$$\Pi_{\alpha\beta}^{(1)} = \sum_a c_{i\alpha} c_{a\beta} f_a^{(1)}. \tag{3.20}$$

The perturbation moment from Eq. (3.20) is related to the viscous stress tensor $\boldsymbol{\tau}$ by

$$\tau_{\alpha\beta} = -\left(1 - \frac{\Delta t}{2\tau}\right)\Pi^{(1)}_{\alpha\beta}. \tag{3.21}$$

The explicit derivation of $\mathbf{\Pi}^{(1)}$ in terms of the macroscopic variables is the last missing element to reconnect with the NSE. For the complete derivation, which requires quite some algebra, we refer the reader to [88], while here we will just present the final result, valid for the isothermal equation of state and for a second order expansion of f^{eq}_a:

$$\Pi^{(1)}_{\alpha\beta} = -\rho c_s^2 \tau \left(\partial^{(1)}_{\beta} u_\alpha + \partial^{(1)}_{\alpha} u_\beta\right) + \tau \partial^{(1)}_{\gamma}(\rho u_\alpha u_\beta u_\gamma). \tag{3.22}$$

The first term in the right-hand side of Eq. (3.22) represents the Navier-Stokes viscous stress tensor from Eq. (2.17), while the second term represents an $\mathcal{O}(u^3)$ arising from having limited the expansion of f^{eq} to the second order in u. By inspecting this term, it is evident that the $\mathcal{O}(u^3)$ is negligible if $u^2 \ll c_s^2$, which corresponds to the weakly compressible limit.

By inserting Eq. (3.22) (neglecting the third-order error term) into Eqs. (3.17)-(3.18) and by reversing the derivative expansion, we finally re-obtain the NSE as in Eqs. (2.15)-(2.16):

$$\partial_t \rho + \partial_\alpha(\rho u_\alpha) = 0, \tag{3.23}$$

$$\partial_t(\rho u_\alpha) + \partial_\beta(\rho u_\alpha u_\beta) = -\partial_\alpha P + \partial_\beta\Big[\mu(\partial_\beta u_\alpha + \partial_\alpha u_\beta)\Big], \tag{3.24}$$

with pressure, P, and dynamic viscosity, μ, given by

$$P = \rho c_s^2, \tag{3.25}$$

$$\mu = \rho c_s^2\left(\tau - \frac{\Delta t}{2}\right). \tag{3.26}$$

This result, additionally, allows to connect the lattice relaxation time τ with the viscosity of the fluid, showing that $\tau > \Delta t/2$ is a necessary condition to ensure the positiveness of μ and thus a stable simulation.

Hermite expansion and regularization procedure

From the previous paragraph, we have derived the LBE-BGK formulation and showed how it can recover a Navier-Stokes level of description. We introduced the Single-Relaxation time BGK operator, discussing its advantages and some of its limitations.

In this paragraph we show how to derive a more advanced collision operator that allows to further improve the accuracy of our simulations. The starting point is to observe that, following the approach originally proposed by Grad [98], the distribution function f can be expressed as a series of the orthonormal Hermite polynomials (which form a complete basis) in the velocity space $\mathbf{c}$:

$$f(\mathbf{x}, \mathbf{c}, t) = \omega(\mathbf{c}) \sum_{n=0}^{\infty} \frac{1}{n!} \mathbf{a}^{(n)}(\mathbf{x}, t) \mathcal{H}^{(n)}(\mathbf{c}), \tag{3.27}$$

where $\mathbf{a}^{(n)}(\mathbf{x}, t)$ and $\mathcal{H}^{(n)}(\mathbf{c})$ are the n-th rank symmetric expansion coefficient and the Hermite polynomial tensors, respectively, and $\omega(\mathbf{c})$ are the weight functions, also called generating functions, as they allow to construct all the Hermite polynomials:

$$\omega(\mathbf{c}) = \frac{1}{(2\pi)^{d/2}} e^{-\mathbf{c}^2/2}, \tag{3.28}$$

$$\mathcal{H}^{(n)}(\mathbf{c}) = (-1)^n \frac{1}{\omega(\mathbf{c})} \nabla^{(n)} \omega(\mathbf{c}), \tag{3.29}$$

where d represents the dimensionality of the problem.
The most valuable feature of the expansion in the Hermite Basis (HB) is that the expansion coefficients, $\mathbf{a}^{(n)}(\mathbf{x}, t)$, are directly connected to the conserved hydrodynamic moments. By definition, in fact, the expansion coefficients are given by:

$$\mathbf{a}^{(n)}(\mathbf{x}, t) = \int f(\mathbf{x}, \mathbf{c}, t) \mathcal{H}^{(n)} d\mathbf{c}, \tag{3.30}$$

and by carrying out the computation for the first three moments, we obtain that they correspond to the corresponding order hydrodynamic moment:

$$\mathbf{a}^{(0)} = \int f d\mathbf{c} = \rho, \tag{3.31}$$

$$\mathbf{a}^{(1)} = \int f \mathbf{c} d\mathbf{c} = \rho \mathbf{u}, \tag{3.32}$$

$$\mathbf{a}^{(2)} = \int f \mathbf{c}\mathbf{c} d\mathbf{c} = \mathbf{P} + (\mathbf{u}^2 - \mathbf{I}). \tag{3.33}$$

This represents a powerful result, since it shows that to reproduce the relevant physics (i.e. to satisfy the conservation laws at a macroscopic level), the first three terms of the Hermite series expansion are sufficient. Another important result is that, due to the orthonormality of the HB, a truncation of the expansion to the N-th order will preserve the leading N moments, allowing to approximate f by its projection onto the subspace spanned by these leading moments:

$$f(\mathbf{x}, \mathbf{c}, t) \approx f^N(\mathbf{x}, \mathbf{c}, t) = \omega(\mathbf{c}) \sum_{n=0}^{N} \frac{1}{n!} \mathbf{a}^{(n)}(\mathbf{x}, t) \mathcal{H}^{(n)}(\mathbf{c}). \tag{3.34}$$

Now we need to connect the formulation based on the expansion on the HB with the LBE and its discretization of the velocity space. This can be done through the Gauss-Hermite quadrature [99], which allows to convert exactly the continuous integral of Eq. (3.30) into a weighted discrete sum. In order to apply this technique, we need first to replace f in Eq. (3.30) by its truncation to the N-th order. In this way the integrand can be written as

$$f^N(\mathbf{x}, \mathbf{c}, t) \mathcal{H}^{(n)} = \omega(\mathbf{c}) p(\mathbf{x}, \mathbf{c}, t), \tag{3.35}$$

where $p(\mathbf{x}, \mathbf{c}, t)$ is a polynomial with degree $\leq 2N$. By applying the Gauss-Hermite quadrature to Eq. (3.30), where the integrand is substituted with Eq. (3.35), we can express the expansion coefficient as a discrete sum over the discrete velocity set $\mathbf{c}_a$

$$\mathbf{a}^{(n)} \approx \int f^N(\mathbf{x}, \mathbf{c}, t) \mathcal{H}^{(n)} d\mathbf{c} = \sum_{a=0}^{q} \frac{w_a}{\omega(\mathbf{c}_a)} f^N(\mathbf{x}, \mathbf{c}_a, t) \mathcal{H}^{(n)}(\mathbf{c}_a), \tag{3.36}$$

where w_a and $\mathbf{c}_a$ are the weights and abscissae of a Gauss-Hermite quadrature of a degree $\leq 2N$ and, as it will be clear later, can be chosen as velocity set for the LBE. By defining $f_a(\mathbf{x}, t) = w_a f^N(\mathbf{x}, \mathbf{c}_a, t)/\omega(\mathbf{c}_a)$, we can write the moments of the truncated distribution as

$$\rho = \sum_{a=0}^{q} f_a, \tag{3.37}$$

$$\rho \mathbf{u} = \sum_{a=0}^{q} f_a \mathbf{c}_a, \tag{3.38}$$

$$\mathbf{P} + \rho \mathbf{u^2} = \sum_{a=0}^{q} f_a \mathbf{c}_a \mathbf{c}_a, \tag{3.39}$$

$$\tag{3.40}$$

which represents the typical way to compute the macroscopic hydrodynamics moment in the LBM, showing that the LBE formalism is recovered if the truncated distribution function is used.

The same procedure can be applied to the equilibrium distribution function, f^{eq}, and its explicit expression for an isothermal system and up to the second order of expansion in the HB, reads

$$f_a^{eq} = w_a \rho \left[1 + \frac{\mathbf{c}_a \cdot \mathbf{u}}{c_s^2} + \frac{3(\mathbf{c}_a \cdot \mathbf{u})^2 - u^2}{2c_s^2} \right]. \tag{3.41}$$

This expression coincides with Eq. (3.5), which is instead obtained by the Taylor expansion around zero fluid velocity. This approach, however, not only allows to control the order of accuracy by retaining higher-order terms, but also shows that the equilibrium distribution of the LBM lies entirely on the subspace spanned by the Hermite Polynomials. This last aspect is of particular relevance, as it allows to understand one important source of error in the standard BGK collisional operator.
The usual LBGK approach, in fact, when viewed as a projection of the continuum BGK-BE into the N-th order Hermite Basis, $\mathbb{H}^N$, introduces an error in relation to the non-equilibrium distributions f^{neq} that appear in the BGK operator, differently from their equilibrium counterpart, do not automatically lie within the same sub-space. This leads to the presence of numerical artifacts from the higher order moments that cannot be accurately evaluated with the velocity sets in use. The Projection-based Regularization (PR) procedure, first introduced and discussed in [91], allows to overcome this problem by ensuring that also the non-equilibrium component of the discrete distribution function belongs entirely to $\mathbb{H}^N$, in order to stabilize the LBM and e.g. reduce numerical slip effects at fluid-solid interfaces.
The PR procedure has been extensively described in several previous works [91, 100], so here we will provide just the most important features. The discrete velocity distribution function is split into two components:

$$f_a = f_a' + f_a^{eq}, \tag{3.42}$$

where f_a' is the non-equilibrium part of the total distribution. Since f^{eq} already lies entirely on the subspace spanned by the first N Hermite polynomials, the PR procedure allows to convert this non-equilibrium part into the new distribution $\hat{f}_a'$ which lies in the same subspace. The components of the discrete velocity distribution function thus read:

$$f_a^{eq} = w_a \rho \left[1 + \frac{\mathbf{c}_a \cdot \mathbf{u}}{c_s^2} + \frac{3(\mathbf{c}_a \cdot \mathbf{u})^2 - u^2}{2c_s^2} \right], \tag{3.43}$$

$$\hat{f}_a' = w_a \sum_{n=0}^{N} \frac{1}{n!} \mathbf{a}^{(n)} \mathcal{H}^{(n)}(\mathbf{c}_a), \quad a = 0, \ldots, d-1, \tag{3.44}$$

$$\mathbf{a}^{(n)} = \sum_{a=1}^{d} f'_a \mathcal{H}^{(n)}(\mathbf{e}_a), \quad n = 0, \ldots, N, \tag{3.45}$$

where N must be chosen accordingly to the maximum order of expansion provided by the Gauss-Hermite quadrature. The D3Q19 scheme allows a complete projection up to $N = 2$, such that weakly-incompressible, isothermal flows are completely recovered at a Navier-Stokes level of description, meaning that when a no-slip rule is applied on a solid boundary, the slip velocity at its surface should be identically zero. Since the first two Hermite coefficients vanish due to the vanishing contribution from the non-equilibrium distributions to mass and momentum, the projection of the non-equilibrium distributions is given by

$$\hat{f}'_a = w_a \frac{\mathcal{H}^{(2)}(\mathbf{c}_a)}{2} \sum_{b=1}^{d} f'_b \mathbf{c}_b \mathbf{c}_b. \tag{3.46}$$

This method has already been applied to a large variety of flows, including multi-component flow applications [101] and rarefied gas flows [102], demonstrating its capability to improve the accuracy and stability of standard LBM simulations.

In the context of the present work, we adopt the PR-LBM because of its ability to suppress the residual numerical slip that we expect to appear around the particle in cases where its dimension is small compared to the lattice grid. It has been indeed shown [43] that for a planar Poiseuille channel flow discrete effects related to the nature of the LBM produce a numerical slip at the fluid-wall interfaces. The slip velocity produced on the walls of the channel, using a standard LBM model with Bounce-Back rule at the boundaries (boundary treatment and relative nomenclature will be further explained later), is

$$U_s = \frac{32}{\pi} Kn^2 - \frac{1}{L^2}, \tag{3.47}$$

where

$$Kn = \sqrt{\frac{\pi}{2}} c_s \frac{\tau - 0.5}{L} \tag{3.48}$$

is the Knudsen number and L is a characteristic spatial length of the simulated system. As shown in Fig. 3.4, using a PR-LBM it is possible to strongly suppress the numerical slip at walls, even if some small slip still appears for large values of Kn. In Chapter 4, we will address simulations involving spherical particles suspended in unbounded fluid. In such conditions, the characteristic spatial length L will be replaced by the typical size of the particle and while an analytical relation such as Eq. (3.47) for the numerical slip around the particle is missing for curved boundaries, we expect the PR-LBM to reduce such effects when compared to a standard LBM scheme.

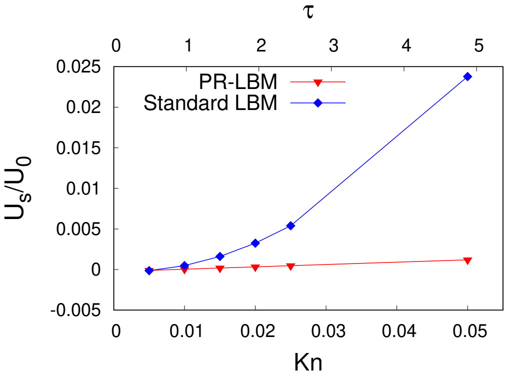

Figure 3.4: Comparison of the slip velocity at the walls, U_s, normalized with respect to the center channel velocity, U_0, of a rectangular $2D$ Poiseuille channel flow for standard LBM (blue diamonds) and for Projection-based Regularized LBM (PR-LBM, red triangles), as a function of Kn (bottom axis) and τ (top axis), for a fixed channel width, $L = 64$. When a strict no-slip boundary condition on the walls is imposed, the slip velocity should be identically zero at any Kn number, but due to the discrete nature of the LBM a numerical slip velocity can appear. A PR-LBM strongly suppresses the numerical slip produced at the channel walls, especially for large values of Kn.

3.3 Fluid-surface interactions in the LBM: no-slip conditions for particle-transport algorithm

The formulation of boundary conditions in the LBM is typically non-trivial, as they apply to the mesoscopic populations f_a, rather than to the macroscopic variables of interest, such as ρ and $\mathbf{u}$, as it is done for standard NS solvers. This introduces more degrees of freedom related to the non-uniqueness of the problem, which ultimately led to the formulation of a large number of LBM boundary conditions.

We will start the discussion with the half-way Bounce-Back (BB) scheme [103–105], which represents the most common way to model fluid-surface interactions in the LBM. During the streaming step, if a component of the velocity distribution function, f_a, meets a rigid boundary, it will be reflected back to its original location with its velocity reversed, so that

$$f_{\bar{a}}(\mathbf{x}_i, t + \Delta t) = f_a(\mathbf{x}_i, t), \tag{3.49}$$

where $\mathbf{x}_i$ represents a fluid node adjacent a solid nodes, represented with $\mathbf{x}_b$, and the subscript $\bar{a}$ refers to the velocity direction opposite to a. The application of Eq. (3.49) to all the fluid nodes, a macroscopic no-slip velocity condition is obtained for a wall located mid-way on the link between lattice nodes.

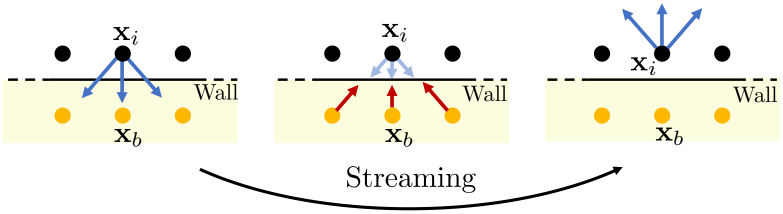

Figure 3.5: Sketch of the time evolution of the half-way Bounce-Back method. The arrows represent the different components of f_a that are impinging on a solid wall located half-way between the fluid node $\mathbf{x}_i$ and the solid nodes $\mathbf{x}_b$. During one single streaming step, these components of the velocity distribution are reversed (red arrows) and applied to the corresponding fluid node. In this way a no-slip boundary condition is enforced on the solid wall.

According to the original works by Ladd [104, 106] and by Aidun [107], solid particles (and non-deformable droplets) can be modeled as finite volumes enclosed by moving boundaries suspended in the fluid domain. Fluid-solid interactions are addressed via no-slip boundary conditions applied at the particle surface. Momentum exchange between the fluid and solid lattice nodes at the interface is used to compute the force and the torque exerted on the solid particle. Newton's equation of motion for the particle can then be directly integrated to update the particle position and velocity. While this method has been successfully applied to simulate many particle-laden flows, its principal drawback lies in the introduction of discretization effects from the particle representation on the lattice grid. This imposes an approximation of the exact location of the surface of the particle, which is commonly found in between the fluid and solid nodes. In the most common approach, when a standard Bounce-Back (BB) no-slip rule is applied at the interface, the particle is approximated by a "rough" stair-case shape (as sketched by the blue solid line in Fig. 4.8) leading to a reconstruction of the hydrodynamics around the particle that is, in general, only first-order accurate [108].

Several studies can be found in the literature offering various improvements for particle discretization. Bouzidi *et al.* [109], Lallemand *et al.* [110] and Ginzburg *et*

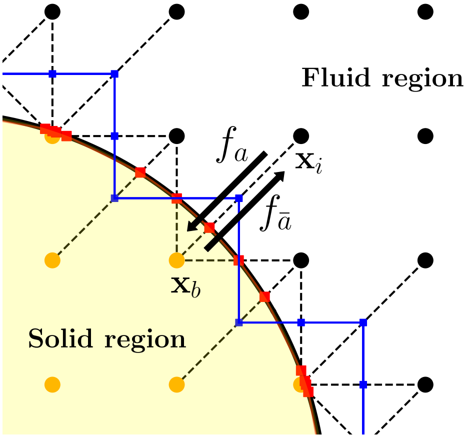

Figure 3.6: Sketch of a spherical particle representation on the lattice grid. The radius of the particle is set to 2.5 lattice units. Momentum exchange is calculated for every fluid node ($\mathbf{x}_i$) and its adjacent solid nodes ($\mathbf{x}_b$) along the fluid-solid links (black dashed lines). The inward component along the direction a of the velocity distribution function f interacts with the surface of the particle during the streaming from $\mathbf{x}_i$ to $\mathbf{x}_b$ and the outward component in the direction $\bar{a}$ is generated. Using standard BB, the interaction point is approximated in the middle position of the fluid-solid link (blue squares), while using an interpolation method the surface of the particle is evaluated in its exact location (red squares).

al. [111] propose different techniques to treat curved and moving boundaries based on second-order accurate interpolation schemes. While improving the accuracy of the BB rule and conserving stability, all these methods require additional fluid nodes along the fluid-solid link in order to apply interpolation successfully. Chun *et al.* [108] consider interpolation of the equilibrium distribution only, keeping the second-order accuracy without the need of extra fluid nodes along the fluid-solid links. Kao *et al.* [112] proposed a new interpolation-free treatment of the fluid-boundary interaction based on local grid refinement. This approach improves accuracy while reducing the effects of mass fluctuations typical of interpolated schemes related to the reconstruction of the velocity distribution function, at the price of increased complexity and computational load.

On-grid particle description is not the only approach to describe particle transport in the LBM. Wu and Aidun [113] enforced a no-slip boundary condition on the external surface of the solid particle based on the External Boundary Force (EBF) approach developed by Goldstein *et al.* [114]. The EBF method consists in the application of a force density to the fluid domain to force the difference between the fluid and the solid velocity at the boundary nodes to be zero, resulting in smoother fluid-solid interactions with respect to the standard BB.

Niu *et al.* [115] investigated the possibility to implement a momentum exchange-based method by using two unrelated meshes using the Immersed Boundary Method (IBM) firstly proposed by Peskin [116], without however increasing the accuracy with respect to standard approaches. A comprehensive comparison between interpolation and IBM is addressed by Peng *et al.* in [117], where it is found that while interpolated schemes are in general more accurate, IBM efficiently suppresses force and torque fluctuations on the particle due to the different representation of the particle surface on the lattice grid. For the scope of this work, we use an on-grid description to investigate and compare the accuracy provided by different fluid-solid interaction models following the algorithm introduced by Aidun *et al.* [107], which combines a Lagrangian description of the solid particle with the LBM solver for the fluid phase.

The momentum contribution of a fluid grid point in contact with the solid particle is obtained by the summation of the inward and outward momentum for each fluid-solid link given by

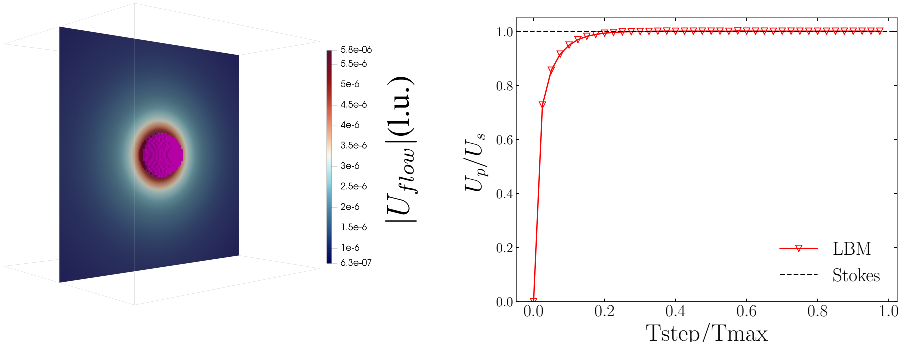

Figure 3.7: Section of the flow velocity field (in LBM lattice units) from a 3D LBM simulation around a settling spherical particle in unbounded fluid (left) and plot of the particle velocity, U_p, normalized with the Stokes settling velocity, U_s, as a function of time. The particle discretization on the lattice grid is evident from the left figure, however, using EI it is possible to capture the physical position of the surface of the particle and recover the correct settling velocity with great accuracy. To obtain accurate simulations of unbounded fluid an advanced boundary treatment at the simulation box is required and it will be discussed in Chapter 4.

$$\mathbf{p}_a = \mathbf{e}_a(f_a(\mathbf{x}_b, t) + f_{\bar{a}}(\mathbf{x}_i, t)), \tag{3.50}$$

where we denote with the subscript b a node belonging to the solid, i a fluid node in the vicinity of b and with a the velocity direction pointing from i to b. The subscript

$\bar{a}$ refers to the velocity direction opposite to a, as shown in Fig. 4.8.

Since the particle is moving across the lattice grid, two extra sources of momentum must be taken into account, namely the momentum gained by the particle when covering new fluid nodes and the momentum lost by the particle when uncovering a (former) solid node [107].

Once the total momentum exchange between the fluid and the solid particle is evaluated, the equations of motion of the particle are integrated through a leapfrog scheme to update its translational and rotational velocity, position and orientation [104, 107]. The outward momentum, i.e. from solid to fluid, given by $f_{\bar{a}}(\mathbf{x}_i, t)$ in Eq. (3.50), is obtained by enforcing a no-slip rule on the particle surface. Such condition can be applied through different boundary condition schemes. In this work we focus on an accuracy comparison between the BB rule, which leads to a stair-case approximation of the surface of the particle, and the Equilibrium Interpolation (EI) scheme [108] which allows to correctly detect the particle surface at its actual position on the fluid-solid link. The EI method consists in applying a BB rule to the non-equilibrium component of the velocity distribution function

$$f'_{\bar{a}}(\mathbf{x}_i, t + \Delta t) = f'_a(\mathbf{x}_i, t), \tag{3.51}$$

while a linear interpolation is applied to the equilibrium part as follows:

$$f^{(0)}_{\bar{a}}(\mathbf{x}_i, t + \Delta t) = 2q f^{(0)}_a(\mathbf{x}_i, t) + (1 - 2q) f^{(0)}_a(\mathbf{x}_i - \mathbf{e}_a, t), \quad \text{for } 0 \leq q < 1/2, \tag{3.52}$$

$$f^{(0)}_{\bar{a}}(\mathbf{x}_i, t + \Delta t) = \frac{1}{2q} f^{(0)}_a(\mathbf{x}_i, t) + \frac{2q - 1}{2q} f^{(0)}_{\bar{a}}(\mathbf{x}_i, t), \quad \text{for } 1/2 < q \leq 1, \tag{3.53}$$

where q denotes the distance of the fluid node to the solid boundary (non-dimensionalized by the grid spacing). In this work, the exact value of q is evaluated through the ray-sphere intersection algorithm described in [118]. We discuss our approach to describe the two-way coupling between flow and particle in Appendix B, where we also mention in detail the implementation of our ray-traced technique to evaluate q.

The effects of moving boundaries on the fluid are taken into account by adding to the right-hand side of Eqs. (3.52) and (3.53) an additional term $\delta f_{\bar{a}}$ proportional to the velocity $\mathbf{u}_b$ at boundary node b. Following the scheme proposed by Bouzidi *et al.* [109], first-order contributions from the motion of the boundary are given by:

$$\delta f_{\bar{a}} = 2 w_a \mathbf{e}_a \cdot \mathbf{u}_b, \qquad \text{if } q < 1/2, \tag{3.54}$$

$$\delta f_{\bar{a}} = \frac{1}{q} w_a \mathbf{e}_a \cdot \mathbf{u}_b, \qquad \text{if } q \geq 1/2. \tag{3.55}$$

An application example of the algorithm described in this Section is presented in Fig. 3.7, where the settling of a spherical particle in unbounded fluid is simulated and the settling velocity from Eq. (2.48) is recovered with great accuracy. The details on how to simulate open boundaries in Stokes-flow conditions, as well as an in-depth accuracy analysis of the moving-boundaries algorithm presented in this paragraph will be addressed in Chapter 4.

3.4 Basics of the DSMC method

The DSMC represents another method, or better, a family of methods, to approach the solution of the BE. In this thesis work, we use an algorithm based on the classic approach originally developed by Bird [33] called No Time Counter (NTC) algorithm. The performances achieved by the DSMC in resolving complex flows led to a rapid rise of the approach's popularity in the scientific community, to the point that it has been addressed as "the dominant predictive tool in rarefied gas dynamics of the past decade" [119].

Besides the NTC, other common schemes have been proposed in the literature to approximate the collision operator in the BE, such as the time counter [120], the majorant collision frequency [121] and the Bernoulli scheme [122]. We chose the NTC for the good compromise between accuracy and numerical efficiency that the scheme offers. In the rest of this Section, we will go through the basic concept of the DSMC method, referring the reader to specific textbooks [33, 123] for a more detailed view on the topic.

In this approach, the real gas molecules are approximated by a finite set of N model particles denoted by their positions, $\mathbf{x}_i$ and velocities, $\mathbf{c}_i$, that move and collide in a physical space domain. These computational molecules are representative (or parliament) particles that embody a large number of real physical gas molecules, so that the total dynamics of the real system is described in the simulation by this parliamentary subset and binary intermolecular collisions and interactions with solid boundaries are modeled through a stochastic approach. The time evolution for the computational molecules is then split in two separate parts: a streaming step and a collision step. During the streaming step, the position of the molecules is updated ballistically and, during the update, the boundary conditions are taken into account.

Streaming step

During this phase, the position of the particles is updated ballistically accordingly to their microscopic velocity and the imposed timestep, as sketched in Fig. 3.2. If external forces are absent, the equation of motion of the particles can be integrated through a standard Euler scheme:

$$\mathbf{x}_i(t + \Delta t) = \mathbf{x}_i(t) + \mathbf{c}_i \Delta t. \tag{3.56}$$

In this framework, it is important to set the value of Δt to an appropriate value in order to achieve meaningful results. From a physical point of view, in fact, it is necessary that the numerical time step has a value comparable to the molecular collision characteristic time, i.e. $\Delta t \sim \lambda/v$, where v represents a relevant microscopic velocity such as the most probable velocity $v_{mp} = (2k_B T/m)^{1/2}$. Following the standard approach proposed by Bird [33], a stricter relation is applied to enforce that during a single time step, the particles can travel for only a fraction of the computational grid they are occupying:

$$\Delta t < \frac{1}{4} \cdot \frac{\Delta x}{(v_{mp} + U_f)}, \tag{3.57}$$

where U_f is the estimated flow velocity and Δx is the spatial dimension of the computational cell. The relation in Eq. (3.57) ties together Δt and Δx, so that an accuracy requirement must be also defined for the spatial resolution. The standard rule-of-thumb relation [33, 123] on the cell size L_c is that it must be a fraction of the gas mean free path:

$$L_c \leq 0.3\lambda. \tag{3.58}$$

It is interesting to notice that Eq. (3.58) is analogous to impose that the cell-based Knudsen number $Kn_{cell} = \lambda/L_c \geq 3$. This relation can be used within to define an adaptive refinement of the DSMC grid to ensure that (3.58) is respected also in complex flows with large pressure variations.
The combination of Eqs. (3.57) and (3.58) force the computational particles residing in a single DSMC cell to undergo a sufficient number of collision within one mean free path distance.

Collision step

To address the intermolecular collisions [33], the physical simulation domain is divided into a computational grid and the DSMC molecules within the same grid cell undergo stochastic binary collisions, where the post-collision velocities of the two molecules involved in a single collision event, $\mathbf{c}_1^*$ and $\mathbf{c}_2^*$, are obtained by imposing the detailed balance of momentum and energy during the collision:

$$\text{Momentum conservation:} \quad m_1\mathbf{c}_1 + m_2\mathbf{c}_2 = m_1\mathbf{c}_1^* + m_2\mathbf{c}_2^* = (m1+m2)\mathbf{c}_{cm} \tag{3.59}$$

$$\text{Energy conservation:} \quad m_1\mathbf{c}_1^2 + m_2\mathbf{c}_2^2 = m_1\mathbf{c}_1^{*2} + m_2\mathbf{c}_2^{*2} \tag{3.60}$$

$$\text{Relative velocity:} \quad |\mathbf{c}_r| = |\mathbf{c}_1 - \mathbf{c}_2| = |\mathbf{c}_r^*| = |\mathbf{c}_1^* - \mathbf{c}_2^*|, \tag{3.61}$$

where $\mathbf{c}_{cm}$ and $\mathbf{c}_r$ are the center of mass and relative velocities, respectively. The last ingredient required to evaluate the post-collision relative velocity, $\mathbf{c}_r^*$, is the collision solid angle. This angle depends on the specific interaction model chosen to describe the single intermolecular binary collisions The two most common model choices are the Hard-Sphere (HS) and Variable-Hard-Sphere (VHS) models, for which the scattering is isotropic in the center of mass reference frame. The expression for $\mathbf{c}_r^*$ in the HS and VHS models reads

$$\mathbf{c}_r^* = |\mathbf{c}_r| \left[(\sin\chi \cos\Phi)\hat{\mathbf{x}} + (\sin\chi \sin\Phi)\hat{\mathbf{y}} + \cos\chi\hat{\mathbf{z}} \right], \tag{3.62}$$

where the azimuthal angle, Φ is uniformly distributed between 0 and 2π, while the elevation angle, χ is distributed accordingly to

$$P(\chi)d\chi = \frac{1}{2}\sin\chi d\chi. \tag{3.63}$$

Finally, after sampling the collision angle, the post-collision velocities are obtained as:

$$\mathbf{c}_1^* = \mathbf{c}_{cm} + \left(\frac{m_2}{m_1+m_2}\right)\mathbf{c}_r^*; \;\; \mathbf{c}_2^* = \mathbf{c}_{cm} - \left(\frac{m_1}{m_1+m_2}\right)\mathbf{c}_r^*. \tag{3.64}$$

Once the collisional dynamics is defined, the total number of colliding pairs within every computational DSMC grid cell can be calculated. Every DSMC molecule has a collision probability given by the NTC scheme [33]:

$$P = F_N \sigma_T c_r \Delta t / V_c, \tag{3.65}$$

where F_N is the kinetic resolution, i.e. the number of real molecules represented by a single computational molecule, σ_T is the collision cross-section, c_r is the magnitude of the relative velocity between the colliding molecules, Δt is the computational time step and V_c is the volume of the DSMC grid cell. The total number of intermolecular collisions that are imposed in every DSMC cell can be defined [123] as:

$$M_{coll} = \frac{N_c(N_c-1)F_N\sigma_T c_r^{max}\Delta t}{2V_c}, \tag{3.66}$$

where N_c is the total number of DSMC molecules contained in the DSMC cell and c_r^{max} the maximum relative velocity between pairs of molecules inside the cells. The collision pairs are then selected through an acceptance-rejection algorithm with probability given by Eq. (3.65).

In this work we describe the intermolecular interactions using the Variable Hard-Sphere (VHS) model, in which, following Bird [33], σ_T is given by:

$$\sigma_{T,VHS} = \pi d^2 \frac{\left(\frac{2k_B T}{m c_r^2}\right)^{\omega - 0.5}}{\Gamma(2.5 - \omega)}, \tag{3.67}$$

where d is the molecular diameter at the reference temperature T, k_B is the Boltzmann constant, m is the molecular mass, Γ is the gamma-function and ω is the viscosity coefficient used to recover the correct scaling of the viscosity, with respect to the temperature, in the VHS model. For argon gas (which will be the gas used in Chapters 5 and 6) the reference quantities are [33] $T = 273.15$K, $d = 4.17 \cdot 10^{-10}$m, $m = 6.63 \cdot 10^{-26}$kg and $\omega = 0.81$.

In the rest of this work we will define λ according to Phillips [42] as:

$$\lambda = \frac{2\mu}{v_{th}\rho}, \tag{3.68}$$

where μ is the dynamic viscosity of the gas, $v_{th} = (8k_B T/\pi m)^{1/2}$ is the mean thermal velocity for a gas molecule with temperature T, mass m and density ρ. In the VHS model μ is defined as:

$$\mu_{VHS} = \mu(T/T_{ref})^{\omega}, \tag{3.69}$$

where for argon gas $\mu = 2.12 \cdot 10^{-5}$ kg m^{-1}s^{-1} [33] at the reference temperature.

Evaluation of macroscopic fields

In the DSMC method, macroscopic flow properties are typically evaluated after the streaming and collision steps by performing statistical sampling of the microscopic quantities and, for this reason, they always result in being fluctuating fields. In our approach, we employ volume-averaged measurements on each individual DSMC computational cell, so that for a generic microscopic property, Q, its average value on a specific cell is defined as:

$$\langle Q(\mathbf{c}) \rangle = \frac{1}{S}\sum_{s=1}^{S}\frac{1}{V_c}\sum_{i=1}^{N_c} Q(\mathbf{c_i}), \tag{3.70}$$

where S is the total number of samples. In order to obtain correct measurements, individual samples must be statistically independent, requiring that a certain amount of time intervals (typically on the order of 10) must separate the acquisition of different samples. The standard hydrodynamic moments are then obtained following Eq. (3.70):

$$\rho = \langle m \rangle, \tag{3.71}$$

$$\mathbf{u} = \langle m\mathbf{c} \rangle, \tag{3.72}$$

$$T = \frac{2m}{3k_B\rho}\left(\frac{1}{2}\langle mc^2\rangle - \frac{1}{2}\rho|\mathbf{u}|^2\right), \tag{3.73}$$

$$\sigma_{\alpha\beta} = \langle m(c_\alpha - u_\alpha)(c_\beta - u_\beta)\rangle. \tag{3.74}$$

The statistical error on the average values is then obtained following the equilibrium statistical mechanics theory [124], so that, for example, the relative error on the density and on the velocity components of a dilute gas are given by

$$E_\rho = \frac{\sqrt{\langle(\delta N)^2\rangle}}{\sqrt{S N_0}} = \frac{1}{\sqrt{S N_0}}, \tag{3.75}$$

$$E_{u_x} = \frac{\sqrt{\langle(\delta u_x)^2\rangle}}{\sqrt{S N_0}} = \frac{1}{\sqrt{S N_0}}\frac{1}{Ma\sqrt{\gamma}}, \tag{3.76}$$

where N_0 is the average number of particles per cell, $Ma = u/c_s$ is the Mach number defined in Eq. (2.29) with the speed of sound $c_s = \sqrt{\gamma RT}$ and $\gamma = c_P/c_V$ is the ratio of the specific heats. In this way, in order to obtain the desired accuracy, it is sufficient to set the parameters S and N_0 accordingly.

3.5 Fluid-surface interactions in the DSMC: boundary conditions and cut-cell method

During the streaming step, interaction with solid boundaries must be taken into account. In this work we follow the model proposed by Maxwell [51], where collisions at the solid interface are either diffusive, specular, or a combination of both. This approach allows to mimic real gas-surface interactions using simplified mechanisms, in the absence of a complete theoretical model. A sketch of the aforementioned models is presented in Fig. 3.8.

The evaluation of gas-surface interactions requires the calculation of two fundamental elements that are common to both boundary conditions: the collision point between the gas molecule and the solid surface, and the value of the residual time, Δt^*, that the molecule needs to travel after reflection. In the specular model, then, the velocity component normal to the solid surface of the incoming gas molecule is reversed, as

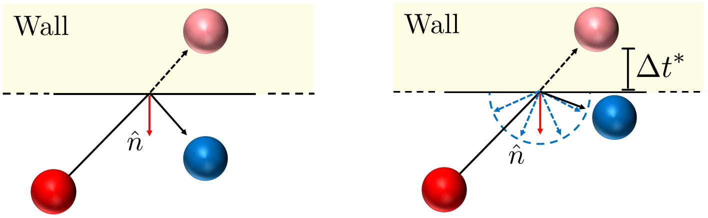

Figure 3.8: Sketch of the Maxwell gas-solid interactions in the DSMC method. An incoming particle (red) that hits a solid surface gets reflected either via specular bouncing (left), where the velocity along the normal direction with respect to the surface $\hat{n}$ (red arrow) is reversed and the tangent one is the same, or via a diffuse bouncing (right) where the particle is reflected in a probabilistic manner following Eqs. (3.77)-(3.79). The post-collision velocity is calculated accordingly to the residual time, Δt^*, the incoming particle would have spent in the solid volume before applying the desired bouncing, as well as wall properties such as velocity and temperature.

it would happen for a perfectly smooth surface. In the diffuse wall model, instead, the wall is treated as a rough surface and the gas molecule post-collision velocity components are sampled from a biased Maxwell distribution in the frame of reference of the wall. The probability distributions for every component, assuming a collision with the upper wall orthogonal to the $\hat{\mathbf{x}}$ direction as depicted in Fig. 3.8, are given by

$$P(c_x) = -\frac{m}{k_B T_w} c_x e^{-\frac{m c_x^2}{2 k_B T_w}}, \tag{3.77}$$

$$P(c_y) = \sqrt{\frac{m}{2 k_B T_w}} e^{-\frac{m (c_y^2 - U_{w,y})^2}{k_B T_w}}, \tag{3.78}$$

$$P(c_z) = \sqrt{\frac{m}{2 k_B T_w}} e^{-\frac{m (c_z^2 - U_{w,z})^2}{k_B T_w}}, \tag{3.79}$$

where T_w and U_w are the wall temperature and translational velocity. Once the post-collision velocity components are computed, the gas molecule is streamed by a time Δt^* from the collision point on the solid surface. The residual time Δt^* can be evaluated by simply comparing the portion of the trajectory the particle traveled inside the solid body with the one in which the particle traveled in the fluid volume.

In addition to the boundary conditions applied at the gas-solid interface, also the simulation domain boundaries need to be considered. More complicated boundary conditions can be employed to the simulation boundaries, such as pressure or free-streaming boundary conditions, where particles are continuously generated and removed at the boundaries to prescribe a certain pressure or flow velocity. In this thesis work we will apply to the simulation boundaries a combination of free-streaming, based on the open-boundary conditions which implementation in our DSMC code is described by Di Staso [20], and periodic boundary conditions.

The boundary conditions described in this Section to model interactions with solid walls can be extended to model the interactions between the gas flow and fully-resolved solid ellipsoidal particles immersed into it. In the following, we will present our implementation of this technique, called the cut-cell method. Similarly to what we did for the LBM particle-transport algorithm, the surface of the particle immersed in the gas domain is described by its analytical expression through the approach discussed in Appendix B. The momentum exchange between the gas and the solid particle is then computed from the microscopic interactions between the simulated gas molecules and the solid surface, where we use the same ray-sphere intersection algorithm [118] employed for the LBM to detect the collision points at which the DSMC molecules impinge on the surface of the solid particle (see Appendix B). In this way, we overcome the limitations of the alternative method used to evaluate the force and the torque on the particle based on the macroscopic stress tensor, which is often less accurate due to the statistical fluctuations of the higher-order macroscopic fields around the particle.

For each DSMC molecule i hitting the surface of the solid particle at position $\mathbf{x}_i$, with initial momentum $\mathbf{p}_i$ and post-collision momentum $\mathbf{p}_i'$, the total momentum transferred from the gas to the solid particle within a single time step Δt is:

$$\Delta \mathbf{p} = \sum_i \left(\mathbf{p}_i - \mathbf{p}_i' \right) , \tag{3.80}$$

from which the total force $\mathbf{F}$ and torque $\mathbf{T}$, exerted on the rigid body, can be directly obtained:

$$\mathbf{F} = \sum_i \left(\frac{\mathbf{p}_i - \mathbf{p}_i'}{\Delta t} \right) , \tag{3.81}$$

$$\mathbf{T} = \sum_i \left[(\mathbf{x}_i - \mathbf{X}) \times \frac{(\mathbf{p}_i - \mathbf{p}_i')}{\Delta t} \right] , \tag{3.82}$$

where $\mathbf{X}$ denotes the center of mass of the solid particle. While in this work we only perform DSMC simulations of particles that are fixed in space, Eqs. (3.81) and (3.82) can be used to update the solid particle translational and angular velocities, position and orientation in the same way we did for the LBM case.

Since a portion of the domain is occupied by the solid volume of the particle, the simulation grid is divided in three regions: gas cells completely filled with gas molecules, solid cells that are completely occupied by the solid particle and boundary cells (cut cells) that are partially covered by the solid particle and partially filled with gas, as sketched in Fig. 3.9. In order to correctly evaluate the collision probability given by Eq. (3.65) within the boundary cells, the local cell volume with gas has to be calculated. We perform this update by marking the cells close to the solid particle, so that only the marked cells are candidates for being boundary cells. The gas volume of the boundary cells is then evaluated through a Monte Carlo approach: a set of N_t random points is generated in the DSMC boundary cell and the gas fraction volume, V_g, is obtained as:

$$V_g = V_c - V_s = \frac{N_t - N_s}{N_t} V_c, \tag{3.83}$$

where N_s represents the number of points that are generated inside the solid volume and V_s is the volume fraction of a DSMC cell occupied by the solid volume. The relative error at which the solid volume fraction of the boundary cells is computed can be expressed as [125]:

$$\varepsilon_{rel} = \frac{V_p - \sum_{all\ cells} V_s}{V_{p,\ bound.\ cells}}, \tag{3.84}$$

where V_p is the real (analytic) volume of the solid particle and $V_{p,\ bound.\ cells}$ is the real volume of the solid fraction of all boundary cells. The numerator represents the difference between the real volume of the particle and the computational volume as calculated from the Monte Carlo approach, which ultimately describes the difference in volume in the boundary cells. The denominator represents the real volume of only the boundary cells, and this can be obtained by subtracting to V_p the volume of the DSMC cells completely occupied by the solid particle. In this way, we can define an estimator of the accuracy at which the total volume of the boundary cells is computed. The scaling of the relative error in Eq. (3.84), with respect to different resolutions of a spherical particle with radius R (in cell units) is plotted in Fig. 3.10 for different values of the Monte Carlo trials N_t. It is shown that using a sufficiently large number of Monte Carlo trials, the volume of the boundary cells is recovered with an accuracy of at least $\sim 95\%$ also for particles with a radius that is only a fraction of the simulation grid size. Since in this work we focus on particles that are fixed in space, the gas volume fraction of the boundary cells can in principle be computed analytically. We prefer, however, to keep our approach general using the Monte Carlo approach, as it can be directly applied to different grids, particle shapes and moving objects. Moreover, using fixed particles, the volume fraction evaluation of the boundary cells needs to be performed only once and we set $N_t = 100000$ to ensure a very high precision of the computation. It is worth mentioning that in cases where the particle is allowed to move, the volume computation must be performed at each time step and

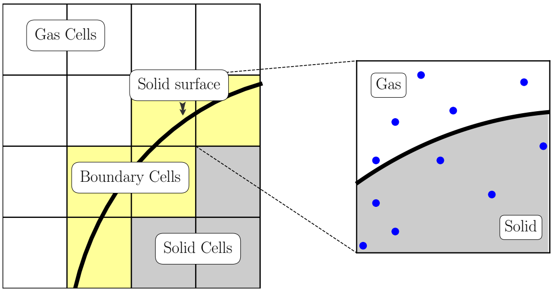

Figure 3.9: Sketch of the decomposition of the DSMC computational grid in cells occupied only by the gas (white), cells completely occupied by the solid particle (gray) and boundary cells (yellow) partially occupied by both the gas and the solid. These boundary cells are cut by the surface of the simulated particle (black curved line) and the volume fraction occupied by the gas must be calculated in order to obtain the correct intermolecular collision probability. In this work we use a Monte Carlo approach to evaluate the gas and solid volume fractions of the boundary cells: a set of random points N_t (blue dots) is generated in each boundary cell and the final solid volume fraction of the cell is given by the ratio between the points belonging to the solid region and the total number of points generated in the boundary cell, as defined in Eq. (3.83).

a lower number of N_t would allow a faster computation.

The cut-cell algorithm implemented and presented in this study has been incorporated in the parallel DSMC solver validated by Di Staso [20]. The intensive computations required for the DSMC simulations presented in this work, in fact, can become feasible only by taking advantage of parallel computation. This can be easily done for a DSMC algorithm, thanks to the locality of the interactions between gas molecules, by enforcing a three-dimensional Cartesian processor grid on which the DSMC simulation domain is decomposed.

3.6 Concluding remarks

In this Chapter we introduced and extensively discussed the numerical methods used in this thesis work, namely the LBM and DSMC, starting from the fundamentals to conclude with the particle transport algorithms that will be used in the next Chapters. We show that due to the shared roots in the kinetic theory, the two methods have several similarities, but also fundamental differences that ultimately make the LBM ideal for flow in the continuum regime and DSMC, on the other hand, to address rarefied flows.

Starting from the LBM, we discuss its theoretical foundations and rigorously derive its

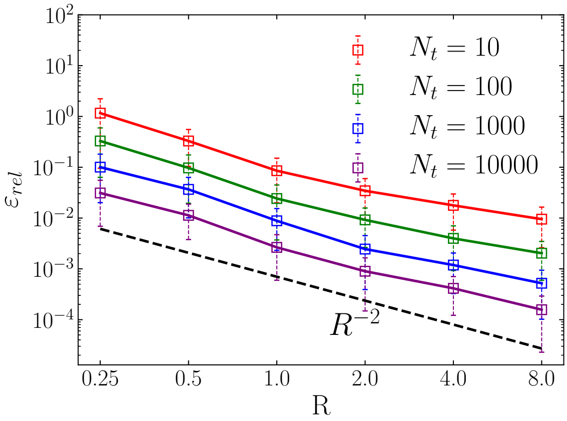

Figure 3.10: Relative error, as defined in Eq. (3.84), in the evaluation of the boundary cell solid volume using a Monte Carlo approach as a function of the radius of the particle, R (cell units), for different values of the Monte Carlo trials N_t. The solid volume fraction of the boundary cells is reproduced with an accuracy higher than 90% for $N_t \geq 1000$ also in cases where the solid particles are very small when compared with the DSMC grid. The scaling of the error with respect to the numerical resolution of the particle is second-order. The error bars are calculated as the standard deviation calculated on a sample of 100 independent measurements.

connection to the Boltzmann Equation and the Navier-Stokes level of description. We then focus on the boundary treatment employed to describe fully-resolved particles in the framework of the LBM boundary conditions, showing how the standard approach to model flat walls can be generalized for ellipsoidal particles. Similarly, we introduce the DSMC method, presenting its basics principles and the connection between microscopical and macroscopic quantities. We then again focus on the two-way coupling algorithm developed in this work to model the interactions between gas flows and solid ellipsoidal particles.

In the following of this work we will employ such numerical schemes to investigate fundamental aspects of the interactions between particles and flows in different conditions.

3.7 Appendix A: lattice weights and Hermite Polynomials

In this appendix we provide the values of the lattice velocities e_a and relative weights w_a for the D3Q19 and D3Q27 lattice stencils, followed by the explicit expression of the Hermite Polynomials required for the full second-order expansion of the PR-LBM adopted in this work:

$$\begin{aligned}
\boldsymbol{e}^{D3Q19} =& [\boldsymbol{e}_0, ..., \boldsymbol{e}_{18}] && (3.85)\\
=& \left[\begin{matrix} 0 & & 1 & & -1 & & 0 & & 0 & 0 & & 0 & & 1 & & 1 & & -1 & \\ 0 & , & 0 & , & 0 & , & 1 & , & -1 & 0 & , & 0 & , & 1 & , & -1 & , & 1 & , \\ 0 & & 0 & & 0 & & 0 & & 0 & 1 & & -1 & & 0 & & 0 & & 0 & \end{matrix}\right. \\
& \left.\begin{matrix} -1 & & 1 & & -1 & & 1 & & -1 & & 0 & & 0 & & 0 & & 0 \\ -1 & , & 0 & , & 0 & , & 0 & , & 0 & , & 1 & , & 1 & , & -1 & , & -1 \\ 0 & & 1 & & 1 & & -1 & & -1 & & 1 & & -1 & & 1 & & -1 \end{matrix}\right], && (3.86)
\end{aligned}$$

$$\begin{aligned}
\boldsymbol{w}^{D3Q19} =& \left(\frac{1}{3}, \frac{1}{18}, \frac{1}{18}, \frac{1}{18}, \frac{1}{18}, \frac{1}{18}, \frac{1}{18}, \frac{1}{18}, \frac{1}{18},\right. \\
& \left.\frac{1}{18}, \frac{1}{36}, \frac{1}{36}, \frac{1}{36}, \frac{1}{36}, \frac{1}{36}, \frac{1}{36}, \frac{1}{36}, \frac{1}{36}, \frac{1}{36}\right), && (3.87)
\end{aligned}$$

$$\begin{aligned}
\boldsymbol{e}^{D3Q27} =& [\boldsymbol{e}_0, ..., \boldsymbol{e}_{26}] && (3.88)\\
=& \left[\begin{matrix} 0 & & 1 & & -1 & & 0 & & 0 & 0 & & 0 & & 1 & & 1 & & -1 & \\ 0 & , & 0 & , & 0 & , & 1 & , & -1 & 0 & , & 0 & , & 1 & , & -1 & , & 1 & , \\ 0 & & 0 & & 0 & & 0 & & 0 & 1 & & -1 & & 0 & & 0 & & 0 & \end{matrix}\right. \\
& \begin{matrix} -1 & & 1 & & -1 & & 1 & & -1 & & 0 & & 0 & & 0 & & 0 & \\ -1 & , & 0 & , & 0 & , & 0 & , & 0 & , & 1 & , & 1 & , & -1 & , & -1 & , \\ 0 & & 1 & & 1 & & -1 & & -1 & & 1 & & -1 & & 1 & & -1 & \end{matrix} \\
& \left.\begin{matrix} 1 & & 1 & & 1 & & -1 & & 1 & & -1 & & -1 & & -1 \\ 1 & , & 1 & , & -1 & , & 1 & , & -1 & , & -1 & , & 1 & , & -1 \\ 1 & & -1 & & 1 & & 1 & & -1 & & 1 & & -1 & & -1 \end{matrix}\right], && (3.89)
\end{aligned}$$

$$\begin{aligned}
\boldsymbol{w}^{D3Q19} =& \left(\frac{8}{27}, \frac{2}{27}, \frac{2}{27}, \frac{2}{27}, \frac{2}{27}, \frac{2}{27}, \frac{2}{27}, \frac{1}{54}, \frac{1}{54},\right. \\
& \frac{1}{54}, \frac{1}{54}, \frac{1}{54}, \frac{1}{54}, \frac{1}{54}, \frac{1}{54}, \frac{1}{54}, \frac{1}{54}, \frac{1}{54}, \frac{1}{54} \\
& \left.\frac{1}{216}, \frac{1}{216}, \frac{1}{216}, \frac{1}{216}, \frac{1}{216}, \frac{1}{216}, \frac{1}{216}, \frac{1}{216}\right). && (3.90)
\end{aligned}$$

The Hermite Polynomials of order n, $\mathcal{H}^{(n)}(\boldsymbol{e})$, up to the second order, read:

$$\mathcal{H}^{(0)}(\boldsymbol{e}) = 1, \tag{3.91}$$

$$\mathcal{H}_i^{(1)}(\boldsymbol{e}) = e_i, \tag{3.92}$$

$$\mathcal{H}_{ij}^{(2)}(\boldsymbol{e}) = e_i e_j - \delta_{ij}, \tag{3.93}$$

where δ_{ij} is the Kronecker delta function.

3.8 Appendix B: Two-way coupled representation of ellipsoidal particles

In this Appendix we will present the mathematical formulation on which our two-way coupled particle transport algorithm are based. This approach has been implemented in both the LBM and DSMC method to model the physical boundaries of the solid particles suspended in the fluid domain.
Two Cartesian coordinate systems are employed: the inertial frame, (x, y, z), attached to the computational domain, and the body-centered frame (x', y', z') which is instead attached to the center of mass of the particle and is aligned along the principal direction of inertia of the particle. To transform the inertial frame into the body-centered frame, firstly we perform a negative translation of $\mathbf{X} = (X, Y, Z)$, representing the coordinates of the center of mass of the particle. A sketch of the collision detection algorithm is shown in Fig. 3.11.

The translation is followed by a rotation defined by the matrix M:

$$M = \begin{pmatrix} q_0^2 + q_1^2 - q_2^2 - q_3^2 & 2(q_1 q_2 + q_0 q_3) & 2(q_1 q_3 - q_0 q_2) \\ 2(q_1 q_2 - q_0 q_3) & q_0^2 - q_1^2 + q_2^2 - q_3^2 & 2(q_2 q_3 + q_0 q_1) \\ 2(q_1 q_3 + q_0 q_2) & 2(q_2 q_3 - q_0 q_1) & q_0^2 - q_1^2 - q_2^2 + q_3^2 \end{pmatrix}, \tag{3.94}$$

where we use the four quaternion variables

$$q_0 = \cos(\theta/2)\cos((\Phi + \Psi)/2), \tag{3.95}$$

$$q_1 = \sin(\theta/2)\cos((\Phi - \Psi)/2), \tag{3.96}$$

$$q_2 = \sin(\theta/2)\sin((\Phi - \Psi)/2), \tag{3.97}$$

$$q_3 = \cos(\theta/2)\sin((\Phi + \Psi)/2), \tag{3.98}$$

defined from the Euler angles (θ, Φ, Ψ) sketched in Fig. 3.12. A final transformation is then enforced to ensure that in the final reference system (x', y', z') any generic

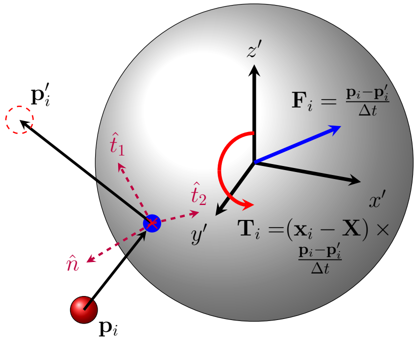

$\mathbf{p}_i'$
z'
$\mathbf{F}_i = \frac{\mathbf{p}_i-\mathbf{p}_i'}{\Delta t}$
$\hat{t}_1$
$\hat{t}_2$
x'
y'
$\mathbf{T}_i = (\mathbf{x}_i - \mathbf{X}) \times \frac{\mathbf{p}_i-\mathbf{p}_i'}{\Delta t}$
$\hat{n}$
$\mathbf{p}_i$

Figure 3.11: Sketch of the gas-solid interaction scheme. An impinging gas molecule i (red sphere) with initial momentum $\mathbf{p}_i$ hits the surface of the solid particle (gray sphere) and undergoes a diffusive reflection with post-collisional momentum $\mathbf{p}_i'$, where the collision point (red cross) is evaluated exactly in the body-centered reference system (x', y', z'). Then, the reflections are computed in the reference system formed by the normal and tangent unit vectors, $(\hat{n}, \hat{t_1}, \hat{t_2})$, with respect to the surface of the particle. Finally, the post-collisional poistion and velocity is transformed back in the inertial reference system.

ellipsoidal particle is described as a spherical particle with unitary radius. Such stretch along the main axes is represented by the matrix S:

$$S = \begin{pmatrix} 1/a & 0 & 0 \\ 0 & 1/b & 0 \\ 0 & 0 & 1/c \end{pmatrix}, \tag{3.99}$$

where a, b and c are the radii of the ellipsoidal particle. The final transformation equation for a generic point $\mathbf{x}$ in the inertial reference frame into its equivalent $\mathbf{x}'$ in the stretched body-centered frame thus reads

$$\mathbf{x}' = SM(\mathbf{x} - \mathbf{X}). \tag{3.100}$$

We then apply Eq. (3.100) to transform the pre- and post-streaming positions $\mathbf{x_0}$ and $\mathbf{x_f}$ of the impinging molecules (for the DSMC) or distribution functions (for the LBM)) in the body-centered stretched reference system:

$$\mathbf{x}_0' = SM(\mathbf{x}_0 - \mathbf{X}), \tag{3.101}$$

$$\mathbf{x}_f' = SM(\mathbf{x}_f - \mathbf{X}). \tag{3.102}$$

Then, the ray-sphere intersection algorithm simply consists in the evaluation of the intersections between the unit radius sphere centered in the origin (which represents the transformed particle) and the parametric line, $L(t)$, passing from $\mathbf{x}_0'$ and $\mathbf{x}_f'$ with unitary direction $\mathbf{v}'$, given by

$$L(t) = \mathbf{x}_0' + t\mathbf{v}'. \tag{3.103}$$

The intersection points are found by substituting the generic point on the sphere with a generic point on the line $L(t)$ and resolving for the free parameter t. The final quadratic equation reads

$$(\mathbf{v}' \cdot \mathbf{v}')t^2 + 2(\mathbf{v} \cdot \mathbf{x}_0')t + (\mathbf{x}_0' \cdot \mathbf{x}_0') = 1, \tag{3.104}$$

whose solutions, t_1 and t_2, allow to calculate the intersection points by inserting them into Eq. (3.103). To ensure the selection of the correct collision points, only the values of t_1 and t_2 that satisfy the condition $||L(t) - \mathbf{x_0}'|| \leq ||\mathbf{x_f}' - \mathbf{x_0}'||$ are considered. If both points respect this condition, then the point closer to $\mathbf{x_0}'$ is chosen. The reflection scheme is then applied in the reference system formed by the normal and tangent unit vectors, with respect to the surface of the particle, with origin in the collision point and given by $(\hat{n}, \hat{t_1}, \hat{t_2})$. In this way the collision routine is equivalent as the one employed for a planar wall.

It is possible to extend the algorithm to particles with different shapes by employing a different ray-surface intersection algorithm and its relative coordinates transformation. Some examples on such intersection algorithms for the most common shapes, such as boxes, cones and triangles can be found in [118]. Ultimately, a particle with a complex shape can be described by an opportune combination of these known shapes, and intersections can be found using the appropriate ray-surface intersection scheme for each one of the constituent basic shapes, separately. In the more general case, a triangulation of the surface can be applied and then use a ray-triangle intersection scheme.

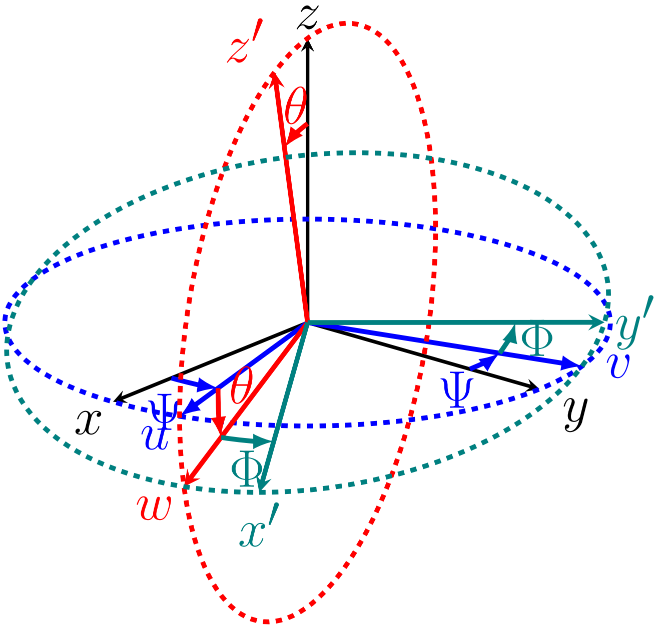

Figure 3.12: Euler angles representation. Any rotation of the coordinate system (x, y, z) (black) can be described by a precession rotation around the axis z by an angle Ψ, which leads to the auxiliary system (u, v, z) (blue), followed by a nutation rotation of an angle θ around the axis v to obtain the second auxiliary system (w, u, z') (red) and finally by a rotation of Φ around z' to obtain the reference system (x', y', z') (green).

Chapter 4

Influence of numerical resolution on the dynamics of finite-size particles with the Lattice Boltzmann Method

In this Chapter we investigate and compare the accuracy and efficiency of different numerical approaches to model the dynamics of finite-size particles using the Lattice Boltzmann Method (LBM) described in Chapter 3, namely the standard Bounce-Back (BB) and the Equilibrium Interpolation (EI) schemes. To accurately compare the different implementations, we firstly introduce a novel boundary condition to approximate the flow properties of an unbounded fluid in a finite simulation domain, taking into account the perturbation induced by a moving particle. We show that this novel boundary treatment is efficient in suppressing detrimental effects on the dynamics of spherical and ellipsoidal particles arising from the finite size of the simulation domain. We then investigate the performances of the BB and EI schemes in modeling the dynamics of a spherical particle settling under Stokes conditions, which can now be reproduced with great accuracy thanks to the novel treatment of the exterior boundary. We find that the EI scheme outperforms the BB scheme in providing a better accuracy scaling with respect to the resolution of the settling particle, while suppressing finite-size effects due to the particle discretization on the lattice grid. Additionally, in order to further increase the capability of the algorithm in modeling particles of sizes comparable to the lattice spacing, we propose an improvement to the EI scheme, the *Complete Equilibrium Interpolation* (CEI). This new approach allows to accurately capture the boundaries of the particle also when located between two fluid nodes. We evaluate the CEI performance in solving the dynamics of an under-resolved particle under analogous Stokes conditions and also for the case of a rotating ellipsoid in a shear flow. Finally, we show that EI and CEI are able to recover the correct flow solutions also at small, but finite, Reynolds number. Adopting the CEI scheme it is not only possible to detect particles with zero lattice occupation, but also to increase up to one order of magnitude the accuracy of the dynamics of particles with a size comparable to the lattice spacing with respect to the BB and the EI schemes. The material presented in this chapter closely follows the results and exposition presented in the publication "Influence of numerical resolution on the dynamics of finite-size particles with the Lattice Boltzmann Method", *Phys. Rev. E* **103**, 013303, 2021.

The rest of the Chapter is structured as follows: the introduction to the research context is firstly discussed in Section 4.1. In Section 4.2 the problem of reproducing ideal Stokes flow for the settling of a spherical particle is addressed and results related to particle resolution analysis for different fluid-solid interaction models are presented. We investigate the performances for the same interaction models in resolving the angular dynamics of an ellipsoid in a shear flow at low Reynolds number in Section 4.3. We summarize and discuss our results in Section 4.4.

4.1 Introduction

As briefly discussed in the Introduction (Chapter 1) of this thesis, particle and droplet transport phenomena in complex flows are crucial for many environmental, industrial and medical applications. Examples include droplets, aerosol and particle transport in turbulent flows [126, 127], but also in red blood cells flow in plasma [128] or contamination from particle debris in next generation lithography machines [129]. This topic is nowadays also extremely relevant in relation with the COVID-19 pandemic [130, 131].

To cope with such a wide spectrum of applications, an increasingly growing effort from the scientific community is devoted towards the development of accurate and efficient numerical methods. Over the past decades, the Lattice Boltzmann Method (LBM) [37, 132] emerged as an efficient and reliable tool to address a large variety of flows, including particle-laden ones [133].

In this Chapter, we use a PR-LBM featuring an on-grid description of solid particles as presented in Chapter 3, to investigate and compare the accuracy provided by the standard Bounce-Back (BB) and the Equilibrium Interpolation (EI) schemes typically used to model fluid-solid interactions in the framework of the LBM.

The problem of accuracy scaling of on-grid particle description with respect to different resolutions, in the case of non-moving particles, has been addressed by several authors. For example, Chun *et al.* [108] performed a convergence analysis of the permeability for flows across different arrays of spheres and cubes, while Sanjeevi *et al.* [49] show the scaling of the drag coefficient of a fixed sphere for different resolutions.

When particle motion is taken into account, accuracy can be negatively affected by different mechanisms, such as volume fluctuations and lack of strict mass conservation, induced for example by the reconstruction the distributions at the uncovered fluid nodes, as shown in [110]. These detrimental effects can in principle lead to different convergence rates as a function of particle resolution with respect to the case of stationary particles, especially if the two-way coupling between particle and flow is relevant like in the settling of a particle in the Stokes flow regime. However, fine accuracy measurements in cases where particles are moving coupled with the flow are challenging due to the difficulties related to find an appropriate benchmark capable of taking into account finite-domain effects. Indeed, in most of the cases where an analytical expression of the motion of the particle is available, the deviations induced by the finite simulation domain are often larger than the one induced by finite-resolution effects related to particle discretization (as shown later in Fig. 4.2 in Section 4.2).

In this Chapter we firstly address the possibility to reduce the effects of a finite-size domain by focusing on cases where the flow is strongly coupled with the particle motion, namely the settling of a spherical particle in a quiescent fluid and the rotation of spherical particles in a shear flow, both under low-Reynolds number conditions (approaching Stokes flow regime). For these cases we have access to analytical expressions for the flow field in an unbounded domain.

In order to recover these flows under ideal conditions, we propose an adaptive boundary treatment at the boundaries of the simulation domain that allows to mimic the behavior of an unbounded fluid, allowing to strongly reduce non-ideal effects induced by the finite-size of the simulation domain. Accuracy scaling with varying particle resolution can then be finely evaluated for different fluid-solid treatments, namely the standard BB, and the Equilibrium-Interpolated (EI) Bounce-Back scheme proposed by Chun *et al.* [108].

We introduce an improvement of the aforementioned EI scheme that allows to detect very small particles in the framework of the standard momentum-exchange interaction scheme. This new method will be addressed as *Complete Equilibrium Interpolation* (CEI) and it will be compared with the aforementioned EI scheme in cases where the simulated particles are described by very few lattice nodes. As an addition to the investigation under Stokes flow conditions presented in this work, we show in Appendix A that for fully resolved particles EI and CEI recover the expected flow behavior also in cases where the Reynolds number is small, but finite.

The final motivation of this work is the understanding and fine measurements of the accuracy scaling of momentum-exchange methods with respect to particle resolution, with a focus on cases when their computational resolution is decreased to just a few grid points. The possibility to efficiently simulate smaller particles without a loss in accuracy when compared to standard approaches can be a valuable tool for simulations of dense suspensions, where many more particles can now be simulated without loss in accuracy and without up-scaling the simulation size to larger resolutions, greatly increasing the computational efficiency. The feature to be sensible to surface details as small as the lattice spacing can be relevant also for fully-resolved particles with complex shape or fine surface details; these details can now be captured with more precision.

4.2 Adaptive boundary conditions to simulate Stokes settling

In this Section we present the definition of an adaptive boundary treatment of the computational domain boundaries for the case of a spherical particle settling under the effects of gravity in Stokes conditions. Thanks to this novel approach we are able to strongly reduce the effects of the finite simulation domain on the dynamics of the moving particle, allowing to perform precise accuracy measurements.

In Chapter 2 we presented the general expressions, given by Eqs. (2.35)-(2.36), for the perturbations induced by a particle moving in an unbounded fluid. For the case of a spherical particle, we showed that the analytical expressions of the different perturbations in the velocity field induced by its motion are given by Eqs. (2.39)-(2.41), while for the pressure field the same perturbation are given by Eqs. (2.42)-(2.43).

We will use these results to address the problem of the settling of a spherical particle under the effect of gravity in an otherwise unperturbed fluid, so that all the external ambient fields are set to zero and the perturbations induced by the particle reduce to Eq. (2.39) and Eq. (2.42).

As already discussed in Chapter 2 (with a slightly different notation), when the particle motion is caused by an external acceleration $\boldsymbol{g}$, e.g. gravity, the final settling velocity $\boldsymbol{U}_0$ is given by the well-known relation

$$\boldsymbol{U}_0 = \frac{2(\rho_p - \rho_f)\boldsymbol{g}R^2}{9\mu}, \tag{4.1}$$

where ρ_f and ρ_p are the fluid and the particle density, respectively. In the rest if the Chapter we will address only motion along the $-z$ direction, so that $\boldsymbol{g} = (0, 0, -g)$, $\boldsymbol{U}_P = (0, 0, U_P)$ and $\boldsymbol{U}_0 = (0, 0, U_0)$.

Simulating the settling of a particle in the ideal Stokes regime (which formally requires an unbounded domain) is not possible using standard boundary conditions (e.g. no-slip or periodic) on the domain boundaries of the simulation box. In these kind of simulations of the dynamics of finite-volume particles, in fact, two main sources of errors are typically present: one is introduced by the finite size of the simulation domain, and another comes from resolution effects due to the discretization of the particle. The influence of domain boundaries on the overall accuracy of the Stokes flow description is significant, making it unfeasible to use the Stokes settling problem and the computation of the terminal settling velocity as an accuracy estimator for the numerical scheme. To overcome such limitations we propose a method to mimic unbounded fluid within a finite simulation domain by exploiting the analytical solution for the Stokes flow problem under investigation.

The dynamics of the particle and the fluid inside the computational domain are fully resolved using the PR-LBM, while we impose on the boundary nodes (see sketch in Fig. 4.1) the macroscopic velocity $\mathbf{u}$ and the pressure p according to Eqs. (2.35) and (2.36), where the instantaneous particle velocity U_P (as computed from the simulation) and its radius, R, are used to calculate the analytical values. In the LBM framework this is done by setting the equilibrium distribution $f^{(0)}$ given in Eq. (3.43) on the boundary nodes.

In this way, even if the particle velocity is affected by an error related to the particle discretization, we are able to reproduce the Stokes velocity field of a sphere moving with speed U_P, largely reducing the impact of having a finite size simulation box. An example of the improvement is shown in Fig. 4.2, where the particle velocity is plotted for different boundary conditions and sizes of the computational domain. While in the case of periodic boundary conditions the particle would indefinitely accelerate due to the interactions with its mirror images, imposing no-slip at the domain boundaries would lead to a severe under-estimate of the Stokes terminal velocity also for very large sizes of the simulation domain. As a proof of concept of the method, we apply the same approach to a more complex case, i.e. the settling of two vertically aligned identical spheres. The analytical solution for this case can

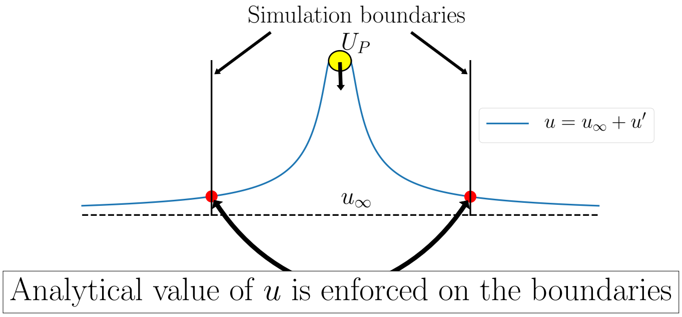

Figure 4.1: Sketch of the application of the adaptive boundary condition for the problem of a settling sphere. The analytical value of the velocity field (and of the pressure field) produced by a spherical particle settling at velocity $\boldsymbol{U_P}$ is enforced on the boundary nodes in order to emulate the properties of an unbounded fluid. At infinite distance from the particle the flow velocity is the unperturbed one, defined with u_∞.

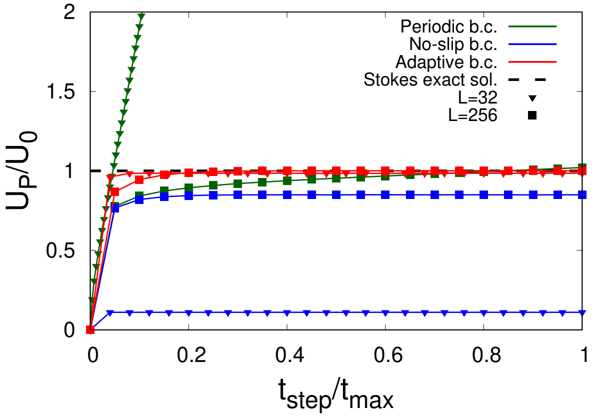

Figure 4.2: Particle velocity, $\boldsymbol{U}_P$, normalized with the Stokes velocity, U_0 defined in Eq. (4.1), is plotted for no-slip (blue), periodic (green) and adaptive (red) boundary conditions applied on the simulation box of different sizes L with respect to a fixed particle radius R. The ideal Stokes settling velocity is recovered only using an adaptive domain boundary that mimics the behavior of an unbounded fluid. Results here represented correspond to $R = 10$, $\tau = 0.85$, $\rho_p = 2\rho_f$ and $Re = 10^{-3}$.

be obtained from Lamb's general expression of the velocity perturbations generated by two moving spheres, as from [134]. While the general solution by Lamb consists of an infinite series of terms from a Spherical Harmonic expansion, for the sake of simplicity we only impose on the domain boundaries its truncation to the first order. Notwithstanding this approximation, simulations results are in fairly good agreement with the theoretical estimate of the settling velocity of the particle provided by the method of reflections [44] , computed at the first reflection, given by:

$$\frac{U_P}{U_0} = 1 + \frac{3R}{2d}, \tag{4.2}$$

where R is the radius of the spheres and d is the distance between their centers. Results as shown in Fig. 4.3.

4.2.1 Accuracy as a function of the simulation box size at fixed resolution

The adaptive boundary conditions, proposed in the previous paragraph, are now applied to measure the performance of the BB and the EI fluid-solid interaction schemes

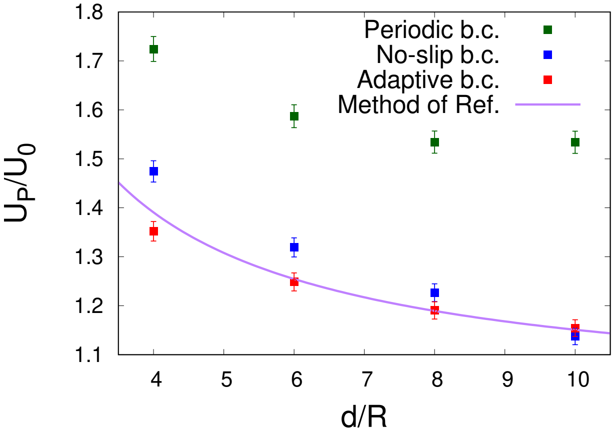

Figure 4.3: Terminal velocity U_P, averaged over the last 100 timesteps, of two vertically aligned spheres settling under gravity as a function of the distance between the centers of the spheres d over their radius R. The simulation domain size is fixed to $L = 180$, while $\tau = 0.6$ and $\rho_p = 2\rho_f$. Results using the adaptive treatment on the simulation domain boundaries (red squares) are compared with the ones obtained using periodic (green squares) and no-slip (blue squares) conditions. For the adaptive case, the general solution from Lamb, truncated to the first term, is applied on the domain boundaries to simulate Stokes settling of two vertically aligned spheres. Results are in fairly good agreement with the predictions from the method of reflections, computed at first reflection, from Eq. (4.2) (purple solid line), except at the smallest value of d/R where the truncation to the first order shows its limitations. The error bars represent a confidence interval of our measurements and are obtained from the velocity difference, converted in relative units, between the adaptive case and in the no-slip case at $d/R = 10$, for which we expect maximum accuracy.

in reproducing the dynamics of the settling of a spherical particle in Stokes flow conditions.

In this first analysis we evaluate the impact of different simulation box sizes L on the accuracy of the particle terminal velocity, computed as the percentage deviation from the Stokes settling velocity given by Eq. (4.1). Simulations are performed with particle radius $R = 10$, Reynolds number $Re = 10^{-3}$ and a value of $\tau = 0.6$ is chosen in order to reduce as much as possible the onset of numerical slip effects. The Kn number given by Eq. (3.48) is now calculated using the particle radius as characteristic length scale. In this way $Kn \sim 0.07$ for $R = 1$ and $Kn = 0.007$ for $R = 10$. The density of the particle is set to $\rho_p = 2\rho_f$ and the gravity acceleration along the z direction, $-g$, applied on the particle follows from the choice of $Re = U_0 R/\nu$ and using Eq. (4.1) . The time-averaged settling velocity $\langle U_P \rangle$ is computed after the initial transient required to reach the terminal velocity has decayed, and then compared with the Stokes value from Eq. (4.1).

While the distance between the simulation boundaries and the particle is still playing a relevant role on particle dynamics, we are now able to isolate the accuracy loss induced by finite-resolution effects due to particle discretization from domain size effects. These results are highlighted in Fig. 4.4, where we plot the relative error of the average of the particle terminal velocity for different simulation domain sizes L. We observe that the accuracy on the particle velocity converges to a non-zero value that we interpret as the maximum precision achievable for a given particle resolution and for a virtually unlimited simulation domain size, for which all the non-ideal effects induced by the finite size of the simulation domain will be vanished and only the resolution error will remain. In order to exclude, as much as possible, boundary effects on the accuracy estimation, we extract the convergence value through a power-law fit of the form

$$f(L) = \left(\frac{1}{L}\right)^{\alpha} + \varepsilon, \tag{4.3}$$

where α and ε are free fit parameters.

The accuracy loss induced by the presence of the simulation boundaries for large

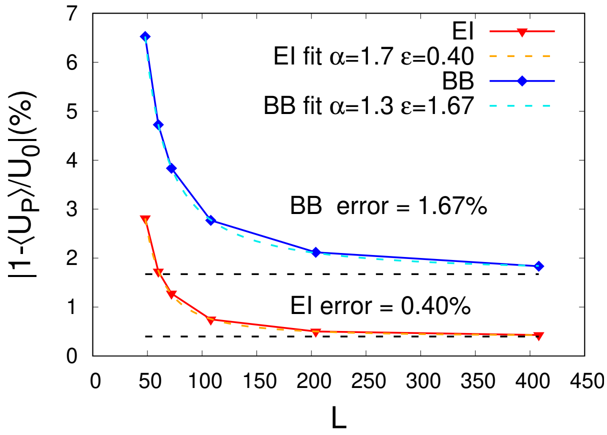

Figure 4.4: Accuracy of the particle terminal velocity using EI (red triangles) and BB (blue diamonds) boundary conditions for $R = 10$, $\tau = 0.6$ and $Re = 10^{-3}$ obtained varying the simulation domain size L from 48 to 408. Fit functions obtained using Eq. (4.3) (colored dashed lines) show a convergence of the error to a limit value (black dashed lines) represented by the fit parameter ε. This limit value represents the maximum accuracy achievable for a given particle resolution.

confinement ratios $2R/L$ can be understood by recalling the general theory of multipoles expansion (e.g. Chapter 3 in [44]) for the velocity field generated by an arbitrary shaped particle. Firstly, since the simulated particle is not an ideal sphere due to finite-resolution effects related to the modeling of the particle surface within the LBM, the perturbation induced on the flow will deviate from the one of an ideal sphere. Secondly, an additional source of error is given by the model used to describe moving boundary effects embodied in Eqs. (3.54) and (3.55), where the velocity profile between particle surface and the first adjacent fluid node is assumed linear, which we know from Eq. (2.39) is not the case for the problem under examination.

As a result of these two error sources, deviations from Stokes analytical solution are expected in the vicinity of the particle, as shown in Fig. 4.5, where the relative error of the flow is computed for every fluid node as:

$$e_u = \sqrt{\frac{|u_{an}(U_P) - u_{sim}|^2}{u_{an}^2(U_P)}}, \tag{4.4}$$

where the analytical velocity field $u_{an}(U_P)$ is calculated from Eqs. (2.35) and (2.39) using the instantaneous velocity U_P of the particle.

If the boundaries of the simulation domain are too close to the particle, the higher order terms in the flow field generated by non-ideal effects related to particle discretization will not vanish and the match with the analytical solution for a settling sphere forced on the domain boundaries will not be perfect, negatively affecting the simulation accuracy.

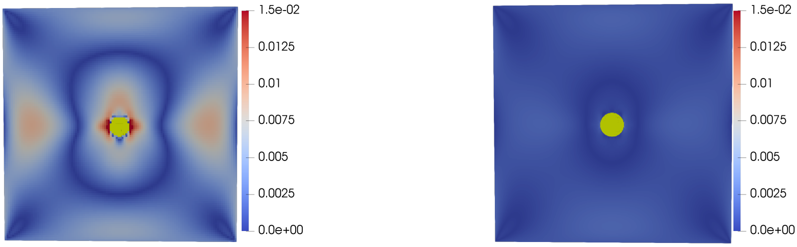

Figure 4.5: Relative error in the flow as defined in Eq. (4.4), $e_u = \sqrt{|u_{an}(U_P) - u_{sim}|^2/u_{an}^2(U_P)}$, for a less resolved (left) and better resolved (right) particle with respectively $R = 5$ and $R = 20$ at the same confinement ratio $2R/L$. The analytical velocity field $u_{an}(U_P)$ is computed using Eqs. (2.35) and (2.39). Discretization effects induce higher deviation from the ideal Stokes flow field around the particle that strongly depend on particle resolution.

4.2.2 Convergence analysis and velocity fluctuations

In the previous paragraph we showed how to measure the asymptotic error for a particle at fixed radius. The same analysis shown in Fig. 4.4 is now repeated for different values of R in order to obtain the accuracy convergence rate with respect to particle resolution. For each investigated value of R we performed different simulations varying the domain size L in order to fit the measured error with Eq. (4.3) to obtain the asymptotic error.

In addition to the average deviation of the particle velocity from the Stokes solution, velocity fluctuations around the mean velocity represent another important observable to assess particle dynamics accuracy. While the particle moves across the lattice grid, its total volume varies accordingly to the lattice nodes that are covered (and un-covered) by the particle during its motion. These volume fluctuations are reflected in the particle dynamics by unphysical jumps in the velocity profile, as shown in Fig. 4.6, where the time evolution of the velocity of the particle is plotted. We compute the average velocity fluctuations as:

$$\langle \Delta U_P \rangle = \frac{\sum_t (U_{P,t} - \langle U_P \rangle)^2}{T}, \tag{4.5}$$

where t represents a measure at a given timestep and T the total number of timesteps, both taken excluding the initial transient.

Results obtained from the convergence analysis of the two investigated models (BB and EI) are compared in Fig. 4.7, where the measured asymptotic error and the average velocity fluctuations are plotted against the particle radius. All the simulations have been performed by keeping $\tau = 0.6$, $\rho_p = 2\rho_f$, $Re = 10^{-3}$. After a best fitting of the data we obtain an empirical relation for the asymptotic error given by:

$$\varepsilon_{BB}(R) = 13.7 \cdot R^{-0.89}, \tag{4.6}$$

$$\varepsilon_{EI}(R) = 13.7 \cdot R^{-1.51}. \tag{4.7}$$

While for the EI scheme the measured convergence rate is in fair agreement with the one observed for fixed particles in [108], for the BB case the second-order scaling shown in [108] is lost and now it exhibits a clear first-order scaling. The main difference between our case and the reference one is the motion of the particle: EI is able to continuously detect the boundaries location while the position of the particle is updated, while BB can detect an update in the boundary locations only after a displacement of the particle of the order of the lattice spacing, resulting in a first-order accurate description of the boundary motion. Velocity fluctuations are second-order convergent for both investigated cases.

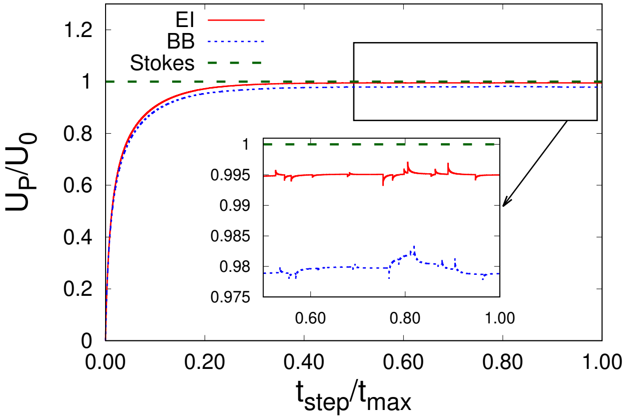

Figure 4.6: Velocity U_P of a settling particle with $R = 10$, normalized with respect to the Stokes settling velocity U_0 using the EI (red solid line) and the BB (blue dashed line) schemes, as function of time. Other relevant parameters are $L = 200$, $\tau = 0.6$, $\rho_p = 2\rho_f$. In the inset a zoom on the y axis of the selected region is performed to show the fluctuations in the velocity profile due to the volume variation of the particle during its motion.

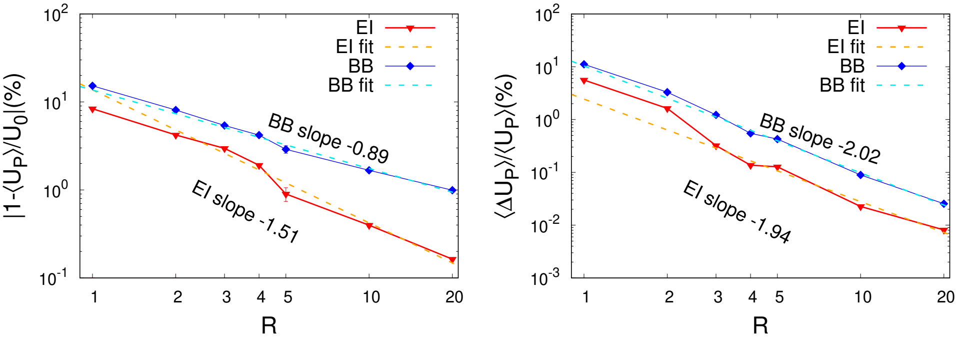

Figure 4.7: Asymptotic error (left) of the average velocity $\langle U_P\rangle/U_0$ and average velocity fluctuations $\langle \Delta U_P\rangle/\langle U_P\rangle$ as computed from Eq. (4.5) (right), with respect to particle radius R. Convergence rates are obtained through a power law fit (colored dashed lines) of the measured asymptotic error and reported as the slope of the best fit in the semilog plot. EI strongly reduces errors, keeping an accuracy scaling comparable with the one observed in [108]. Using BB, the accuracy scaling is instead only first-order. Second-order convergence is maintained in both cases for the velocity fluctuations.

There are other concurring mechanisms that have a detrimental effect on the accuracy of particle dynamics: at first, lattice parameters such as the relaxation time τ are known to influence the LBM accuracy in recovering the hydrodynamics of the flow [135], so that a different choice of τ can lead to a different accuracy scaling. Another relevant error source is the already discussed model for the interaction between the flow and a moving boundary embodied in Eqs. (3.54)-(3.55), which introduces a first-order error in the flow velocity around the particle.

4.2.3 Complete Interpolation: sub-grid particle simulations and accuracy

In the standard momentum exchange approach, the link-nodes (i.e. fluid nodes from which at least one lattice velocity component $\mathbf{e}_a$ points inside the solid volume) are evaluated only between fluid and solid nodes, neglecting the possibility to detect the surface of the particle when it is located between two fluid nodes. While, in general, this feature is not particularly important for fully-resolved spherical particles, it can introduce an important effect for particles with complex shapes or with fine surface details. In this section, we propose an improvement of the EI scheme in which the capability to detect the surface of the particle also in between two fluid nodes is implemented using a standard ray-sphere intersection algorithm [118] as shown in Fig. 4.8. This novel boundary treatment will be addressed as Complete Equilibrium Interpolation (CEI).

One example of the capability to resolve sub-grid particle dynamics offered by CEI is shown in Fig. 4.9 where the settling of a particle with radius $R = 0.6$ initialized in the center of the simulation domain is compared with the EI scheme for two different lattice models, namely the D3Q19 and D3Q27 lattice stencils. An increased number of velocities, provided by a larger lattice, can increase accuracy of CEI in detecting the surface of the particle. This effect can be observed in the top plot of Fig. 4.9, where the number of links is plotted as a function of time. It is to be noted, however, that on-grid particle description only allows to use single-cells lattice stencils, so that the D3Q27 is already the upper limit.

The achievable accuracy for small radii, i.e. when $R \leq 2$, using a CEI scheme is now investigated and compared with the standard EI and BB models for a D3Q19 lattice stencil. The simulations are performed by keeping the confinement ratio $2R/L = 0.05$ between particle radius R and the size L of the computational box, which is enough to keep the effects from the boundaries of the simulation box negligible when compared to the ones from the particle resolution for such small radii. The relaxation time is again set to $\tau = 0.6$, while the density of the solid particle is increased to $\rho_p = 3\rho_f$ to increase numerical stability against the stronger fluctuations observed in the simulation due to the extreme values of R.

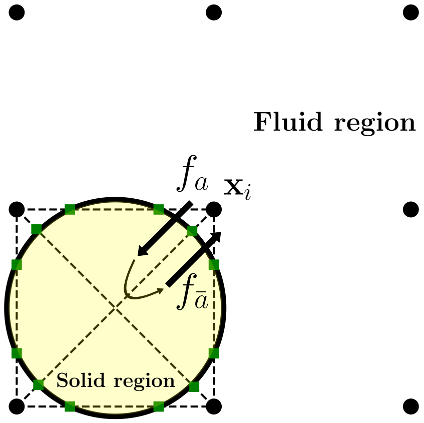

Figure 4.8: Sketch of a particle with a resolution comparable to the grid spacing ($R = 0.55$). In such cases there might be no lattice nodes enclosed by the solid volume and both BB and EI schemes fail to detect the particle. Using Complete Equilibrium Interpolation (CEI) it is now possible to detect the particle position and surface (green squares) also between adjacent fluid node links.

For such small particles the discrete effects introduced by the simulation grid can play an important role on the dynamics, so we addressed the problem by performing an ensemble of 10 identical simulations with different initialization of the particle center, that now is randomly located in the range of ± 0.5 with respect to the simulation domain center, as sketched in Fig. 4.10. In this way the particle discretization on the lattice grid will be different for every different location of the particle center, allowing us to observe the impact of the lattice on the overall accuracy.

Results are shown in Fig. 4.11, where the final accuracy and velocity fluctuations, averaged over the ensemble, are plotted against the particle radius, R. In addition, minimum and maximum values, observed in the ensemble, are reported as error bars in order to give a quantitative idea of the fluctuations that can occur for such small particles using an on-grid description.

It is remarkable that using the CEI scheme it is possible to keep the average error on particle speed below 10% for sub-grid particles, while strongly suppressing velocity fluctuations of more than one order of magnitude in these cases. The performance scaling of the momentum exchange routine with respect to particle resolution has been investigated in Fig. 4.12. It is found that the overhead introduced by CEI, noticeable only for large radii, is small if compared with the increase in accuracy provided by the CEI scheme. From Fig. 4.11 it can be noted, in fact, that for the case of a particle

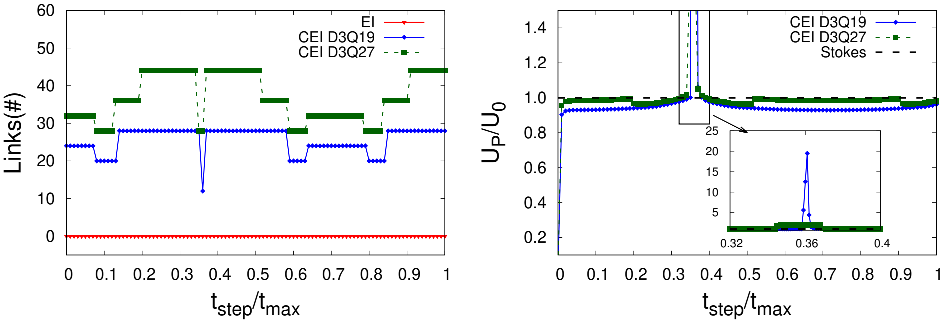

Figure 4.9: Number of link-nodes for momentum exchange (left) and time evolution of particle velocity (right); EI (red triangles), CEI using D3Q19 lattice (blue diamonds) and CEI using D3Q27 lattice (green squares) for a particle with radius $R = 0.6$. Standard EI is not able to capture a sub-grid particle when initialized in the domain center (zero occupation on top plot), leading to a free fall velocity profile (and thus omitted from the bottom plot for the sake of readability). Using CEI, the particle is correctly detected, but some peaks appear in the velocity profile due to the drop in the number of link-nodes during the motion of the particle when a D3Q19 lattice is used. This effect can be mitigated by using the higher order lattice such D3Q27.

with $R = 1$ the accuracy obtainable with the CEI scheme is higher than the one achievable with the BB scheme using $R = 2$, while the computational overhead is barely noticeable. Moreover, if the same reduction in resolution is applied also to the domain size, like in convergence studies, a shrinking of a factor of 2 in the overall resolution can lead to an improvement in the performances up to a factor of 8 in terms of simulation time.

4.3 Rotational dynamics of a spheroidal particle in a shear flow

In this Section we investigate the dynamics of spheroidal particles set into rotation by a shear flow. In the first part of the analysis we show an application of the adaptive boundary conditions to the case of spherical and ellipsoidal particles free to rotate in an ambient shear flow, while in the last part we study the accuracy of the CEI scheme in resolving the rotational dynamics of an ellipsoidal particle. The relaxation time is again set to $\tau = 0.6$ for all the simulations in this Section. The fundamental theory behind rotation of ellipsoidal particles in shear flows was developed by Jeffery [47]

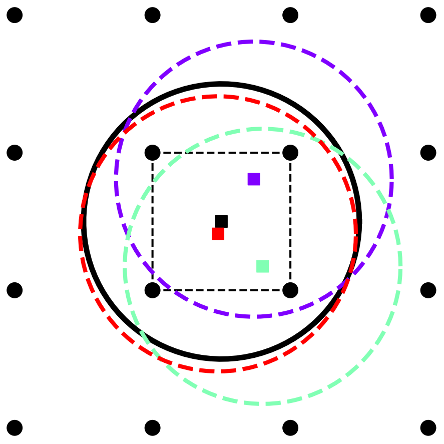

Figure 4.10: Sketch of particles with $R = 1$ initialized with random offsets of ± 0.5 with respect to a particle (black solid line) located at the center of the simulation domain (black square). The colored squares represent the center of each different particle (dashed colored lines). Different initializations lead to different discretizations of the particles on the lattice grid, represented by the number of lattice nodes connected by the black dashed lines that are enclosed by the surface of the particles.

and has been discussed in Chapter 2. There, we show that the angular velocity, $\omega(t)$, of a general spheroidal particle set into motion by an unbounded shear flow is:

$$\omega(t) = \frac{C}{a^2 + b^2} \left(a^2 \cos^2 \theta(t) + b^2 \sin^2 \theta(t)\right), \tag{4.8}$$

$$\tan \theta(t) = \frac{a}{b} \tan \left[\frac{Cabt}{a^2 + b^2}\right], \tag{4.9}$$

where a and b are the major and minor axes of the ellipsoid in the plane of the shear respectively, $C = 2U_{shear}/L$ is the shear rate at a given simulation domain size L, assuming that the shear flow is driven by two moving walls at $\pm U_{shear}$. The variable $\theta(t)$ describes the angle between the major axis and one of the main directions in the shear plane.

The angular velocity $\omega(t)$ of the ellipsoid is then described by a family of curves that depend on the shear rate and on the starting orientation of the particle and in general it will show periodic oscillations with period

$$T_{jef} = \frac{\pi(a^2 + b^2)}{abC}. \tag{4.10}$$

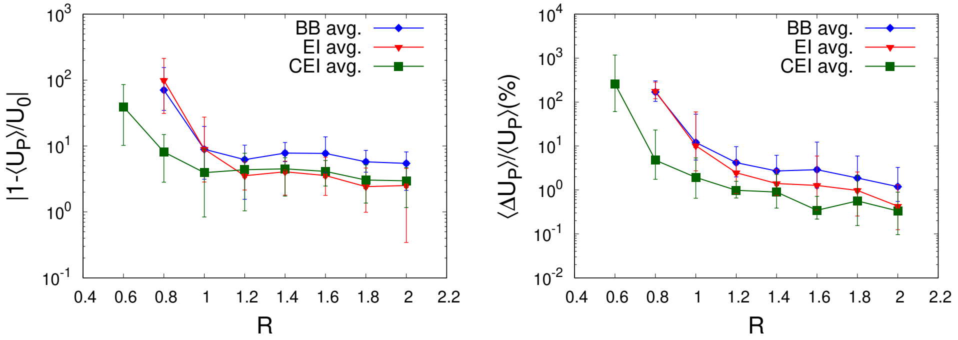

Figure 4.11: Averages (solid lines) of the accuracy on particle velocity (left) and of the velocity fluctuations (right) for $0.6 \leq R \leq 2$. Results are averaged over an ensemble of 10 simulations having different random initialization of the particle center within ± 0.5 from the domain center. Minimum and maximum values within the ensemble are represented by the error bars. The CEI scheme (green squares) allows to describe the dynamics of particles with small radii at increased accuracy with respect to EI (red triangles) and BB (blue diamonds) schemes, while strongly reducing velocity fluctuations. With the CEI scheme is now possible to detect solid features on the order of one lattice grid spacing.

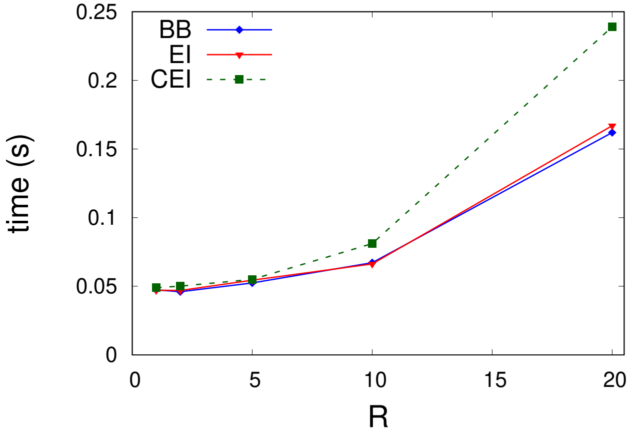

Figure 4.12: Time required to perform one call of the momentum exchange routine, averaged over 1000 timesteps, for BB (blue diamonds), EI (red triangles) and CEI (green squares) as a function of the particle radius, R. For small values of R the performances of the three investigated algorithm are similar, while for larger values of R CEI introduces some overhead, that can be reduced with a higher level of code optimization.

Some particular cases are shown in Chapter 2 (see Fig. 2.4), where the analytical trajectory of the angular velocity is plotted for a sphere and for an ellipsoid with different internal aspect ratios.

The adaptive boundary conditions presented in the previous Section, i.e. the possibility to enforce on the boundaries of the simulation box the analytical expression of the perturbation induced by the presence of the particle, can be straightforwardly applied for the case of a spherical particle free to rotate in a shear flow. An unperturbed shear flow can be modeled as the sum of two equal contributions from an ambient vorticity, $\boldsymbol{\Omega}^{\infty}$, and an ambient strain, $\mathbf{E}^{\infty}$. The velocity field of a shear flow having a velocity of $\pm U_{shear}$ along the $\hat{x}$ direction at $y = \pm L/2$ respectively can then be obtained from Eq. (2.35) by imposing the ambient fields as:

$$\boldsymbol{\Omega}^{\infty} = \left(0, 0, -\frac{C}{2}\right), \tag{4.11}$$

$$\mathbf{E}^{\infty} = \begin{pmatrix} 0 & \frac{C}{2} & 0 \\ \frac{C}{2} & 0 & 0 \\ 0 & 0 & 0 \end{pmatrix}. \tag{4.12}$$

In this configuration, the rotational dynamics of the particle is limited to the shear plane and the angular velocity of the particle can be written as $\boldsymbol{\omega}_P = (0, 0, \omega_P)$. For this reason, from now on we will refer only to the non-zero component ω_P and the vector notation will be omitted.

As we did for the settling problem, the particle and flow dynamics are fully solved by the PR-LBM and the instantaneous value of the particle angular velocity, ω_P, is used to impose the analytical flow using Eq. (2.35) on the boundaries of the simulation domain. In this way we are able to suppress any boundary effects due to the finite size of the simulation domain also for extreme cases, as shown in Fig. 4.13, where we plot the angular velocity of a spherical particle with $R = 10$ initialized in the center of a domain with size $L = 24$ (which means that the confinement ratio $2R/L \sim 1$). We compare the results using our adaptive method and the standard approach (i.e. when the shear flow is driven by walls moving at $\pm U_{shear}$ and periodic boundary conditions are applied along the direction of the flow). The exact angular frequency for the particle, as predicted by Eq. (4.8), is obtained for any values of the particle radius and domain size, so that a resolution analysis for the spherical particle case is omitted.

While in principle Eqs. (2.40-2.43) are exact only for a spherical particle, the adaptive boundary treatment can be efficiently used to reduce boundary effects also for the case of a non perfectly spherical particle. We focus on the case of an ellipsoid with internal aspect ratio $a/b = a/c = 2$ and major radius $a = 10$, rotating in a shear flow with

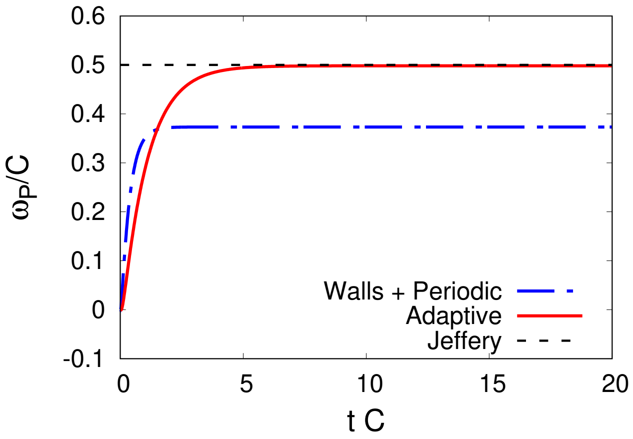

Figure 4.13: Angular velocity for a sphere of radius $R = 10$, rotating in a shear flow with shear rate $C = 0.002$. The simulation domain size is set to $L = 24$, so that the domain boundaries of the simulation box are almost in contact with the particle. Using the adaptive boundary conditions (red solid line) we are able to suppress detrimental boundary effects and the analytical angular frequency (black dashed line) is exactly reproduced. Using a standard approach (blue point-solid line) consisting of no-slip moving walls in the orthogonal direction to the flow and periodic boundaries along the flow the detrimental effects due to the vicinity of walls on Jeffery's ideal dynamics is evident.

analogous geometry as the one used for Fig. 4.13. The shear rate C is set in such a way that $U_{shear} = 0.01$ is fixed for all the simulations. In this context we apply the adaptive treatment on the boundaries using Eqs. (2.40-2.43), but this time we use an effective radius for the perturbations given by $R_{eff} = \sqrt[3]{abc}$. This is equivalent to approximate, on the simulation boundaries, the perturbation generated by the rotating ellipsoid with the ones generated by a sphere with the same volume. We compare the performance in recovering the analytical period from Eq. (4.10) using our adaptive approach and the standard approach, for different confinement ratios $2a/L$, and the results are shown in Fig. 4.14. In order to perform this measurements we fit our data with a modified set of Eqs. (4.8-4.9), which are now able to capture period variations and to take into account the presence of an initial transient. These equations read:

$$\omega_{fit}(t) = \frac{C}{a^2+b^2}\left(a^2\cos^2\theta_{fit}(t) + b^2\sin^2\theta_{fit}(t)\right), \tag{4.13}$$

$$\tan\theta_{fit}(t) = \frac{a}{b}\tan\left[\frac{Cabt}{a^2+b^2}s + \phi\right], \tag{4.14}$$

where s and ϕ are free fit parameters that represent a period stretching and a phase shift due to an initial transient, respectively.

While it is commonly found in the literature [136, 137] that in this setup boundaries effects induced by triggering the shear flow using moving walls can be considered negligible for a confinement ratio $2a/L \leq 0.1$, we observe that we can largely reduce their impact using our novel adaptive approach for all the investigated confinement ratios.

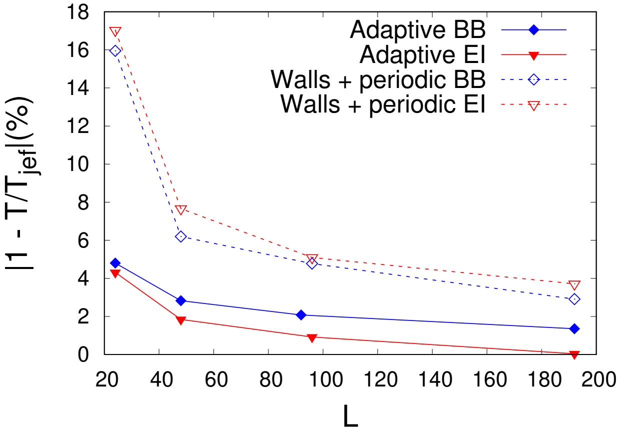

Figure 4.14: Relative error on the analytical period, given by Eq. (4.10) and measured by fitting our data with Eqs. (4.13) and (4.14), of the oscillations of the angular frequency for an ellipsoid with aspect ratio $a/b = a/c = 2$, at fixed major radius $a = 10$ for different values of the simulation domain size L. We compare the results using the BB (blue diamonds) and EI (red triangles) schemes for two different treatments of the simulation domain boundaries. The influence on the dynamics of the particle of the simulation boundaries is strongly reduced using our novel adaptive treatment. Results for $\tau = 0.6$, $U_{shear} = 0.01$.

We now aim to test and compare the CEI scheme capabilities to model particles with more complex shapes. This is done by comparing the performances of different boundary treatments of the surface of the particle in reproducing the dynamics of an ellipsoid rotating in a shear flow. To simulate this setting we again use the adaptive treatment by enforcing on the simulation boundaries Eqs. (2.40-2.43), where the perturbation terms are approximated by the ones produced by a sphere rotating at ω_P with the effective radius $R_{eff} = \sqrt[3]{abc}$, in an analogous way as we did for Fig. 4.14. The shear rate C is again set to reproduce the shear flow produced by two walls moving at $\pm U_{shear}$, with $U_{shear} = 0.01$.

Simulations have been performed for an ellipsoid with internal aspect ratio $a/b = a/c = 2$, while varying the radii of the particle and the simulation domain size L in

order to keep the confinement ratio constant at $2a/L = 0.1$.
An example of the improvement introduced by interpolation based algorithms is shown in Fig. 4.15, where the angular velocities of a low resolution particle are compared for different boundary treatments. The EI scheme already leads to a remarkable improvement with respect to the BB scheme, but now using the more sophisticated CEI scheme the ellipsoid poles are better resolved during the dynamics, leading to a more defined trajectory. The algorithm capabilities to capture particle dynamics for

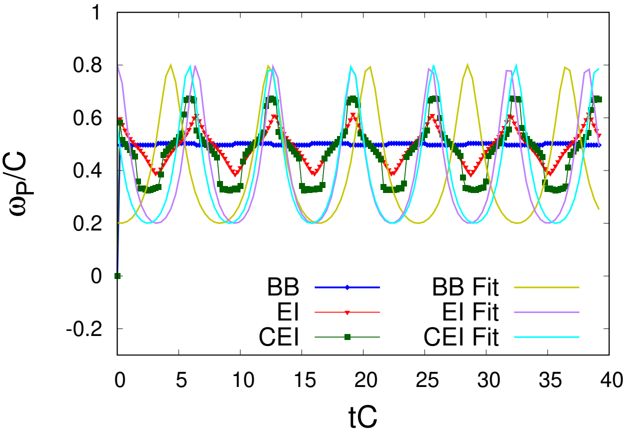

Figure 4.15: Angular frequency evaluated from Eq. (4.8) using BB (blue diamonds), EI (red triangles) and CEI (green squares) schemes for an ellipsoidal particle with major radius $a = 1.5$ and minor radii $b = c = 0.75$ at $\tau = 0.6$ and $L = 30$. The particle center is initialized at the point $(15, 15, 15)$. For the BB case the algorithm is not able to distinguish the ellipsoid from a spherical particle, while the EI and CEI schemes are increasingly better in capturing shape features. The best fits, obtained using Eqs. (4.13-4.14), are used to evaluated the accuracy of every method in reproducing the ideal rotational dynamics.

a progressively less resolved ellipsoid can now be addressed. We investigate how the error scales with the resolution of the particle by varying a from 1 to 5. As we did for the case of the settling of a spherical particle, we address the problem of the impact of grid resolution on the simulation accuracy by repeating 10 identical simulations for different random initialization of the particle center within a range of ± 0.5 with respect to the simulation domain center.

The error on the period is once again measured using Eqs. (4.13) and (4.14). It is to be noted, however, that the error on the period is not the best indicator to finely address the accuracy of the dynamics of a low resolution particle, since the fit model embodied by Eqs. (4.13) and (4.14) can often extract an accurate angular trajectory also from not so accurate signals, as shown for the BB case in Fig. 4.15. For this reason here we consider also the average error on the angular trajectory between the simulation data, ω_P, and the fit function ω_{fit} obtained from Eq. (4.13). In this way we are able to provide a more reliable indicator of the instant-by-instant precision in the reconstruction of the rotational dynamics of the ellipsoid under examination. Results are shown in Fig. 4.16, where the error on the period and the average error on the angular trajectory, as well as their maximum and minimum values, are plotted for the BB, EI and CEI schemes and different values of particle resolution. Improvements introduced by interpolation schemes are evident, with the maximum accuracy obtained through CEI, that allows now to capture particles radii small as half of the grid spacing. It is interesting to note, by comparing Fig. 4.16 with Fig. 4.11, that the improvements introduced by the CEI scheme are slightly more evident when an ellipsoidal particle is used, showing that CEI is more effective for particles with a complex shape.

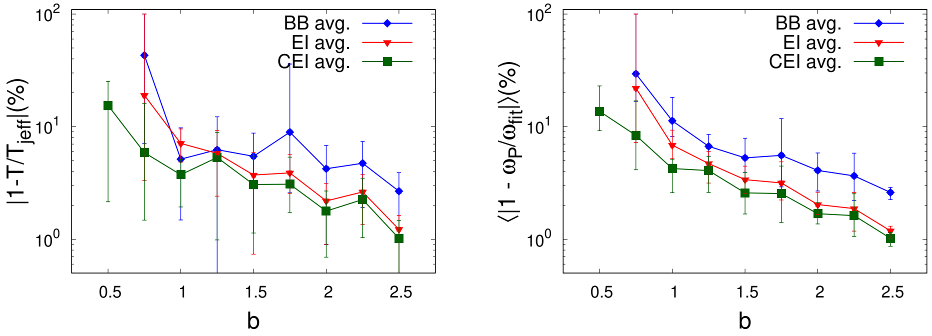

Figure 4.16: Error on the period (left) and error on the trajectory of the angular frequency (right) of an ellipsoid rotating in a shear flow. The ellipsoid has internal aspect ratio $a/b = a/c = 2$, where a is the major axis and $b = c$ are the minor axes. The resolution of the ellipsoid ranges between $0.5 \leq b \leq 2.5$. Results are averaged over an ensemble of 10 simulations, each with a different offset of the position of the particle from the domain center. The confinement ratio between particle major axis and simulation domain is kept constant, with $2a/L = 0.1$. While EI (red triangles) provides better accuracy with respect to BB (blue diamonds), both methods fail in detecting a particle with $a = 1$ and $b = 0.5$, where CEI (green squares) succeeds. The latter leads to a general improved accuracy with respect to EI. The error bars represent the minimum and maximum value in the ensemble

4.4 Concluding remarks

We propose an accurate and efficient method, based on an adaptive boundary treatment, to strongly suppress boundary effects due to the finite size of the simulation domain on the dynamics of spherical and ellipsoidal particles free to move in an unbounded fluid under Stokes flow conditions. This is done by enforcing the ideal Stokes flow solution on the simulation domain boundaries for an unbounded domain, accordingly to the instantaneous particle velocity as solved by the Lattice-Boltzmann simulation. In a sense, our approach allows to impose the correct boundary condition at infinity, but at a finite distance instead.

We firstly show that through this novel treatment of the boundaries of the simulation domain we are able to reproduce the ideal Stokes dynamics in two cases of interest, i.e. the settling of a spherical particle under gravity and the rotation of a spherical and ellipsoidal particle in a shear flow, with a higher precision with respect to the standard approaches.

We then isolate the influence of particle resolution by performing fine measurements of the accuracy convergence of the particle dynamics in the aforementioned problems, down to very low resolutions. It is the first time, up to our knowledge, that an accurate evaluation of the accuracy of the particle is carried down to such low resolutions in cases where the particle is free to move across the lattice grid.

Particle translational accuracy is firstly measured for two widely used fluid-solid interaction models, namely Bounce-Back (BB) and Equilibrium Interpolation (EI), showing that the latter strongly improves accuracy while reducing velocity fluctuations. Under the investigated case, measured convergence rate for the EI scheme is in fair agreement with what is found in the literature for a fixed obstacle, while the BB scheme only exhibits a first order convergence due to the lower accuracy in capturing the dynamics of moving boundaries.

Finally we propose a third model as an extension of EI called Complete Equilibrium Interpolation (CEI), that allows to detect momentum exchange also between two fluid nodes, in the case in which the particle surface is occupying a position between the two. We show that CEI is not only able to detect particles as small as one lattice grid spacing, where the BB and EI schemes fail, but also to provide an higher accuracy in cases where the particle size is only a few lattice nodes, while strongly suppressing velocity fluctuations due to particle volume change during time evolution.

We find that these improvements are more evident for elongated particles such as ellipsoids, making this new model promising for the modeling of particles with complex shapes (i.e. needles) or with small features at their surface. Another relevant application of this method is the simulation of dense suspensions of particles, since it allows to increase the number of simulated particles without a large accuracy loss, potentially increasing computational efficiency.

We finally show that Complete Equilibrium Interpolation is capable to recover correct flow results when inertial effects are relevant for the dynamics of the particle (Appendix A).

As last note, the adaptive domain boundary treatment presented in this Chapter can find relevant applications as an improvement to the standard periodic boundaries in all the cases where a spherical or quasi-spherical particle or bubble is moving in an ambient flow under Stokes conditions, such as in jetting problems or transport of droplets in aerosols, and it can be further extended to address more complex shapes and number of particles.

4.5 Appendix A: recovering effects of inertia at finite Reynolds numbers

In this appendix we investigate the capability of CEI and EI to recover the correct results in cases where inertia is relevant on the dynamics of the particle, focusing firstly on the problem of a cylindrical particle settling in a vertical channel at $Re = 1.03$ and $Re = 8.33$, and later on the problem of a cylindrical particle rotating in a shear flow at $Re = 79.6$. The 2D nature of this class of problems and the presence of finite Reynolds numbers are the reasons why this investigation is addressed as an appendix, since in the manuscript we focus on 3D flows in the Stokes regime.

In the absence of inertia, a particle released away from the center of a vertical channel would settle straight down with no lateral motion [134]. This is no longer the case when inertia becomes important, as particle migrates horizontally until the final equilibrium position is reached at the center of the channel. This class of phenomena has been extensively investigated by a number of authors through different numerical schemes such as the finite-element method [138–140] and the LBM [141–143]. In the first part of this appendix we investigate the performances of EI and CEI with respect to BB to recover the expected dynamics under the same flow conditions as Li *et al.* [141] (the simulation setup is sketched in Fig. 4.17-(a)).

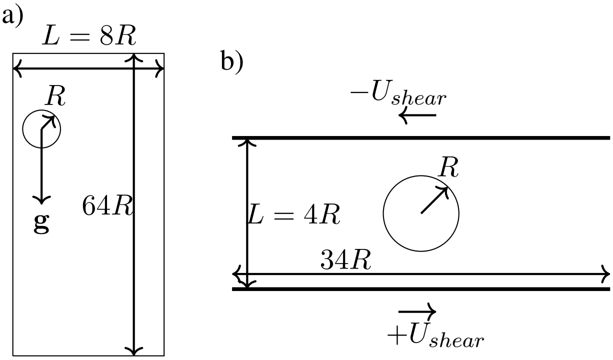

Figure 4.17: Schematic representation of: (a) a cylindrical particle of radius R released near one wall of a two dimensional channel set into motion by a gravity force $\mathbf{g}$, (b) a cylindrical particle free to rotate in a shear flow.

The channel width (along the $\hat{x}$ direction) is set to $L = 8R$, where R is the particle radius; the particle is released at an horizontal position of $x = 0.19L$ and it is free to settle under the effect of a body force $\mathbf{g} = (0, 0, g)$. The relaxation time and the particle density are set to $\tau = 0.6$ and $\rho_p = 2\rho_f$, respectively. The body force $\mathbf{g}$ is tuned to match with the desired Reynolds numbers of $Re = 1.03$ and $Re = 8.33$, where $Re = U_P 2R/\nu$ and U_P is the final settling velocity of the particle. We apply uniform zero velocities at the inlet and zero normal derivative of the velocity at outlet. Using a fully resolved particle with $R = 12$ the results from [141] are recovered with very high accuracy as shown in Fig. 4.18.

From the same plot (Fig. 4.18) it can be also observed that using EI and CEI the particle tends to respond slightly slower in the transient when compared with the BB results. This effect can be related to the increased accuracy at which EI and CEI can capture inertial effects with respect to BB and the Stress-Integration Method proposed in [141]. These differences are, in any case, very small.

Furthermore, we investigate the accuracy in recovering the final horizontal position for different resolutions of the system as a function of the particle radius R at fixed Reynolds number $Re = 1.03$. It is found that the correct horizontal position of the particle is recovered with very high precision for all the investigated combinations of resolution and boundary schemes. Interpolation-based schemes only provide a small improvement in the velocity fluctuations of the final settling velocity for small radii as shown in Fig. 4.19.

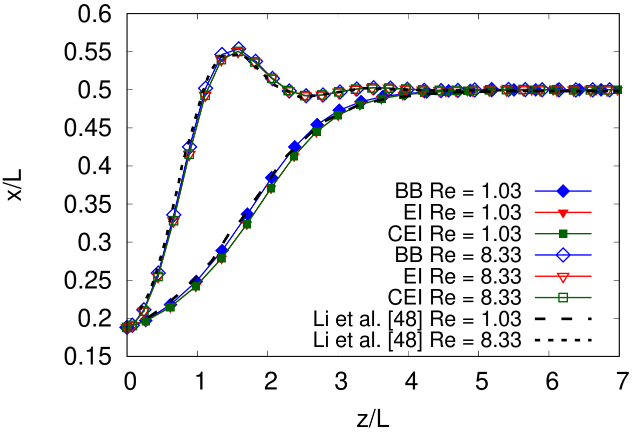

Figure 4.18: Settling trajectory of a cylinder released at $x = 0.19L$ of a vertical channel at $Re = 1.03$ and $Re = 8.33$. The particle radius is $R = 12$, while the channel width $L = 8R$. The horizontal migration towards the center of the channel is an effect related to the inertia of the particle. The dynamics observed by Li *et al.* [141] (black dashed lines) is correctly reproduced with all the investigated boundary schemes (colored point lines). Other relevant simulation parameters are $\tau = 0.6$ and $\rho_p = 2\rho_f$.

In the last part of this Appendix we show that EI and CEI are able to reproduce the correct flow dynamics of a cylinder freely suspended and free to rotate in a shear flow. Following the simulation setup presented by Ding and Aidun [145], and sketched in

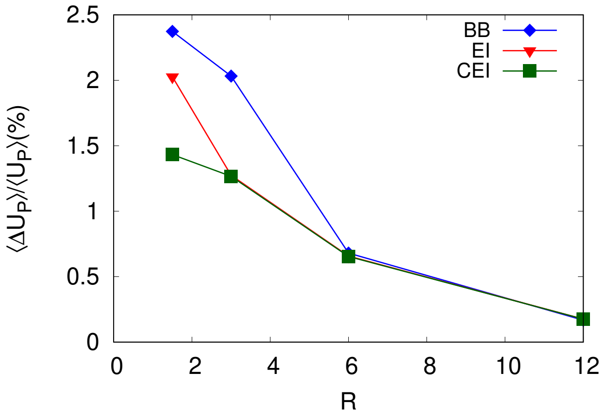

Figure 4.19: Average velocity fluctuations $\langle \Delta U_P \rangle$ (as defined in Eq. (4.5)) of the terminal velocity U_P of a cilynder settling in a vertical channel as a function of its radius R for BB (blue diamonds), EI (red triangles) and CEI (green squares). The particle is released at $x = 0.19L$ of a channel with width $L = 8R$ at $Re = 1.03$. EI and CEI slightly reduce the velocity fluctuations related to the volume fluctuations of the particle, but the effect is noticeable only for small values of R.

Fig. 4.17-(b), the radius of the particle is initially set to $R = 64$ and it is initialized in the center of a channel with a size of $34R \times 4R$, so that the channel width along the $\hat{y}$ direction is set to be $L = 4R$. The relaxation time and the particle density are set to $\tau = 1$ and $\rho_p = \rho_f$, respectively. The shear flow is generated by two opposite walls located at $y = \pm L/2$ and moving with a velocity $\pm U_{shear}$. The velocity of the walls is tuned to have $Re = CD^2/\nu = 79.6$, where D is diameter of the cylinder and $C = 2U_{shear}/L$ is the already defined shear rate. This setup is in agreement with the experiments of Zettner and Yoda [144].

The simulation results are presented in Fig. 4.20, and they show a good agreement with the experimental data presented in [144], confirming that for large resolution of the particle BB, EI and CEI recover identical results.

By performing the same simulations at different resolutions, down to $R = 4$, we observed that good accuracy is always recovered for all investigated boundary schemes until a critical resolution limit is reached. Below this threshold the flow is clearly under resolved and the algorithm is unable to capture the correct hydrodynamics for the simulated Re.

The weak relation between the accuracy of the dynamics and the resolution of the particle observed in this section is partially related to the strong symmetry of the investigated systems, combined with the more strict requirements in terms of fluid

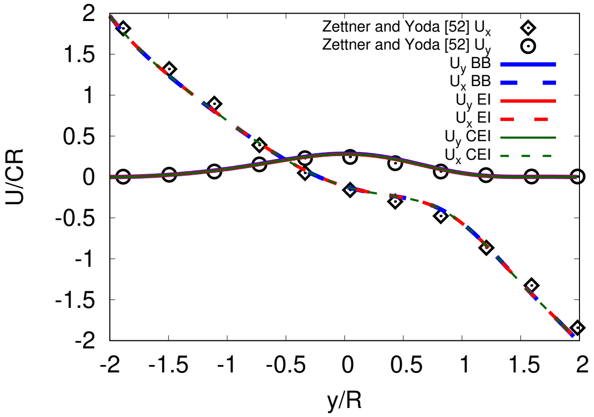

Figure 4.20: The $\hat{x}$ (dashed lines) and $\hat{y}$ (solid lines) velocity components U_x and U_y of the flow versus y/R at the domain section $x/R = -1.8467742$ from a rotating cylinder with radius $R = 64$ centered at $(0, 0)$. The Reynolds number is $Re = 79.6$. The same simulation is performed using BB (blue), EI (red) and CEI (green) and numerical results are in good agreement with the experimental data from Zettner and Yoda [144] (black circles and diamonds) for all the investigated schemes.

resolution needed to simulate higher Re numbers. This last aspect suggests that low-Reynolds number conditions provide a better test case to asses resolution effects related to particle discretization.

Chapter 5

Drag and lift coefficients of ellipsoidal particles under rarefied flow conditions with the DSMC method

While in the previous Chapter we focused on the dynamics of particles in the continuum regime, we now shift our attention to rarefied flows. Since we are interested in the transition and free-molecular regimes, the Direct Simulation Monte Carlo (DSMC) method is the most suitable tool to describe such scenarios. More specifically, we investigate the influence of the orientation of the particle and rarefaction on the drag and lift coefficients, in the case of prolate and oblate ellipsoidal particles immersed in a uniform ambient flow. This is done by modeling the solid particles using the cut-cell algorithm discussed in Chapter 3 within our DSMC solver. In this approach, the surface of the particle is described by its analytical expression and the microscopic gas-solid interactions are computed exactly using a ray-tracing technique. The measured drag and lift coefficients are used to extend the correlations, based on the sine-squared drag law, available in the continuum regime to the rarefied regime, focusing on the transitional and free-molecular regimes. The functional forms of the correlations for the ellipsoidal particles are chosen as a generalization from the spherical case. We show that the fits over the data from numerical simulations can be extended to regimes outside the simulated range of Kn. Our approach allows to achieve a higher precision when compared with existing predictive models from the literature. Finally, we underline the importance of this work in providing new correlations for non-spherical particles that can be used for point-particle Euler-Lagrangian simulations to address the problem of contamination from finite-size particles in high-tech mechanical systems. The material presented in this Chapter closely follows the results and exposition presented in the publication "Drag and lift coefficients of ellipsoidal particles under rarefied flow conditions", *Phys. Rev. E* **105**, 015306, 2022.

The Chapter is structured as follows: Section 5.1 introduced the research topic, as well as the relevant literature. In Section 5.2 we present a detailed analysis and validation of the proposed numerical scheme, showing its capability to recover the drag force exerted by a uniform ambient flow on a spherical particle as well as the accuracy scaling with respect to the spatial and kinetic resolutions of the simulations. In Section 5.3 we introduce and discuss the definition for the Knudsen number for ellipsoidal particles based on the equivalent sphere. In Section 5.4 we propose the predictive model for the drag and lift coefficients of a prolate and oblate ellipsoidal particle. We summarize and discuss our results in Section 5.5.

5.1 Introduction

Numerous studies have been proposed to address the problem of shape influence on the transport of particles in the continuum regime. From the pioneering theoretical work of Oberbeck [46] and Jeffery [47], who firstly investigated the motion of an ellipsoid immersed in a fluid in the Stokes limit, an increasingly growing effort has been dedicated to understand shape and orientation effects on the drag, lift and torque experienced by particles in different flow conditions [48, 49, 146–152].

While the understanding of particle-flow interactions in the continuum regime is consistently increasing through the years, our knowledge on the impact of rarefaction on the dynamics of the particles is still limited. From the numerical point of view, limitations arise as Navier-Stokes solvers fail due to the breakdown of the continuum assumption, while from the experimental point of view it is difficult to create ideal conditions to investigate the dynamics of very small particles in low pressure environments.

Typically, Eulerian-Lagrangian simulations are employed in numerical studies related to the transport of nano-sized particles in micro-mechanical devices [70,71,73,74,153]. In this approach, the flow field is evaluated on Eulerian grids, while the solid bodies are modeled as (spherical) point particles and evolved in time in a Lagrangian fashion. Rarefaction effects are then included through the phenomenological Cunningham corrections [62, 154] on the drag force experienced by the particles. Although, in general, this approach is a reasonable approximation for the dynamics of micro- and nanometric particles immersed in a gas, any effect related to their finite size, shape and orientation is neglected. Such effects are essential in high-tech applications, where high accuracy is required in the modelling approach, so that finite-size effects must often be taken into account.

Different authors addressed, both analytically and numerically, the interaction between rarefied gas flows and a finite-size spherical particle. Epstein [53] firstly derived a drag relation for a sphere translating in a gas at thermal equilibrium in the free-molecular regime in the limit of low velocities. This approach was later extended by Baines [155] to account for larger velocities. Gallis *et al.* [156,157] proposed a a formulation based on the use of Green's function to calculate drag and heat flux experienced by a sphere in the free-molecular regime for monatomic and diatomic gases.

While the aforementioned analyses are focused on the free-molecular regime, Phillips [42] provided an analytical expression for the drag force on a sphere through an approximate solution of the Boltzmann equation which includes the effects of intermolecular collisions. His approach, based on the method of moments [158, 159], is applicable to a large range of Knudsen numbers, covering the slip and transition regimes ($0.0865 \leq Kn \leq 3.36$). The results from Phillips show a good match with the experimental observations from Millikan [60,61]. These approaches are, however, limited to spherical particles and have not been extended, so far, to particles with more complex shapes.

Some works are available in the literature that tackle the problem of gas-solid interactions in the case of non-spherical particles from a theoretical perspective: Halbritter [160] derived a formulation for the torque exerted by a rarefied gas on an ellipsoidal particle at thermal equilibrium. Dahnekë [54] extended the analytical formulation from Epstein to particles with different shapes, including cylinders, prolate and oblate ellipsoids. These studies are again limited to free-molecular flows.

Some phenomenological models have been proposed [75] to describe the drag corrections experienced by non-spherical particles in the transition and slip flow regimes, such as the Equivalent Sphere Approximation (ESA) and the Adjusted Sphere Approximation (ASA) briefly introduced in Chapter 3. As it will be further explained later, these approaches are based on the approximation of the investigated particle with an appropriate spherical volume, and rarefaction effects are included through the Cunningham corrections. The main feature of the ASA model is that it retains orientation effects, but it requires the knowledge of the drag force on the body in the continuum and free-molecular regimes, and this information is only available for a limited number of shapes.

To numerically address rarefied gas flow problems in a broad spectrum of Kn, ranging from slip to free-molecular flows, the Direct-Simulation Monte Carlo (DSMC) method [33,161] has proven to be a stable and accurate approach to accurately model the Boltzmann equation [162, 163]. We employ the DSMC method due to its versatility in including solid particles with different shapes in the simulation domain, combined with its capability to correctly describe rarefaction effects and gas-surface interactions. Two main approaches are usually applied to model the surface of the particle in the DSMC framework: in one case it is approximated by a non-Cartesian body-fitted mesh, and every face on the meshed surface coincides with a DSMC grid cell face on the gas domain [164]. In the second approach, the surface of the particle is represented with its analytical expression and it is free to move on the Cartesian

DSMC grid.

The latter approach, firstly introduced in 1999 by LeBeau [165], has been called the cut-cell method [166, 167], as the super-imposition of the solid particle volume on the DSMC cartesian grid imposes that some of the DSMC grid cells (i.e. the boundary cells at the gas-solid interface) are cut by the solid surface, requiring to dynamically compute and update the volume of such cells. The cut-cell method provides two main advantages: it allows to describe the surface of the particle analytically and, when the motion of the particle is present, it overcomes the need of adaptive re-meshing of the simulation grid at every time step, as only the cut-cells volumes have to be recomputed.

Examples of recent successful applications of the cut-cell method to model gas-particle interactions can be found in the literature: Jin *et al.* [125] proposed an efficient approach to recalculate the cut-cell volume based on a polyhedral approximation of the solid volume fraction in each boundary cell. They apply this approach to spherical particles as well as to particles with more complex surfaces. Shrestha *et al.* [168] applied the cut-cell algorithm to study the Brownian diffusion of a spherical particle in the free-molecular regime and the transport of an arbitrary-shape particle driven by the thermophoretic force. In their formulation the surface of the particle is approximated by a triangulated mesh. Baier *et al.* [169] investigated the thermophoretic force experienced by a spherical Janus particles in presence of an external thermal gradient. Chinnappan *et al.* [170] addressed the transport dynamics of ellipsoidal particles in the free-molecular gas flow regime. The aforementioned studies are focused on the free-molecular regime and, up to our knowledge, an extensive investigation of the drag and lift correlations in the transitional regime is still missing in the literature.

In this work we cover this gap by addressing the impact of a finite Knudsen number ($1 \leq Kn \leq 10$) in the interactions between a gas flow and ellipsoidal particles. This range of Knudsen is particularly relevant for modern industrial problems, as most of the gas flows are not in the free-molecular regime, although still at very low pressure, and the Knudsen number based on the particle size of the contaminant particles often exceeds unity. To efficiently investigate gas-solid interactions at lower values of Knudsen ($Kn < 1$), where the DSMC simulations may become very expensive, alternative techniques can be employed, such as the method of moments [42, 171] or appropriate Lattice-Boltzmann models [31, 172].

We propose a cut-cell algorithm which is able to describe a spheroidal particle exactly, at any aspect ratio. Through the use of a modified ray-sphere intersection approach, the collision points between the gas molecules and the ellipsoidal solid particle are obtained at the exact position on the surface of the particle and the volume of the boundary cells (cut-cells) is computed through a Monte-Carlo approach. This approach differs from both the triangulated approximation of the surface of the solid body proposed in [166–168, 173] and the polyhedral approximation of the cut-cells proposed in [125]. In particular, when compared with modern state-of-the-art, multi-purpose DSMC algorithms [166,173], in which solid surfaces are approximated through a triangulated surface mesh and cut-cell volume evaluated through a cut/split algorithm [166], our approach allows to describe the surface of spheroidal particles via their analytical representation, limiting numerical approximations only to the evaluation of the cut-cells volume. This requires that surfaces can be represented mathematically, and for the more general case of arbitrary-shaped surfaces a generalized approach as the one discussed in Appendix A, or the one used in [166, 173] is required.

We use this algorithm to investigate rarefaction and orientation effects of an impinging uniform gas flow on different ellipsoidal particles. This class of problems can be studied, without loss of generality, by changing the angle of attack at which the gas flow impinges on the simulated particles, as sketched in Fig. 5.1. We firstly aim to verify the validity of the sine-squared drag law in presence of rarefaction. The sine-squared correlation of the drag force experienced by an arbitrary-shaped particle as a function of its orientation was firstly proposed by Happel and Brenner [45] for Stokes flows in the continuum regime, and later extended by Sanjeevi *et al.* [48,49] to larger Reynolds numbers. Here we plan to investigate and extend its validity in the case of rarefied flows.

We perform this analysis for different Knudsen numbers ranging from the transitional to the free-molecular regime by defining a suitable definition of the Knudsen number

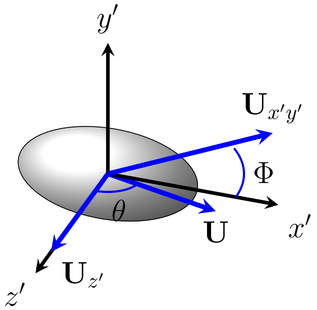

Figure 5.1: Sketch of an ellipsoidal particle immersed in a uniform Stokes flow with velocity $\mathbf{U}$ for an arbitrary orientation. In the body-centered reference, (x', y', z'), the ambient velocity $\mathbf{U}$ can be decomposed in its components $\mathbf{U}_{x'y'}$, laying on the $x'y'$-plane forming an angle Φ with respect to the x' axis, and $\mathbf{U}_{z'}$, laying on the z'-axis. Since $\mathbf{U}_{z'}$ is independent on the relative orientation between the particle and the flow, orientation effects are described by the angle of attack, Φ, without loss of generality.

for ellipsoidal particles. We firstly show that the sine-squared drag law typical for the continuum regime is preserved for the whole range of investigated Knudsen numbers, and then we use this correlation to build a heuristic model which is able to predict rarefaction and orientation effects on the hydrodynamic forces acting on the ellipsoidal particles. Such model can be used to improve existing Euler-Lagrangian simulations of particle transport in rarefied conditions, as it would allow to model ellipsoidal particles and to include orientation effects in the dynamics of the simulated particles.

5.2 Validation of the cut-cell algorithm

In this work we employ the cut-cell technique to model fully-resolved solid particles in the DSMC method discussed in Chapter 3. To validate the algorithm, we firstly perform simulations of a rarefied argon gas flow impinging on a spherical particle in the same conditions as Jin *et al.* [125]. The simulation setup is the following: the radius of the particle is fixed at $R = 0.25\mu$m and the gas temperature is set to $T = 300$K. The gas density, ρ, flow velocity, U_0, and pressure, P, are varied accordingly to the Knudsen number, defined as $Kn = \lambda/R$, and the (particle-based) Reynolds number, $Re = 2U_0R/\nu$, is kept constant and equal to 0.022 to match with the setup from [125]. The mean free path. λ and the gas dynamic viscosity, μ are use the same definition presented in Chapter 3 [Eqs. (3.68) and (3.69)].
The simulation box size $L = 20 \cdot R = 5\mu$m to avoid as much as possible detrimental effects due to the vicinity of the particle to the boundaries of the simulation box. Using 120 DSMC cells per linear direction to discretize the domain is sufficient to respect the rule-of-thumb criteria [33, 123], ensuring high accuracy for all the simulations. This discretization leads to a particle radius of $R = 6$ (cells units). The number of particles-per-cell is set to $N_c = 50$, leading to roughly $8.6 \cdot 10^7$ computational particles. Free-streaming boundary conditions are imposed along the flow direction and periodic boundary conditions are applied along the transverse directions. With this configuration we reach a very high accuracy for the investigated range of Kn and, to give an example, for $Kn = 10$ we have that one computational DSMC particle represents four physical argon atoms.
We validated the proposed algorithm by inspecting the drag force, F_D, experienced by the particles in such setup for two cases: spherical particles in collisional flows and ellipsoidal particles in collisionless flows. In all the simulations presented in this Chapter F_D is averaged over $N_{\Delta t} = 10000$ time steps after an initial transient of 5000 time steps, which is enough to reach the steady state in all investigated cases. The error bars are calculated using the 95% confidence interval defined as $\varepsilon_{95} = 2\sigma_{std}/\sqrt{N_{\Delta t}}$, where σ_{std} is the standard deviation on the average value of F_D. The validation of the

drag force experienced by a spherical particle is presented in Fig. 5.2, where the drag force measured with our DSMC code is compared with the DSMC results from Jin *et al.* [125], as well as with the analytical approximations from Takata *et al.* [59] (based on a direct solution of the Boltzmann equation using a finite-difference approach), and Phillips [42] (based on the method of moments developed by Lees [158, 159] and extensively described in [171]). The results are normalized with respect to the prediction from Phillips, given by:

$$F_{Phil.}(R) = -6\pi\mu R U_0 f(Kn), \tag{5.1}$$

with $f(Kn)$ representing the rarefaction corrections:

$$f(Kn) = \frac{15 - 3c_1 Kn + c_2(8+\pi\sigma)(c_1^2+2)Kn^2}{15 + 12c_1 Kn + 9(c_1^2+1)Kn^2 + 18c_2(c_1^2+2)Kn^3}, \tag{5.2}$$

where $c_1 = \frac{2-\sigma}{\sigma}$, $c_2 = \frac{1}{2-\sigma}$, μ is the gas dynamic viscosity and σ is the momentum accommodation coefficient, with range $0 \leq \sigma \leq 1$. In our simulations $\sigma = 1$ (fully-diffusive surface) and thus $c_1 = c_2 = 1$.

As it can be seen from Fig. 5.2, simulation results with our DSMC method are well aligned with the results available in the literature obtained with similar approaches (see Jin *et al.* [125]). The consistent small deviation between the values obtained with DSMC solvers and those based on the approximations from Phillips [42] and Takata *et al.* [59] are related to the limitations of the different numerical approaches used by [42, 59] to solve the Boltzmann equation. Additionally, the inset shows that setting $L = 120$ is sufficient to exclude detrimental effects due to the finite size of the simulation box.

In the second part of this validation we focus on ellipsoidal particles by comparing results from collisionless simulations with the analytical expressions for the drag force on both prolate and oblate ellipsoidal particles provided by Dahnekë [54]. Dahnekë extended the theoretical approach from Epstein, valid for small streaming velocities, to particles with different shapes, assuming that the reflected gas molecules do not interact with the incoming ones (collisionless limit). We can achieve this in the DSMC simulations by artificially switching off intermolecular collisions. In our simulations we fix the volume of the ellipsoidal particles to the same value as the one used for the spherical particle. The aspect ratio of the ellipsoidal particles is fixed to $a/b = 2$, leading to a major radius $a = 0.39\mu$m for the prolate case and $a = 0.315\mu$m for the oblate case. A sketch of the ellipsoidal particles used in this work is presented in Fig. 5.3.

Similarly to the spherical case, the physical simulation box size is set in relation to the major radius of the simulated particles, so that $L = 20 \cdot a = 8\mu$m. In terms of DSMC cell units, 120 cells per linear direction are again sufficient to ensure a high

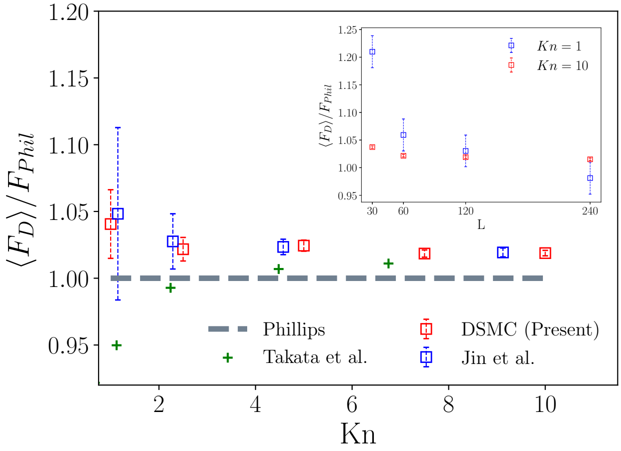

Figure 5.2: Average drag force, $\langle F_D \rangle$, on a spherical particle with radius $R = 0.25\mu$m as a function of the Knudsen number. Our DSMC simulations (red squares) are compared with the DSMC results from Jin *et al.* [125] (blue squares), with the analytical approximation from Phillips [42] (gray dashed line) and from Takata *et al.* [59] (green pluses). In the inset, the effects of varying the simulation box size L, leaving all other parameters unchanged, are reported for $Kn = 10$ (red squares) and $Kn = 1$ (blue squares). The error bars are based on ε_{95}.

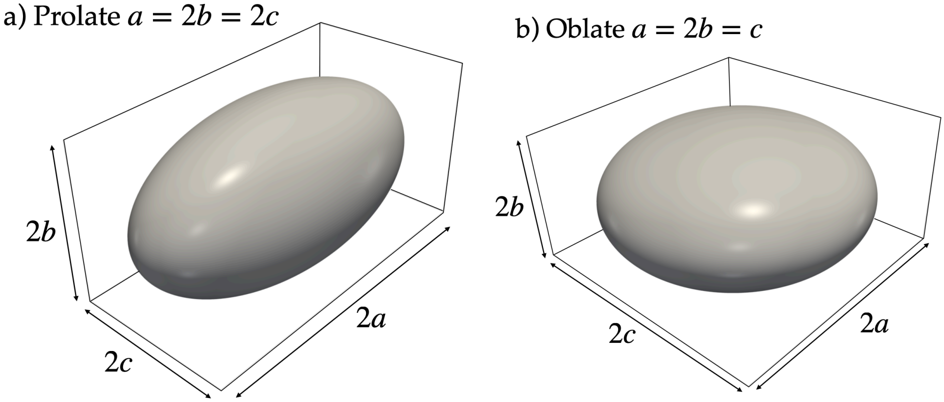

Figure 5.3: Sketch of the prolate (a) and oblate (b) ellipsoidal particles used in this Chapter. The volume of all particles is fixed to $V = 6.5 \cdot 10^{-20}\text{m}^3$.

accuracy for all the simulated cases. The Reynolds number is set to $Re = 0.1$. The agreement between DSMC simulations and the analytical expressions from Dahnekë is excellent, as presented in Fig. 5.4.

The cut-cell algorithm implemented and presented in this study has been incorporated in the parallel DSMC solver validated by Di Staso [20]. The intensive computations required for the DSMC simulations presented in this work, in fact, can become feasible only by taking advantage of parallel computation. This can be easily done for a DSMC algorithm, thanks to the locality of the interactions between gas molecules, by enforcing a three-dimensional Cartesian processor grid on which the DSMC simulation domain is decomposed. The simulations presented in this work are executed on computational nodes with 2 AMD EPYC 7282 CPUs per node, and the individual run wall clock time strongly depends on the Knudsen number, ranging from 20 hours ($Kn \geq 10$) to several days ($Kn \sim 1$) on one node.

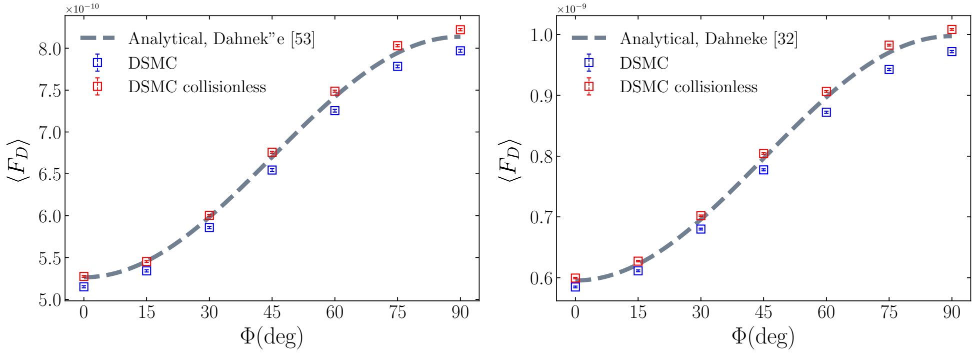

Figure 5.4: Drag force from collisionless DSMC simulations (squares) at $Kn = 10$ for a prolate (left) and oblate (right) ellipsoid with aspect ratio $a/b = 2$, for different orientations Φ, are compared with predictions from Dahnekë [54] (gray dashed lines). For completeness, we also present simulation results when intermolecular collisions are present (blue). The error bars are based on ε_{95}.

To conclude the characterization of the algorithm, an extensive convergence analysis of the mean value of the drag force experienced by the particle, and its standard deviation, is presented in Appendix B.

5.3 Drag correlations for ellipsoidal particles at finite Knudsen number

In this Section we investigate rarefaction and orientation effects on the drag force acting on prolate and oblate ellipsoidal particles, with the aim to provide the fundamental requirements for the predictive model presented in Section 5.4. Such requirements are embodied by the necessity to firstly define an expression for the Knudsen number for ellipsoidal particles that accurately (and consistently) captures rarefaction effects, and, secondly, to confirm the validity of the sine-squared drag law, introduced by Happel and Brenner [45] for the continuum regime, when rarefaction effects are present.

In relation to the definition of a single characteristic length for ellipsoidal particles, a number of authors [48, 49, 151, 174] proposed to use the radius of the sphere with equivalent volume, R_{eq}, to define the Reynolds number. In this work we follow the same approach, extending this choice also to the Knudsen number, so that the relevant dimensionless numbers read $Re = 2U_0 R_{eq}/\nu$, and $Kn = \lambda/R_{eq}$, where $\nu = \mu/\rho$ is the kinematic viscosity of the gas.

In the following of this Section, we show that the proposed definition of Kn is a good approximation to describe rarefaction effects for ellipsoidal particles. Firstly, it successfully reduces the number of characteristic lengths to one (the radius of the equivalent sphere). This aspect not only defines Kn in an unambiguous way, but also makes this definition unrelated to the aspect ratio of the particle and to its orientation. Additionally, the relation between the drag force acting on the equivalent sphere and the one acting on the ellipsoidal particles is preserved independently of the specific value of Kn.

As briefly anticipated in Chapter 2 (see Fig. 2.8), the necessity for rarefaction effects to be unrelated with a specific aspect ratio or orientation of the particle is a well-known results for the collisionless regime. In Chapter 2, in fact, we show that for small free stream velocities (i.e. $s \ll 1$) the correlation typical of the continuum limit is recovered also for the collisionless case. Such correlations are represented by the same sine-squared drag law introduced by Happel and Brenner [45] for the continuum regime and extensively discussed in Section 2.1. This result represents a clear indication that rarefaction effects are independent of the relative orientation between the particle and the incoming flow.

Since the sine-squared drag law represents the fundamental starting point of the analysis presented in this Chapter we will recall its fundamentals. Using the linearity of velocity fields in creeping flows ($Re \ll 1$), in the continuum regime, the drag force on an arbitrary shaped particle oriented at angle Φ with respect to the impinging flow can be expressed as:

$$F_D(\Phi) = F_{D,0^\circ} + (F_{D,90^\circ} - F_{D,0^\circ}) \sin^2 \Phi, \tag{5.3}$$

where $F_{D,0^\circ}$ and $F_{D,90^\circ}$ are the drag force at $\Phi = 0^\circ$ and $\Phi = 90^\circ$, respectively. It is useful to recall (see Fig. 5.1) that Eq. (5.3) is a general expression valid for any arbitrary orientation of the particle.

From Eq. (5.3), Happel and Brenner obtain the correlations for the drag and lift coefficients, which read:

$$C_D(\Phi) = C_{D,0^\circ} + (C_{D,90^\circ} - C_{D,0^\circ}) \sin^2 \Phi, \tag{5.4}$$

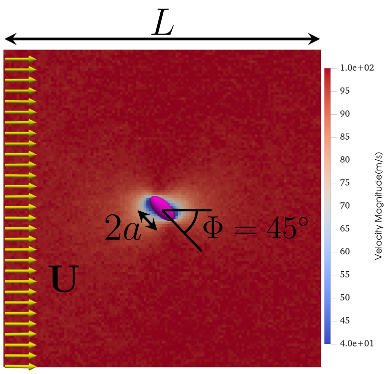

Figure 5.5: Snapshot of the velocity field around a prolate ellipsoidal particle with aspect ratio $a/b = 2$ from a DSMC simulation. The plot represents a cut on the xy plane, crossing the particle center. The particle is immersed in an argon gas flow with free stream velocity $\mathbf{U}$ (yellow arrows) and is oriented at $\Phi = 45°$ with respect to the impinging gas flow. The simulation domain size is set such that $L \geq 20 \cdot a$. In the case shown $Kn = 10$ and $\mathbf{U} = 99.7\hat{x}$m/s.

$$C_L(\Phi) = (C_{D,90°} - C_{D,0°}) \sin\Phi \cos\Phi. \tag{5.5}$$

A confirmation of the validity of Eqs. (5.4)-(5.5) in the free-molecular regime can be found in Section 2.1. Since we found that the sin-squared drag law is valid in both the continuum and the collisionless regime, we expect it to be valid in the whole range of Knudsen independently of the particle shape.

We verify this assumption by performing collisional DSMC simulations at varying $Kn = \lambda/R_{eq}$ and orientation Φ. Like in Section 5.2, the volume of the equivalent sphere is fixed to $V = 6.5 \cdot 10^{-20}$m^3, corresponding to $R_{eq} = 2.5\mu$m. The DSMC grid is set accordingly to the requirements from [33, 123], so that we use a value of $L = 140$ for $Kn = 1$ and a value of $L = 120$ for all other values of Kn $(2, \ldots, 10)$. A snapshot from the DSMC simulation for $Kn = 10$ and $\Phi = 45°$ is presented in Fig. 5.5.

An example of the drag force signal from collisional DSMC simulations of flow on a prolate ellipsoid with $a/b = 2$ oriented at $\Phi = 0°$ for $Kn = 10$ and $Kn = 1$ is presented in Fig. 5.6. Here it can be observed that even in cases where the signal-to-noise ratio $\langle F_D \rangle/\sigma_{std}$ approaches unity (as it happens for the $Kn = 1$ case), the relative error computed from $\varepsilon_{95}/\langle F_D \rangle$ is not larger than $\sim$ 2%, ensuring highly accurate results.

In Fig. 5.7, we compare the drag force on the ellipsoidal particles with the one acting on the equivalent sphere at the same Kn number, as obtained by the prediction of Phillips from Eq. (5.1). The Φ-dependence in Eq. (5.3) is well captured and rarefaction

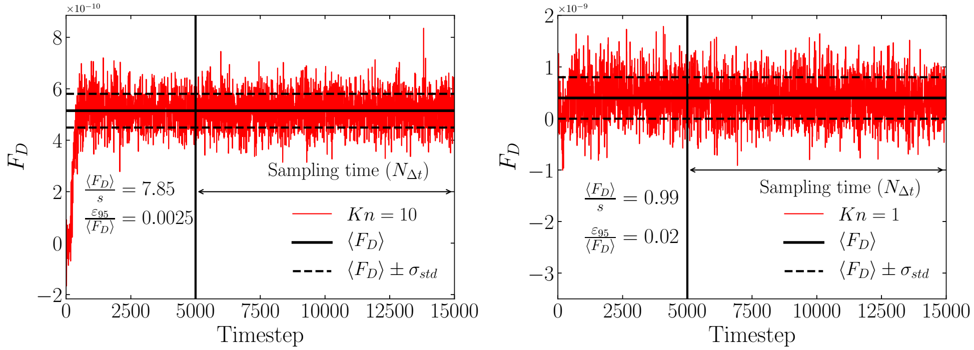

Figure 5.6: Drag force as measured from DSMC simulations (solid red line) on a prolate particle with $a/b = 2$, $\Phi = 0°$ and fully-diffuse surface at fixed $Re = 0.1$ for $Kn = 10$ (left) and $Kn = 1$ (right). The sampling of the drag force used to compute its average, $\langle F_D \rangle$ (solid horizontal black line), starts after 5000 time steps and it lasts for the subsequent $N_{\Delta t} = 10000$ time steps. The standard deviation, s (dashed horizontal black lines), is used to compute the absolute error on the drag force using the 95% confidence interval as $\varepsilon_{95} = 2\sigma_{std}/\sqrt{N_{\Delta t}}$.

effects seem thus in good approximation independent on the orientation of the particle also for finite Kn numbers, as the sine-squared drag law, obtained from the continuum regime, is preserved. Moreover, the relation between the drag force on the equivalent sphere and the one acting on the ellipsoidal particles is maintained for the investigated range of Kn, considering the presence of larger fluctuations at lower Kn cases due to lower kinetic resolution (i.e. the number of real particles described by a single computational particle). In all the investigated cases, in fact, $F_{Phil}(R_{eq})$ crosses the curves obtained from the simulations for the drag force on the ellipsoidal particle, and the intersection happens at $\Phi \sim 41°$ and $\Phi \sim 22°$ for the prolate and oblate case, respectively.

The validity of the sine-squared drag law also in presence of rarefaction is, per se, an important confirmation that can be used to build a predictive model for the drag force on ellipsoidal particles. While in this work we focus on simple uniform flows, it is interesting to investigate whether such relation holds also in more complex situations, such as for particles with more complex shape, in the vicinity of solid walls or in cases where the Knudsen number varies across the fluid domain. We plan to address this class of problems in future studies.

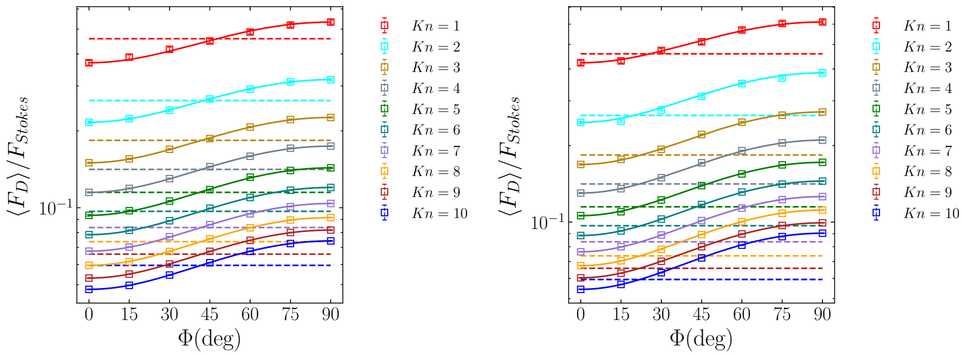

Figure 5.7: Drag force from DSMC simulations for a prolate (left) and oblate (right) ellipsoid as a function of the Knudsen number Kn for different orientations Φ, normalized with respect to the Stokes drag of a spherical particle. The results from the DSMC simulations (squares) are compared with those for the sphere with equivalent volume (dashed lines) given by Eq. (5.1) and with the theoretical correlation (solid lines) obtained by inserting the values of $F_{D,0^\circ}$ and $F_{D,90^\circ}$ from our DSMC simulations into Eq. (5.3). The error bars are based on ε_{95}.

5.4 Predictive model for the Drag and Lift coefficients

In this Section we propose the derivation of a heuristic model for the prediction of the drag and lift coefficients of prolate and oblate ellipsoidal particles. Such model is based on the validity of the sine-squared drag law also in presence of rarefaction and is aimed to extend the available correlations from the continuum to the rarefied regime. For our collisional DSMC simulations we maintain all the parameters the same as in Section 5.3.

Following the work of Sanjeevi *et al.* [48], we define the drag and lift coefficients for an ellipsoidal particle as:

$$C_D = \frac{|\mathbf{F_D}|}{\frac{1}{2}\rho U_0^2 \pi R_{eq}^2}, \tag{5.6}$$

$$C_L = \frac{|\mathbf{F_L}|}{\frac{1}{2}\rho U_0^2 \pi R_{eq}^2}, \tag{5.7}$$

where $\mathbf{F_L}$ is the lift force acting on the particle, ρ is the density of the gas, U_0 is the gas free-stream velocity. Since we are investigating uniform flows in the Stokes regime, the pitching torque is known to vanish in such conditions [44] due to the absence of an external rotational field, and thus the analysis of the pitching torque is not relevant in the scope of this work.

We can directly apply Eqs. (5.4)-(5.5) to obtain the analytical relations for the drag and lift coefficients, with respect to the angle of attack Φ, of the simulated ellipsoidal particles. Here $C_{D,0^\circ}$ and $C_{D,90^\circ}$ can be obtained by measuring the drag force experienced by the particles in our DSMC simulations and the results are shown in Fig. 5.8. As expected from the analysis presented in the previous Section, simulations results are in excellent agreement with the theoretical predictions.

In the following of this Section we will provide a heuristic model for $C_{D,0^\circ}$ and

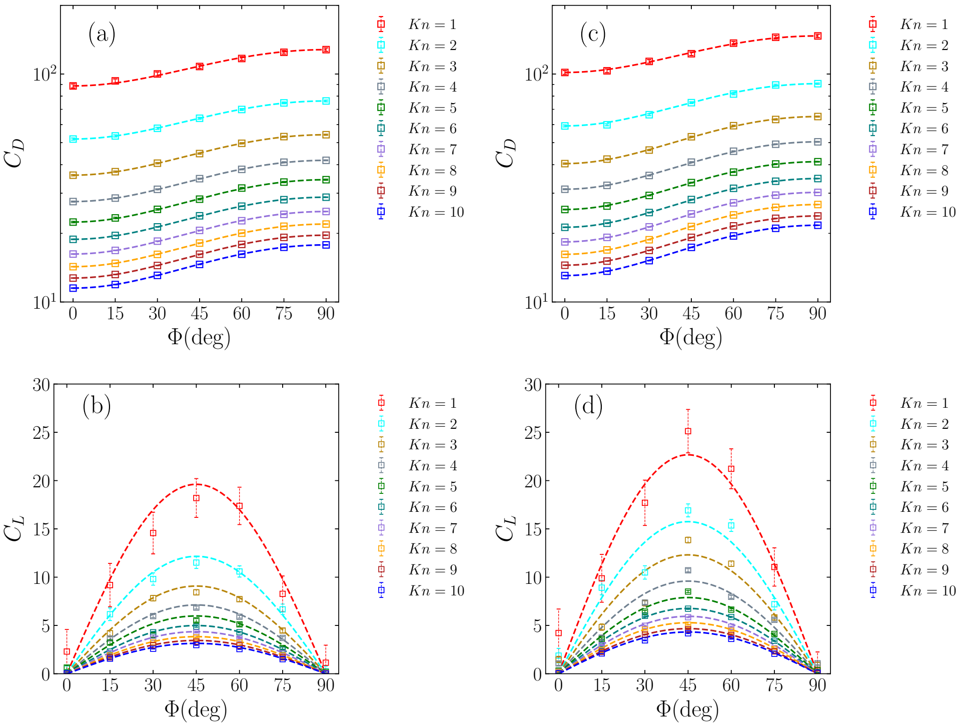

Figure 5.8: Comparison between Eqs. (5.4)-(5.5) (dashed lines) and results from DSMC simulations (squares) for the drag (C_D) and lift (C_L) coefficients of a prolate (a, b) and an oblate (c, d) ellipsoid for different orientations Φ and Kn. Both ellipsoids have aspect ratio $a/b = 2$. In order to use Eqs. (5.4)-(5.5) in this context, we computed $C_{D,0^\circ}$ and $C_{D,90^\circ}$ directly from our DSMC simulations. The C_D data is plotted in semi-log scale for a better readability.

$C_{D,90^\circ}$ that takes into account rarefaction effects, in the attempt to include in Eqs. (5.4)-(5.5) a dependence on the Knudsen number. Our starting assumption is that, similarly to the spherical case, an equation for C_D that includes rarefaction effects for ellipsoidal particles can be written as a product between C_D in the continuum limit and a function $g(Kn)$ which represents a small perturbation with respect to the spherical case:

$$C_{D,0^\circ}(Kn) = \underbrace{C_{D,0^\circ}^{cont}}_{\text{continuum}} \cdot \underbrace{g_{0^\circ}(Kn)}_{\text{rarefaction effects}} , \tag{5.8}$$

$$C_{D,90^\circ}(Kn) = \underbrace{C_{D,90^\circ}^{cont}}_{\text{continuum}} \cdot \underbrace{g_{90^\circ}(Kn)}_{\text{rarefaction effects}} , \tag{5.9}$$

where $C_{D,0^\circ}^{cont}$ and $C_{D,90^\circ}^{cont}$ are the drag coefficients in the continuum regime, while $g_{0^\circ}(Kn)$ and $g_{90^\circ}(Kn)$ are model functions to be evaluated. In order to use Eqs. (5.8) and (5.9), we first need to compute the values of $C_{D,0^\circ}^{cont}$ and $C_{D,90^\circ}^{cont}$ for the ellipsoidal particles investigated in this work. This can be done using the Schiller-Neumann [175] drag expression for the drag coefficient of a spherical particle,

$$C_D^{sph} = \frac{24}{Re}\left(1 + 0.15Re^{0.687}\right), \tag{5.10}$$

which has proven to be quite accurate up to a moderate Reynolds number. We can then obtain $C_{D,0^\circ}^{cont}$ and $C_{D,90^\circ}^{cont}$ for the simulated ellipsoidal particles using the heuristic relations from Happel and Brenner [45]:

$$C_{D,0^\circ}^{cont} = C_D^{sph} K_{0^\circ}, \tag{5.11}$$

$$C_{D,90^\circ}^{cont} = C_D^{sph} K_{90^\circ}. \tag{5.12}$$

The correction factors K_{0° and K_{90° depend on the shape of the particle and for regular prolate and oblate ellipsoidal particles in creeping flow conditions, the exact analytical expressions for the correction factors were derived by Oberbeck [46] as a

	Prolate	Oblate
$C_{D,0^\circ}$	236	247
$C_{D,90^\circ}$	270	282

Table 5.1: Values of $C_{D,0^\circ}$ and $C_{D,90^\circ}$ (three-digit accuracy) for a prolate and oblate ellipsoid with aspect ratio $a/b = 2$. Results are obtained from the theoretical prediction given by Eqs. (5.11) and (5.12) using the correction factors from Eqs. (5.13)-(5.16) and the expression for C_D^{sph} from Eq. (5.10).

function of their major and minor axes a and b, respectively:

$$K_{0^\circ}^{pr} = \frac{(4/3)(a/b)^{-1/3}(1-(a/b)^2)}{a/b - \frac{(2(a/b)^2-1)\ln\left((a/b)+\sqrt{(a/b)^2-1}\right)}{\sqrt{(a/b)^2-1}}}, \tag{5.13}$$

$$K_{90^\circ}^{pr} = \frac{(8/3)(a/b)^{-1/3}((a/b)^2-1)}{a/b + \frac{(2(a/b)^2-3)\ln\left((a/b)+\sqrt{(a/b)^2-1}\right)}{\sqrt{(a/b)^2-1}}}, \tag{5.14}$$

$$K_{0^\circ}^{ob} = \frac{(8/3)(b/a)^{-1/3}((b/a)^2-1)}{b/a - \frac{(3-2(b/a)^2)\cos^{-1}(b/a)}{\sqrt{1-(b/a)^2}}}, \tag{5.15}$$

$$K_{90^\circ}^{ob} = \frac{(4/3)(b/a)^{-1/3}(1-(b/a)^2)}{b/a + \frac{(1-2(b/a)^2)\cos^{-1}(b/a)}{\sqrt{1-(b/a)^2}}}. \tag{5.16}$$

Ouchene *et al.* [151] show that for creeping flows, the set of Eqs. (5.13)-(5.16) predicts the drag coefficients of prolate ellipsoids with different aspect ratios with very high accuracy. We then compute $C_{D,0^\circ}^{cont}$ and $C_{D,90^\circ}^{cont}$ by substituting Eq. (5.10) into Eqs. (5.11) and (5.12), using the corrections given by Eqs. (5.13)-(5.16). The results are shown in Table 5.1, and can be used in Eqs. (5.11)-(5.12) to obtain C_D for the ellipsoidal particles used in this work.

To address rarefaction effects, we propose the following choice for the general expression of the functions $g_{0^\circ}(Kn)$ and $g_{90^\circ}(Kn)$, where we assume that such effects on ellipsoidal particles can be described as small variations with respect to the function $f(Kn)$ for the spherical case:

$$g_{0^\circ}(Kn) = f(Kn) + \frac{a_{0^\circ}}{b_{0^\circ} + c_{0^\circ}Kn}, \tag{5.17}$$

$$g_{90^\circ}(Kn) = f(Kn) + \frac{a_{90^\circ}}{b_{90^\circ} + c_{90^\circ}Kn} \tag{5.18}$$

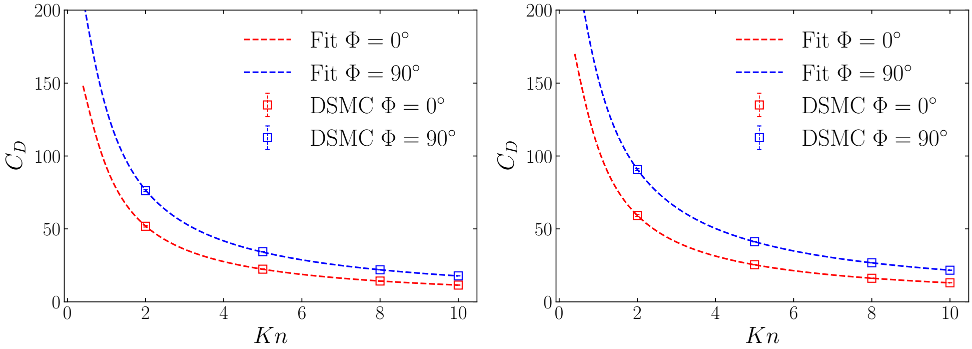

Figure 5.9: Fit of DSMC simulation data of $C_{D,0^\circ}$ (red) and $C_{D,90^\circ}$ (blue) using the functions in Eqs. (5.17)-(5.18), for a prolate ellipsoid (left) and an oblate ellipsoid (right). Fitted curves (dashed lines) represent the model functions given by Eqs. (5.8) and (5.9). The resulting fit parameters are presented in Table 6.1.

where a, b and c are free parameters to be determined separately for $C_{D,0^\circ}$ and $C_{D,90^\circ}$.

We show that with the proposed choice of the $g(Kn)$ functions, it is sufficient to fit the model on a small set of Kn to obtain a robust predictive model for rarefaction effects on ellipsoidal particles. The simulation data is split in two groups:

$$Kn_{fit} = 2, 5, 8, 10.$$

$$Kn_{test} = 1, 3, 4, 6, 7, 9, 20.$$

We then perform a fit of $C_{D,0^\circ}$ and $C_{D,90^\circ}$ from simulation data as a function of Kn, using only the Kn_{fit} set and the fit functions given by Eqs. (5.8) and (5.9). The results of the fit are shown in Fig. 5.9 and the obtained fit parameters are given in Table 6.1. Now Eqs. (5.17)-(5.18) are fully defined and we can proceed with the test of the model.

Once the functions $g(Kn)$ are determined for the needed orientations, we can verify if the model succeeds in the prediction of C_D at different values of Kn and Φ. In order to do so we plug Eqs. (5.8) and (5.9) into Eq. (5.4) to obtain the final model equation for $C_D(\Phi, Kn)$:

$$C_D(\Phi, Kn) = C^{cont}_{D,0^\circ} g_{0^\circ}(Kn) + (C^{cont}_{D,90^\circ} g_{90^\circ}(Kn) - C^{cont}_{D,0^\circ} g_{0^\circ}(Kn)) \sin^2 \Phi. \tag{5.19}$$

The comparison between Eq. (5.19) and the results from DSMC simulation is performed on both the data sets Kn_{fit} and Kn_{test}, where the latter set has not been used

	Prolate		Oblate	
	$\Phi = 0°$	$\Phi = 90°$	$\Phi = 0°$	$\Phi = 90°$
a	-0.171	0.115	-0.219	0.223
b	1.023	2.492	3.762	1.523
c	1.482	1.603	2.916	1.126

Table 5.2: Fit parameters obtained using Eqs. (5.8) and (5.9) to fit $C_{D,0^\circ}$ and $C_{D,90^\circ}$ as obtained from DSMC simulations. These parameters are used to define the functions $g_{0^\circ}(Kn)$ and $g_{90^\circ}(Kn)$, which general expression is given in Eqs. (5.17)-(5.18).

during the fit process. The results are shown in Fig. 5.10, where we can observe an excellent agreement between the proposed model and the simulations. Particularly relevant is the agreement between the model and the data for Kn_{test}, showing that the model correctly predicts rarefaction effects on values of Kn that were not included in the fitting process and it can be extended to the regimes with $Kn \leq 2$ and $Kn \geq 10$.

In an analogous way, we investigate the capability of the predictive model given by Eqs. (5.8)-(5.9) to address the lift coefficient C_L of the different ellipsoids. Following the same approach we used for the evaluation of C_D, we plug Eqs. (5.8) and (5.9) into Eq. (5.5) to obtain the model equation for C_L:

$$C_L(\Phi, Kn) = (C^{cont}_{D,90^\circ} g_{90^\circ}(Kn) - C^{cont}_{D,0^\circ} g_{0^\circ}(Kn)) \sin\Phi \cos\Phi. \tag{5.20}$$

We can now compare the prediction from Eq. (5.20) with the C_L obtained from the DSMC simulations, again using the same approach to separate the data into Kn_{fit} and Kn_{test}. The results of the comparison are shown in Fig. 5.11. The model prediction is in reasonable agreement with the simulation data, considering that $C_L \ll C_D$, leading to a lower signal/noise ratio from the DSMC simulations for C_L with respect to C_D.

In the last part of this Chapter, we compare the performances of the predictive model proposed in this work with existing phenomenological models available in the literature used to predict the drag on non-spherical particles at different Knudsen numbers, namely the previously mentioned (see Section 2.5) ESA and ASA, as defined by Dahnekë [75].

The results of the comparison, limited to some of the values in Kn_{test} set, are presented in Fig. 5.12, where we use the results provided by [75] to compute the ASA prediction for the spheroidal particles investigated in this work. The performances of the proposed model in reproducing C_D show a general improvement with respect to the ASA model, and this is particularly evident for the oblate case. This is due to the larger departure from the spherical case of oblate ellipsoids, as the ASA model

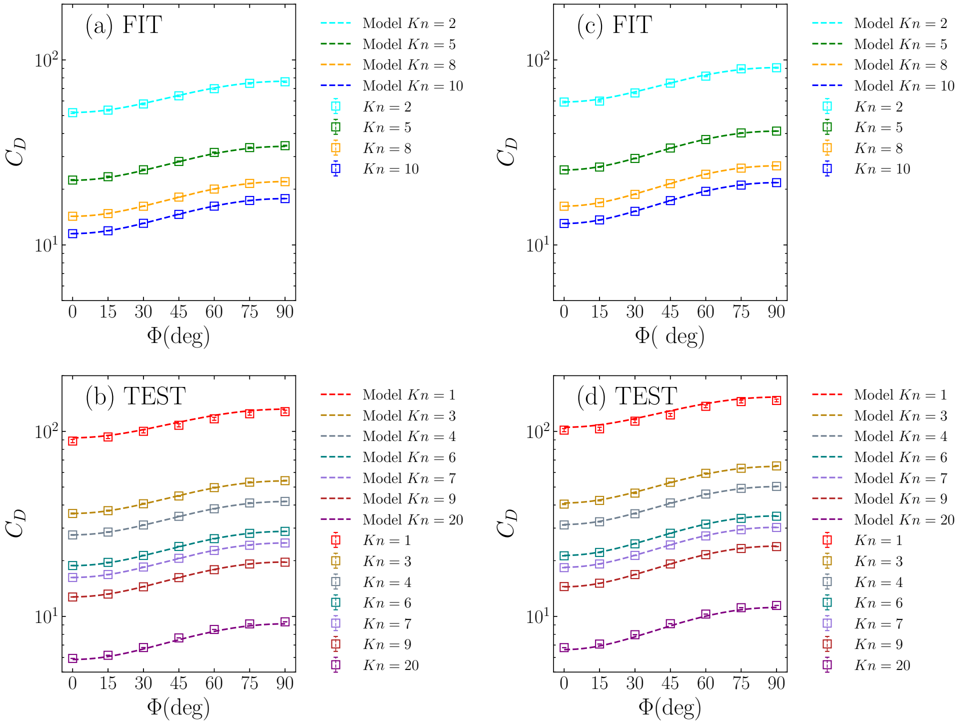

Figure 5.10: Comparison between DSMC simulations (colored squares) and model predictions (colored dashed lines) of the drag coefficient C_D of a prolate (a, b) and an oblate (c, d). The model predictions, given by Eq. (5.19), are then compared with the fit set (a, c) and the test set (b, d). In both cases the match is excellent.

appears to be less accurate the higher this departure is.

The presented approach is proven to be successful in predicting rarefaction effects on the forces exerted on ellipsoidal particles, and shows that it is possible to describe such effects with a perturbative approach from the spherical case. Our results are, however, currently limited to the investigated aspect ratio ($a/b = 2$) and for fully-diffusive surfaces ($\sigma = 1$). In our future works we plan to extend the predictive model to a larger range of aspect ratios, including also effects from a momentum accommodation coefficient σ lower than unity to take into account the presence of specular reflections to model more realistic gas-surface interactions.

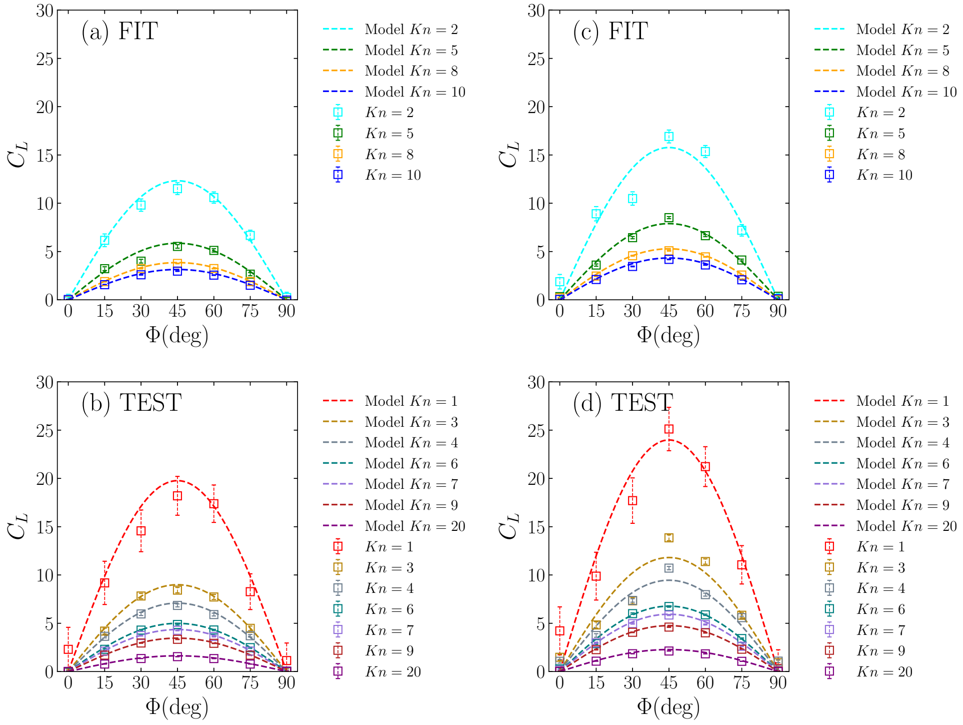

Figure 5.11: Comparison between the lift coefficient C_L from DSMC simulations (colored squares) and the predictive model (dashed lines) for a prolate (a, b) and an oblate (c, d) ellipsoid. The model predictions, given by Eq. (5.20) are then compared with the fit set (a, c) and the test set (b, d).

5.5 Concluding remarks

In conclusion, we developed a two-way coupled algorithm to address interactions, under rarefied conditions, between gas flows and spheroidal particles based on momentum exchange for our in-house DSMC numerical code. The surface of the solid particle is defined by its analytical expression and the interactions between the gas and the rigid body are computed from a microscopic approach. The collision points at which the computational molecules impinge on the solid surface are obtained through a ray-tracing technique, allowing an exact computation of the collision points of the gas molecules impinging on the solid surface.

The algorithm features the cut-cell method to address the DSMC grid cells that are partially covered by the solid volume. We use a Monte-Carlo approach to evaluate the volume of the boundary cells, showing that for an appropriate number of trials, it is

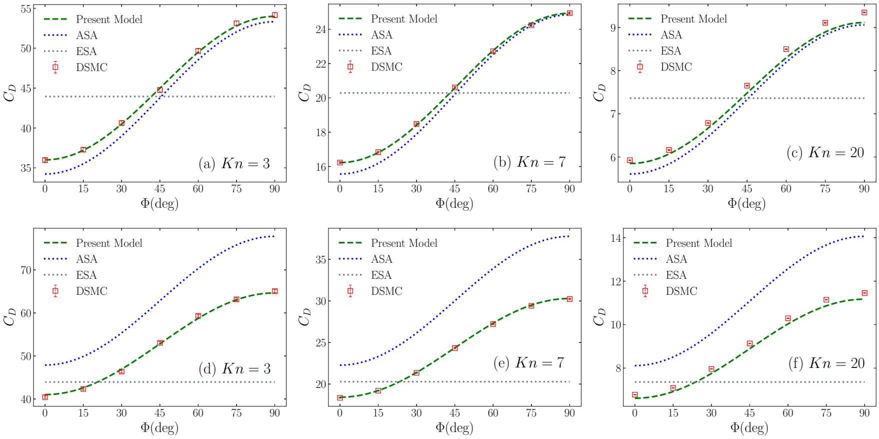

Figure 5.12: Comparison of the C_D predictions as obtained with the present model (green dashed line), with the ASA (blue dotted line) and ESA (gray dotted line) models as defined in [75] for different values of Kn from the Kn_{test} for a prolate (a, b, c) and oblate (d, e, f) with internal aspect ratio $a/b = 2$. The predictions from the models are also compared with direct results from DSMC simulations (red squares).

possible to recover the volume of the interested cells with great accuracy.

The algorithm is validated by computing the drag force on spherical and ellipsoidal particles immersed in a uniform argon gas flow in different conditions. We show that the measurements from our simulations are in good agreement with different results available in the literature, especially when compared with analogous DSMC methods. The accuracy scaling of the mean value and of the standard deviation of the drag force is investigated with respect to the spatial and kinetic resolutions of the system in Appendix B.

We then address the impact of shape, orientation and rarefaction on the drag force for a prolate and an oblate ellipsoid. We firstly propose a suitable definition of the Knudsen number, Kn, for ellipsoidal particles based on the radius of the sphere of equivalent volume and then we show that the sin-squared drag law typical of the continuum regime is valid also in presence of rarefaction. Orientation and rarefaction effects are, in fact, not related, and it is possible to address them separately.

Finally, we develop a heuristic model to predict the drag and lift coefficients for ellipsoidal particles in a range of Kn that includes the transition and the free-molecular regimes. The predictive model is based on the assumption that rarefaction effects on ellipsoidal particles can be represented as small perturbation with respect to the spherical case. These perturbations are obtained through a fit of our simulation data. The model obtained with this procedure shows robust performances in predicting drag and lift coefficients in the investigated range of Kn, and we show that the model can be successfully applied outside of the range of Kn used for its derivation. Moreover, the model proposed in this work offers better predictions when compared to phenomenological models such as the Equivalent Sphere Approximation (ESA) and the Adjusted Sphere Approximation (ASA), especially for the oblate ellipsoid case, where the shape of the particle largely deviates from the spherical case.

We emphasize that the results from this work can be used to improve the available models used in Euler-Lagrangian simulations of particles in rarefied conditions, as the drag and lift correlations can now be extended to the rarefied regimes. This allows in principle to include shape and orientation effects in point-particles simulations, greatly increasing the capability to simulate suspensions of non-spherical particles in rarefied gas flows, which are expected to follow different trajectories with respect to the spherical case. Such feature is of valuable interest in modern high-tech applications, as it can help to improve the state-of-the-art techniques typically employed to address problems such as contamination from particles in low-pressure environments. While we show results for particles with aspect ratio $a/b = 2$ and with fully diffusive surface, in our future works we plan to extend the proposed technique to ellipsoids with different complex aspect ratios, such as needles and disks, and to include a study of the impact of different momentum accommodation coefficients, by taking into account the presence of specular reflections at the gas-solid interface.

5.6 Appendix A: accuracy scaling of the cut-cell algorithm

In this Appendix, we aim to investigate the accuracy scaling of the cut-cell algorithm proposed in this work with respect to spatial and kinetic resolution, separately. The former is related to the impact of different sizes of the particles (in cell units), and is embodied by the parameters L_c/λ and the particle radius R. The latter represents the number of real particles described by a computational particle and is tuned via the number of particles-per-cells, N_c. This kind of analysis is, up to our knowledge, not available in the literature, and it is important to understand the impact of different parameters, such as the resolution of the solid particle and the number of particles-per-cell, on the accuracy of the DSMC simulations.

In the first analysis, we compare the relative error on the mean value and the standard deviation of the drag force on a spherical particle at $Kn = 10$ for different values of the particle radius, R (in cells units). This is done by fixing the total number of DSMC molecules and by fixing the simulation time step, to ensure that the number of collisions per time step is unchanged between different resolutions. We do so to isolate the effects induced by varying the simulation grid size on the overall simu-

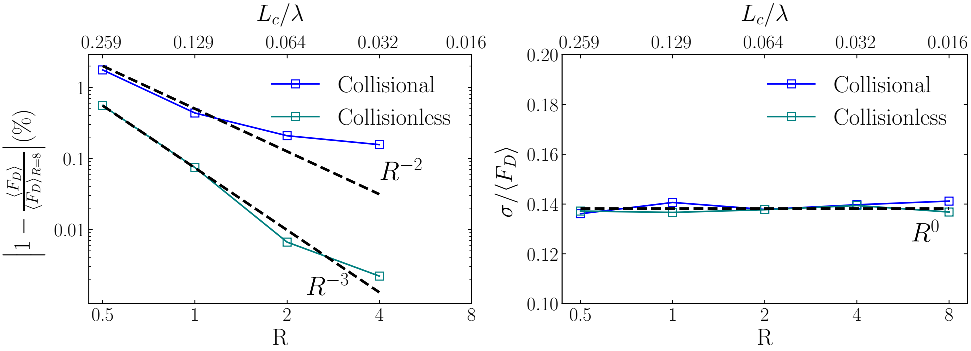

Figure 5.13: Relative error (left) and standard deviation (right) of the mean value of the drag force, $\langle F_D \rangle$, for a spherical particle at $Kn = 10$, as a function of the spatial resolution of the solid particle R. Results from collisional (blue) and collisionless (green) DSMC simulations are included. The relative error is computed with respect to the value of $\langle F_D \rangle$ measured at $R = 8$.

lation accuracy. The ratio between the simulation box size and the particle radius is fixed to $L/R = 20$, so that varying the resolution of the particles is equivalent to vary the value of the DSMC spatial resolution given by L_c/λ. By imposing the same time step between different simulations we finally ensure that the number of collisions per time step between the DSMC molecules and the solid particle is the same for all the simulations, leading to a constant standard deviation.

The results are shown in Fig. 5.13, where we observe that when intermolecular collisions are present, the relative error on the mean value of the drag force exhibits a second-order scaling with respect to the spatial resolution for small values of R, while it deviates from the scaling law for larger values of R. This deviation is related to the approaching of the DSMC resolution limits in resolving stochastic intermolecular collisions as, in this setup, the number of particles-per-cell, N_c, decreases for increasing R as a consequence of keeping the total number of particles unchanged. Once intermolecular collisions are switched off, in fact, the error is drastically reduced and it shows a consistent third-order convergence with respect to spatial resolution. Interestingly, the algorithm offers a remarkable good accuracy also for cases where the radius of the particle is of the order of one DSMC cell, allowing to correctly resolve the drag for particles with a small curvature with respect to the DSMC spatial grid resolution.

We checked also the accuracy scaling with respect to the kinetic resolution. This is done by fixing the particle radius to $R = 4$ (and thus $L_c/\lambda = 0.032$) and by varying the number of particles-per-cell, N_c. Results are shown in Fig. 5.14, where it can be observed that both the scaling of the mean value of the drag force and of its standard deviation are in agreement with the typical results of a DSMC simulation, with the former scaling linearly with N_c and the latter scaling as ${N_c}^{-1/2}$.

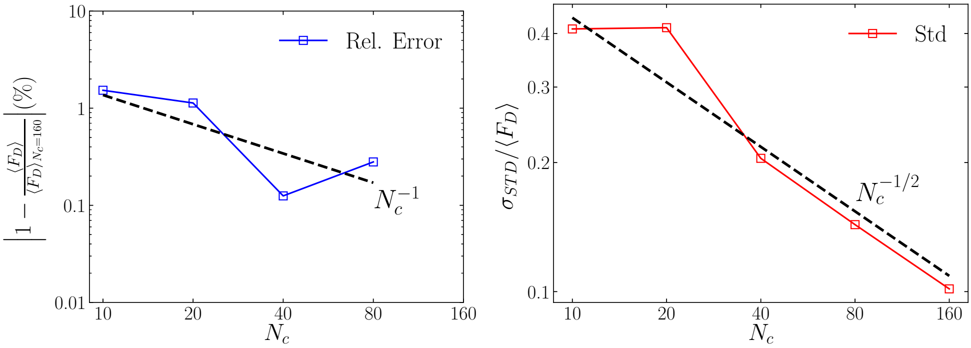

Figure 5.14: Relative error (left) and standard deviation (right) of the mean value of the drag force, $\langle F_D\rangle$, for a spherical particle at $Kn = 10$, as a function of the kinetic resolution, given by the number of particles-per-cell, N_c. In this analysis the ratio between the simulation box size and the radius of the particle is $L/R = 20$ and the radius of the particle is set to $R = 4$. The relative error is computed with respect to the value of $\langle F_D\rangle$ measured at $N_c = 160$.

Chapter 6

Extension of drag model for ellipsoidal particles in complex scenarios

In the previous Chapter we propose an approach to derive heuristic models to predict the drag and lift experienced by prolate and oblate ellipsoidal particles immersed in a uniform rarefied gas flow, limiting our derivation to one specific particles aspect ratio and assuming fully-diffuse gas-surface interactions. In this Chapter we aim to cover this gap by deriving, again from fully-resolved DSMC simulations, improved models for the drag force acting on ellipsoidal particles with different aspect ratios. In this improved formulation we will also include the capability to predict effects related to gas-surface interactions via the tangential momentum accommodation coefficient (TMAC). Similarly to the results presented in the previous Chapter, the derived models are obtained for isothermal, subsonic flows that are typically found in high-tech lithography machines. These models can be used as corrections (to include shape, orientation and TMAC effects) in standard Euler-Lagrangian Point Particles simulations in rarefied gas flows. Additionally, we show that the obtained drag corrections, formally valid for unbounded gas flows, can potentially be applied also in cases where the particle moves in proximity to a solid wall. We do so by investigating near-wall effects on the drag of a prolate ellipsoidal particle. Due to confinement effects, the drag increases when compared to the unbounded case, but such effects are typically negligible for large Kn also in cases in which the particle is in contact with the solid wall. The content of this Chapter is based on the paper "Modelling drag coefficients of ellipsoidal particles in rarefied flow conditions", currently under revision and available as a pre-print (arXiv:2208.06172).

The rest of the Chapter is structured as follows: in Section 6.1 we provide an general introduction to the topics discussed in this Chapter. In Section 6.2 we derive the predictive models for the drag coefficient of ellipsoidal particles with different aspect ratios immersed in a uniform ambient flow. Such models include rarefaction, orientation, and gas-surface interaction effects, and we show they correctly reproduce

DSMC data on a broad range of Kn. In Section 6.3, we modify the simulation setup by adding solid walls to the simulation box boundaries perpendicular to the vertical direction, and we locate the ellipsoidal particle in proximity of the top wall. We show that the presence of the wall increases the effective drag experienced by the particles, leading to a deviation from the sine-squared drag law typical of the unbounded case. Since such effects quickly vanish at increasing Knudsen and particle-wall distance, drag corrections from Section 6.2 can be applied also in confined flow domains conserving good accuracy (assuming large particle-based Knudsen and that the size of the particle is much smaller than the typical system size). Finally, in Section 6.4, we summarize and discuss our results.

6.1 Introduction

As discussed in the previous Chapters, micro and nanoparticles play an important role in a large variety of fields including aerospace industry [5, 6, 176], drug delivery [10–12] and contamination control in high-tech mechanical systems [7–9]. In many numerical investigations, involving the transport of micro- and nano-sized particles in gas flows, Eulerian-Lagrangian simulations are employed [70–74, 177, 178]. In this approach, the flow field is evaluated on Eulerian grids, while spherical particles are modeled as Lagrangian points whose positions and velocities are evolved in time and rarefaction effects are included through the Cunningham correction [62], which represents a rarefaction correction to the Stokes drag experienced by spherical particles.

While the Cunningham correction is widely used to model the drag force on spherical bodies, for non-spherical particles any explicit relation to their finite size and shape is neglected. Moreover, also when only spherical particles are considered, the Cunningham correction does not include a dependence on TMAC, i.e. the relation with the type of reflections that the gas molecules undergo when they hit the solid surface of the particle. From the pioneering work of Millikan [60, 61], in fact, it is assumed that a large majority of gas-surface reflections is diffusive. This assumption has been later verified by Buckley et al. [76], who found that a value for the tangential accommodation coefficient of $\sigma = 0.809$ described Millikan's results with good accuracy. If smaller particles, such as nano-particles, are considered, however, a larger fraction of specular reflections can appear [1], in particular for particles with a diameter smaller than 20nm, leading to a reduced accuracy of the Cunningham correction.

By extending the work presented in the previous Chapter, in this study we aim to address these aspects by deriving accurate heuristic predictive models for the drag experienced by ellipsoidal particles with different aspect ratio, orientation and TMAC, immersed in a uniform rarefied gas flow. Such models are derived by fitting data from

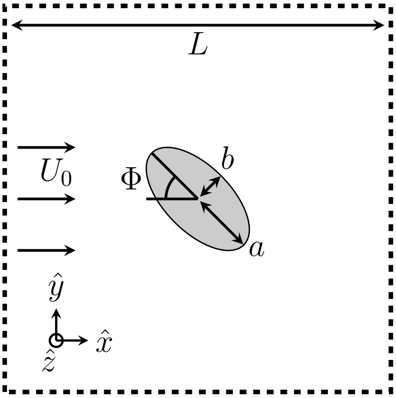

Figure 6.1: Sketch of the simulation setup: an ellipsoidal particle with aspect ratio a/b is immersed in a uniform gas flow with ambient velocity U_0. The particle is at the center of a cubic simulation box of size $L = 20a$, at which free streaming boundary conditions are applied on the faces orthogonal to $\hat{x}$, and periodic boundary conditions elsewhere. We perform simulations varying the angle of attack, Φ, the Knudsen number, Kn (by varying the pressure and density of the gas), the aspect ratio, a/b, and the tangential momentum accommodation coefficient, σ.

fully-resolved DSMC simulations, performed using our in-house code (described in Chapter 3), using the same two-way coupled cut-cell algorithm employed for Chapter 5 and discussed in Chapter 3. Our results are currently focused on subsonic, isothermal conditions typical of contamination control in high-tech mechanical systems (more about this aspect will be discussed in Section 6.2).

The core of our approach lays on the observation that the sine-squared drag law, firstly introduced by Happel and Brenner for the continuum and low-Reynolds number regime [45] (later extended by Sanjeevi *et al.* to the high-Reynolds regime [48,49]), is also valid in the low-Reynolds number, rarefied gas flow case. The sine-squared drag law, given by

$$C_D(\Phi) = C_{D,0^\circ} + (C_{D,90^\circ} - C_{D,0^\circ}) \sin^2 \Phi, \tag{6.1}$$

states that the drag coefficient (and, thus, the drag force) of an arbitrary shaped particle at a given orientation Φ with respect to the uniform flow can be fully characterized by its values at 0° and 90°. In this way, it is sufficient to obtain predictive models able to reproduce the drag at the orientations of 0° and 90° and use Eq. (6.1) to extend the prediction in the whole range of Φ. A geometry relevant for this study in which the sine-squared drag law can be applied is shown in Fig. 6.1.

We perform DSMC simulations at finite Knudsen number ($2 \leq Kn \leq 10$) to derive the predictive models as analytical functions of Kn, Φ and TMAC (σ), for different particle aspect ratios. We show that the predictions of the models are in good agreement with DSMC data that is not used during the fitting process, also when data outside of the fitting range is considered (confirming the validity of the derived relations). The models derived in this work can be used to greatly improve Euler-Lagrangian Point Particles simulations by providing corrections to the drag coefficient of the particle that include effects with regards to shape, rarefaction, orientation and tangential accommodation coefficient.

While these results are formally valid only in unbounded fluids, in the last part of this Chapter we show that the drag corrections obtained with the proposed approach can be safely employed also in the non-ideal cases where the unbounded condition is not preserved, for example in cases when domain walls are present. Through a minor modification of the simulation setup, we investigate the near-wall effects on the drag force experienced by a prolate ellipsoidal particle (we focus on the prolate case to restrict the number of parameters in play) located in the vicinity of a solid wall for different orientations, distances from the wall and rarefaction levels. We show that the Φ-dependence of the drag force exhibits a deviation with respect to the sine-squared drag law of the unbounded case, but such effects are negligible for $Kn \geq 2$ and they vanish quickly as soon as the particle distance with the wall increases. Since we aim to apply the drag corrections derived in this work for large Knudsen number and in cases where the particles spend on average the majority of the time far away from the walls, we can conclude that near-wall effects can be neglected in most of the cases of interest.

6.2 Effects of the aspect ratio and gas-surface interactions at finite Knudsen number

In Chapter 5 we have shown that it is possible to model orientation and rarefaction effects on simple ellipsoidal particles immersed in a uniform ambient flow by using a perturbative approach where rarefaction effects are modeled as a continuous function of Knudsen. Such function is obtained through a fit of the drag force experienced by the particles, as measured from DSMC simulations, for the two cases with orientation at $\Phi = 0^\circ$ and $\Phi = 90^\circ$, with respect to the uniform ambient flow. Orientation effects are then extrapolated for all values of Φ through the sine-squared drag law [Eq. (6.1)], which we show is still valid also for rarefied conditions. Since the discussion presented in Chapter 5 will be the starting point of this work, we will briefly summarize the main concepts. We proposed a model for the drag coefficient on ellipsoidal particles based on the following expression:

$$C_{D,\chi}(Kn) = \underbrace{C_{D,\chi}^{cont}}_{\text{continuum}} \cdot \underbrace{g_{\chi}(Kn)}_{\text{rarefaction effects}}, \tag{6.2}$$

where the subscript χ refers to the two cases with $\Phi = 0°$ and $\Phi = 90°$, separately, $C_{D,\chi}^{cont}$ is the drag coefficient of the ellipsoidal particles under investigation in the continuum regime and $g_{\chi}(Kn)$ is the model function to be determined. Note that, in the subsonic case, an eventual dependence on the Re number would appear only in $C_{D,\chi}^{cont}$. The drag coefficient in Eq. (6.2) is computed from the spherical case using the relations derived by Oberbeck [46], while the particle-based Knudsen number is defined as $Kn = \lambda/R_{eq}$, where λ is the mean free path of the gas defined via the definition of Phillips [42] introduced in Chapter 3 [Eq. (3.68)], and R_{eq} is the radius of the sphere with equivalent volume. In Chapter 5 we showed that this definition of Kn captures rarefaction effects on ellipsoidal particles unambiguously, and we proposed the following form for the model functions:

$$g_{\chi}(Kn) = f(Kn) + \frac{a_{\chi}}{b_{\chi} + c_{\chi}Kn}, \tag{6.3}$$

where a_{χ}, b_{χ} and c_{χ} are free parameters determined through a fit of data from DSMC simulations, and $f(Kn)$ represents the rarefaction correction to the Stokes drag force for a spherical particle as proposed by Phillips [42] and given by

$$f(Kn) = \frac{15 - 3c_1 Kn + c_2(8+\pi\sigma)(c_1^2+2)Kn^2}{15 + 12c_1 Kn + 9(c_1^2+1)Kn^2 + 18c_2(c_1^2+2)Kn^3}, \tag{6.4}$$

with $c_1 = \frac{2-\sigma}{\sigma}$, $c_2 = \frac{1}{2-\sigma}$. It can be seen that Eq. (6.4) recovers the continuum limit for vanishing Kn as

$$\lim_{Kn\to 0} f(Kn) = 1. \tag{6.5}$$

While this model is able to predict with good accuracy the effects of rarefaction in the transition and free-molecular regime of ellipsoidal particles, it is limited to a single aspect ratio ($a/b = 2$), to fully diffuse reflection ($\sigma = 1$), and it does not properly recover the asymptotic limit for the continuum regime.

In this Section we propose an improved model to address the aforementioned aspects, starting from the recovery of the correct asymptotic continuum limit. The new functional form for the model functions is given by:

$$g_{\chi}(Kn) = f(Kn) + \frac{p_{\chi}Kn}{q_{\chi} + r_{\chi}Kn^{s_{\chi}}}, \tag{6.6}$$

where p_χ, q_χ, r_χ and s_χ, with $\chi = 0°$ or $90°$, are the new free parameters to be determined separately for $C_{D,0°}$ and $C_{D,90°}$ and for each different shape of the particle. The free parameter s_χ is set to be strictly larger than unity, so that

$$\lim_{Kn \to 0} g_\chi = 1, \tag{6.7}$$

$$\lim_{Kn \to +\infty} g_\chi = 0, \tag{6.8}$$

allowing to correctly recover the continuum and free molecular limits also for the ellipsoidal case.

To obtain the free parameters in Eq. (6.6), we perform collisional DSMC simulations of different ellipsoidal particles immersed in a uniform argon gas flow with ambient velocity U_0, varying Kn and orientation Φ, following a similar procedure as described in in Chapter 5 (a sketch of the simulation setup is presented in Fig. 6.1). To obtain the drag coefficient from DSMC simulations we used the same approach as [48] so that $C_D = \mathbf{F}_D/(0.5 A \rho U_0^2)$, where $\mathbf{F}_D$ is the drag force as measured from DSMC simulations and A is the equivalent sphere cross-sectional area. We will focus on the drag coefficient since in Chapter 5 we showed that it knowing the drag coefficient is sufficient to fully determine also the lift coefficient. A discussion about the lift coefficient and the pitching torque is presented in Appendix A.

The volume of the equivalent sphere is fixed to $V = 6.5 \times 10^{-20}\text{m}^3$, corresponding to $R_{eq} = 2.5\mu\text{m}$. The aspect ratio of the particles is initially set to $a/b = 2$, leading to a major radius $a = 0.39\mu\text{m}$ for the prolate case and $a = 0.315\mu\text{m}$ for the oblate case (later in the paper the aspect ratio will be varied to $a/b = 4, 8$ and 10). The physical simulation box size is set to $L = 20a$, which has been shown in Chapter 5 to be sufficient to limit eventual effects induced by the finite size of the simulation box. In terms of DSMC cell units, for all cases with $Kn \geq 2$ a grid resolution of 120 cells per linear direction is sufficient to ensure high accuracy accordingly to the DSMC rules of thumb [33, 123] (i.e. $C_{size} \leq 0.3\lambda$, where C_{size} is the size of a single DSMC grid cell). For simulations at $Kn = 1, 0.5$ and 0.2 the number of cells is increased to $144, 288$ and 640, respectively. The simulation time step is defined accordingly to [33, 123] as $dt = 0.2 C_{size}/(v_{mp} + U_0)$, where $v_{mp} = \sqrt{2 k_B T/m}$ is the most probable speed of gas molecules.

The number of computational particles-per-cell (PPC) is always set to be larger than 25, again in accordance with [33, 123]. The Reynolds number is fixed to $Re = 0.1$, so that the ambient flow, U_0, the gas density, ρ, and the pressure are obtained from the values of Kn and $Re = \rho 2 U_0 R/\mu$, where $\mu = 2.12 \times 10^{-5}$ kg m^{-1}s^{-1} is the dynamic viscosity of the gas. The temperature of both gas and particle is set to $T = 300K$, and the latter is kept fixed to this value (isothermal assumption). The overall range of Kn investigated in this work is given by $0.2 \leq Kn \leq 20$, but, as it will be explained later, only the range $2 \leq Kn \leq 10$ is used to derive the model.

The TMAC is initially kept constant with $\sigma = 1$ (fully diffuse reflections) and later it will be varied in the whole range $0 \leq \sigma \leq 1$. For the rest of the paper, we will refer to TMAC with the single parameter σ. The error bars on the measured drag are calculated using the 95% confidence interval defined as $\varepsilon_{95} = 2s/\sqrt{N_{\Delta t}}$, where s is the standard deviation on the average value of the drag force from DSMC simulations, F_D, and $N_{\Delta t}$ is the number of samples, which is set to $N_{\Delta t} = 10000$ for $Kn \geq 0.5$, $N_{\Delta t} = 50000$ otherwise. Sampling of the drag force starts after the first 5000 time steps, which is enough to reach the steady state in all investigated cases. As already discussed in Chapter 5, with this setup highly accurate DSMC simulations are achieved. In order to separate derivation and validation of the presented heuristic model, the available DSMC data is divided in two sets: $Kn_{fit} = 2, 5, 8, 10$, which is used as data points for the fit, and $Kn_{test} = 0.2, 0.5, 1, 3, 7, 20$ which is instead used to validate the model.

We derive the fit parameters using the same procedure discussed in Chapter 5 for the cases of a prolate and oblate ellipsoid with $a/b = 2$, showing that the new model correctly predicts C_D while recovering the asymptotic continuum limit. Results, limited to the prolate case, are presented in Fig. 6.2..

It is important to mention that while this derivation shows robust performances in predicting rarefaction corrections to the drag experienced by ellipsoidal particles down to values of $Kn = 0.5$, it is not expected to be accurate for the slip-flow regime ($Kn \lesssim 0.1$) as the Kn_{fit} set is limited to the transition and free-molecular regimes. The loss of accuracy of the model for low values of Knudsen can be observed in Fig. 6.2, where the model predictions start to deviate from DSMC test data at $Kn = 0.2$. In order to improve the model in the slip-flow regime, more fitting data should be provided, either numerically or experimentally and currently our model should be used only for $Kn > 0.2$. Additionally, the case at $Kn = 0.2$ represents the limits of DSMC capability due to the large domain size and low ambient velocity, as it can be seen from the larger error bars when compared to other cases in Fig. 6.2 ($\varepsilon_{95} = 17.8$ for $Kn = 0.2$, while it already drops to $\varepsilon_{95} = 1.8$ for $Kn = 1$). The main aim of this specific case is to provide an indication of DSMC results in the low-Kn range to compare with the prediction of our model, obtained as an extreme extrapolation with respect to the fitting range ($2 \leq Kn_{fit} \leq 10$).

Another relevant aspect is related to the predictive capability of the present approach in relation to changes of the Mach and Reynolds numbers. The Mach number, Ma, can be related to the Reynolds and Knudsen numbers via the relation $Ma = \sqrt{\frac{\gamma\pi}{2}}\frac{ReKn}{2} = 0.617\frac{ReKn}{2}$, where γ is the ratio of specific heats and its value

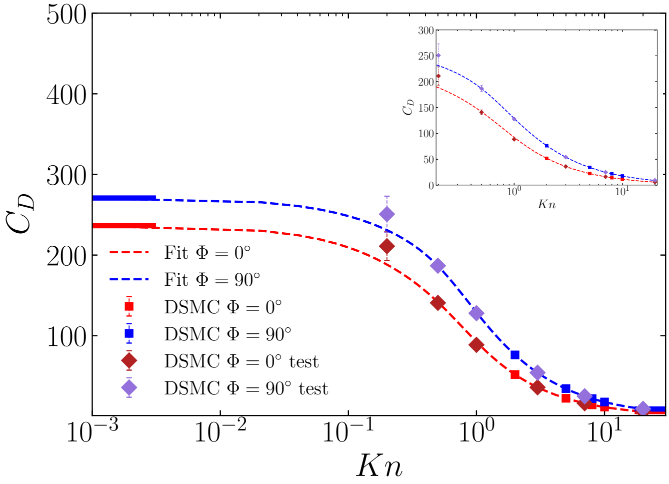

Figure 6.2: Fit of DSMC simulation data (squares) of $C_{D,0°}$ (red) and $C_{D,90°}$ (blue) using the functions in Eqs. (6.2) and (6.6), for a prolate ellipsoid with aspect ratio $a/b = 2$ and a fully diffusive surface ($\sigma = 1$). The predictive models (dashed lines) correctly captures data from Kn_{test} set (diamonds) down to $Kn = 0.5$, while they start to deviate at $Kn = 0.2$ (approaching slip-flow regime). The continuum and free molecular limits (horizontal solid lines) are correctly reproduced by the models. The former is obtained from the spherical case using the relations derived by Oberbeck [46], while the latter is calculated from [75] for fixed $Kn = 100$. The inset plot shows a zoom on the DSMC data and asymptotic limits are omitted. Error bars are calculated from ε_{95}.

is approximately 1.67 for argon at $300K$. The additional factor 2 at the denominator originates from the use of different characteristic length scales for Re and Kn ($2R_{eq}$ and R_{eq}, respectively).

In the proposed investigation the Mach number ranges globally from $0.006 \leq Ma \leq 0.617$, while the model is derived on values of Mach ranging from $0.03 \leq Ma \leq 0.3$, which is the typical range for low subsonic flows. For what concerns the Reynolds number, when dealing with micro- and nano-metric particles the Reynolds number is practically always smaller than unity, which is the reason behind the choice to focus on creeping flow conditions ($Re < 1$). Creeping flow condition is, in fact, a requirement for C_D^{cont} in Eq. (6.2) as it allows to use Oberbeck relations [46], to express the drag coefficients of ellipsoidal particles from the sphere with equivalent volume. As long as creeping flow is preserved, the specific choice of Re only impacts the value of the ambient velocity U_0 without any direct effect on the accuracy of our model predictions, as it will be shown later in this Section.

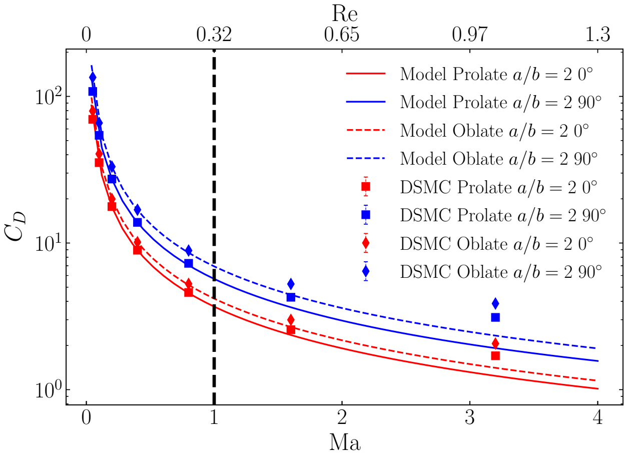

Figure 6.3: Comparison of drag coefficient, C_D, obtained from DSMC simulations of drag on a prolate (squares) and oblate (diamonds) ellipsoidal particles with aspect ratio $a/b = 2$ and model predictions from Eq. (6.2) (solid and dashed lines) at fixed $Kn = 10$ for varying Mach number (and therefore Re). We limit the comparison to the cases with $\Phi = 0°$ (red) and $\Phi = 90°$ (blue) as intermediate value can be obtained by applying the sine-squared drag law from Eq. (6.1). Model predictions are in excellent agreement with DSMC data up to $Ma \sim 1$ (black dashed line, corresponding to $Re = 0.32$), after which they start to deviate as compressibility effects are not included in the calculation of C_D^{cont} from Eq. (6.2). Error bars are calculated from ε_{95} and are typically smaller than symbols sizes.

To verify the validity of the model for varying Re and Ma we perform DSMC simulations at fixed $Kn = 10$ and compare the results of the model predictions for a prolate and oblate ellipsoidal particle with aspect ratio $a/b = 2$. From the results, presented in Fig. 6.3 it can be observed that the model predictions show excellent match with DSMC data up to large values of Ma, and start to show appreciable deviation only for $Ma \gtrsim 1.6$. This allows us to be confident on the applicability of the model up to $Ma \sim 1$ and $Re \lesssim 1$, which correspond to the typical ranges of interest for Euler-Lagrangian simulations of submicron particles transport in a variety of high-tech mechanical systems.

In this context it is important to keep into consideration that our DSMC simulations are based on an isothermal approximation of the particle surface, which is kept at the same constant temperature of the equilibrium gas ($300K$ in this case). Such approximation neglects local temperature variation due to gas-surface interaction around the particle, introducing an error on the temperature of the reflected gas molecules (which will be the same as the surface temperature). While this approach is valid for

subsonic flows ($Ma \leq 0.3$), where temperature variation are typically within 1% of the equilibrium value, this might be not true for high-Mach flows. When compressibility effects start to play a role, a relevant flow temperature variation can be observed around the solid particle (especially at the stagnation points), and such effects should be considered in the energy of the reflected gas molecules. Since in this work we are mostly focused in contamination control in lithography machines, which are typically subsonic isothermal problems, the aforementioned approximation is not affecting the quality of the results. When considering space applications, where high-Mach flows are common, we suggest to improve the model to account for local thermal effects.
Another potential limitation is that our simulations only employ argon gas. Using a different gas in principle will only impact the gas viscosity (given by Eq. (3.69 in Chapter 3)), which will lead to different derived quantities such as λ and Re. We expect that the rarefaction corrections derived in this work will not be affected by a modification of the suspending gas, but this assumption must be verified in future studies.
The presented procedure to derive the predictive models can be efficiently extended to particles with larger aspect ratio, approximating more complex shapes such as needles (for the prolate case) and flakes (for the oblate case), which are representative shapes for many high-tech mechanical systems applications. This aspect highlights that the perturbative approach employed to derive the model functions from Eq. (6.6) is not limiting the applicability of such method, even when the shape of the particle under investigation largely deviates from the spherical case.
By repeating the procedure explained for the case with aspect ratio $a/b = 2$, we obtain the free parameters $p_\chi,\ q_\chi,\ r_\chi$ and s_χ, with $\chi = 0°$ and $90°$, for the cases with $a/b = 4,\ a/b = 8$ and $a/b = 10$. This is, again, done by fitting the corresponding data from DSMC simulations related to the Kn_{fit} set. In Fig. 6.4 we show the model functions, as well as their testing by direct comparison with DSMC results from the Kn_{test} set, which have not been used during the fitting process. We focus on the cases at 0° and 90°, since it has been shown in [152] that it is sufficient to predict the drag force at such orientations to be able to extend the prediction to any arbitrary vale of Φ. Due to the large number of costly DSMC simulations required for this study, and considering that we are mostly interested in applications at $Kn \geq 1$, the test set is limited to $Kn_{test} = 1, 3, 7, 20$ for the following validations. The results shown in Fig. 6.4 clearly indicate that our model functions work properly for all aspect ratios considered.

In the last part of this Section we will extend our results, so far limited to fully diffusive reflections at the surface of the solid particles, to include σ effects. For nanometric particles, in fact, it is known [1] that an increasingly larger fraction of gas molecules undergoes specular reflection when hitting the surface of the solid particle,

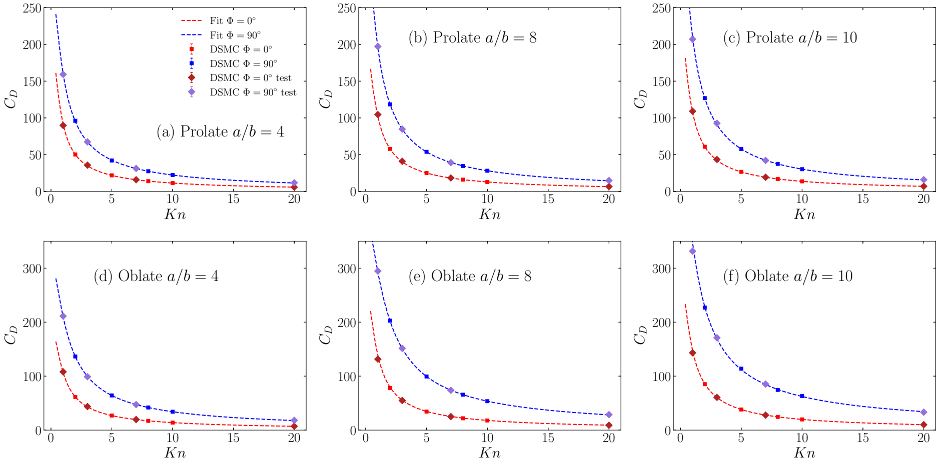

Figure 6.4: Fit of DSMC simulation data of $C_{D,0^\circ}$ (red) and $C_{D,90^\circ}$ (blue) using Eqs. (6.2) and (6.6), for prolate ellipsoids (top row) and oblate ellipsoids (bottom row) with same volume and $a/b = 4$ (a,d), $a/b = 8$ (b,e) and $a/b = 10$ (c,f). Fitted curves (dashed lines) represent the model functions given by Eq. (6.6) and using Eq. (6.2). The prediction from the derived models is compared with data from DSMC simulations that is not used during the fitting process (colored diamonds), showing an excellent match. As shown in Chapter 5, it is sufficient to know the scaling of the drag force at $\Phi = 0°$ and $\Phi = 90°$ to derive its value at any arbitrary orientation. Legend is shown only for (a) as symbols refer to same quantities in all plots.

and it is important to capture such effects to correctly model particle transport in contamination control applications. In this work we decide to adopt a diffuse/specular molecular scattering governed by the single parameter σ rather than the more complex Cercignani-Lampis-Lord (CLL) model [52], which instead describes the molecular scattering via multiple momentum accommodation coefficients (namely, tangential, normal and additional energy accommodation coefficients). The reason behind this choice resides in the fact that the latter formulation, albeit considered more accurate [179, 180], is often difficult or unpractical to connect with typical industrial experiments which are designed (or limited) to capture a single-parameter accommodation, such as σ used in this work. Since we are targeting engineering applications, for which TMAC is typically employed, we will restrict our derivation to the aforementioned diffuse/specular scattering model (in which energy and tangential momentum accommodation are the same and both defined by σ).

We show that by adding an extra term to the model Eq. (6.6) we can successfully include effects of a varying σ in the prediction of the drag coefficient. The modified model functions are defined as:

$$g'_\chi(Kn, \sigma) = g_\chi(Kn) + \frac{\alpha_\chi Kn}{\beta_\chi + \gamma_\chi Kn^{\delta_\chi}}(1 - \sigma), \tag{6.9}$$

where an extra term containing the σ-dependence is included in the previously defined model functions (represented by the first term in the right end side). This new term is used to model the corrections to the drag given by the presence of a combination of specular and diffuse reflection at the solid interface, with $0 \leq \sigma \leq 1$, and it is designed to vanish for $\sigma = 1$, recovering $g_\chi(Kn)$. It is worth mentioning that Eq. (6.9) is an heuristic model and it is aimed to simplify the physics behind σ effects on drag corrections (which are known to be analytically more complex, see e.g. [33, 75, 181]), while capturing their overall impact.

The extra free parameters α_χ, β_χ, γ_χ and δ_χ are to be determined through a 2D fit in the independent variables Kn and σ, where again χ refers to the two cases at $\Phi = 0^\circ$ or $Phi = 90^\circ$, separately. The results from the fit for the case of a prolate ellipsoid with $a/b = 2$ are presented in Fig. 6.5.

We repeat the fitting procedure for different aspect ratios and values of σ. The testing is performed on values of Kn and σ that were not used during the fitting process, to evaluate the predictive capability of the model obtained with this procedure. The results of the testing are presented in Fig. 6.6, where it can be observed that the predictive model is able to recover DSMC data with fairly good accuracy for all investigated cases. The final fit coefficients derived in this Section are reported in Table 6.1.

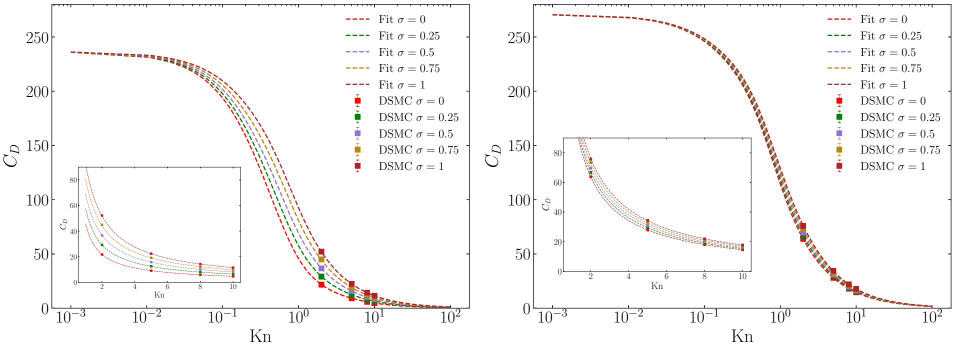

Figure 6.5: Fit of DSMC simulation data (squares) of $C_{D,0^\circ}$ (left) and $C_{D,90^\circ}$ (right) using Eqs. (6.2) and (6.9) (dashed lines) for a prolate ellipsoidal particle with aspect ratio $a/b = 2$. The model functions are derived through the fit of DSMC data using σ_{fit} and Kn_{fit}. In the insets, an enlargement on the Kn_{fit} range is presented.

Prolate $\Phi = 0^\circ$									
a/b	$C_{D,cont}$	p	q	r	s	α	β	γ	δ
2	236	-0.378	1.26	4.30	1.90	0.299	0.436	1.08	1.98
4	249	-0.175	0.708	1.26	1.99	0.423	0.255	1.26	1.95
8	286	-0.134	0.146	1.42	1.90	0.422	0.328	1.04	1.98
10	304	-0.160	0.284	1.26	1.94	0.421	0.296	1.04	1.97

Prolate $\Phi = 90^\circ$									
a/b	$C_{D,cont}$	p	q	r	s	α	β	γ	δ
2	270	0.094	3.90	1.52	1.99	0.151	1.73	1.16	2.04
4	320	0.110	1.34	1.38	1.90	0.115	1.99	0.753	2.22
8	402	0.064	1.40	0.695	1.94	0.115	1.98	1.25	2.04
10	437	0.053	1.53	0.634	1.92	0.089	0.990	1.24	1.93

Oblate$\Phi = 0^\circ$									
a/b	$C_{D,cont}$	p	q	r	s	α	β	γ	δ
2	247	-0.118	1.84	2.29	1.88	0.308	0.267	1.29	1.99
4	267	-0.082	0.094	1.30	1.92	0.425	0.444	1.28	1.96
8	309	0.010	1.01	1.99	2.10	0.553	0.327	1.15	1.96
10	326	0.025	1.97	0.207	2.01	0.502	0.327	1.01	1.96

Oblate $\Phi = 90^\circ$									
a/b	$C_{D,cont}$	p	q	r	s	α	β	γ	δ
2	282	0.307	3.01	1.76	2.00	0.040	1.99	0.336	2.52
4	340	0.398	1.31	1.18	1.91	-0.044	1.00	1.36	1.71
8	422	0.603	1.46	1.11	1.90	-0.092	1.22	1.24	1.74
10	454	0.577	0.738	1.17	1.80	-0.056	2.00	0.150	2.39

Table 6.1: Fit parameters obtained using Eq. (6.2) to fit $C_{D,0^\circ}$ and $C_{D,90^\circ}$ as obtained from DSMC simulations performed at Kn_{fit} for all cases investigated in this work. The parameters p, q, r, s are used to define the function $g_\chi(Kn)$ given by Eq. (6.6), while the parameters $\alpha, \beta, \gamma, \delta$ are used to define the function $g'_\chi(Kn)$ given by Eq. (6.9). Additionally, the drag coefficients in the continuum regime $C_{D,cont}$, computed from [46] and used as reference, are presented.

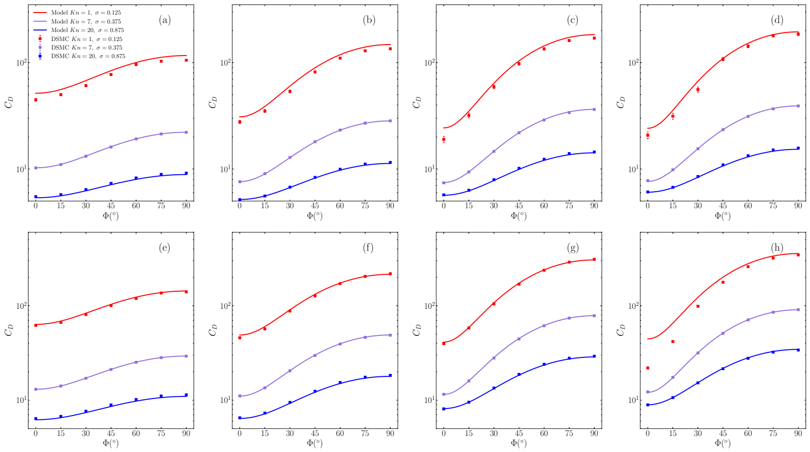

Figure 6.6: Comparison between DSMC simulations (squares) and model predictions (solid lines) of the drag coefficient C_D of a prolate (a, b, c, d) and an oblate (e, f, g, h) ellipsoid, for $a/b = 2$ (a,e), $a/b = 4$ (b, f), $a/b = 8$ (c, g) and $a/b = 10$ (d, h). Every set of test has been performed with different values of Kn and σ that were not used during the fitting process. The match between the model predictions and DSMC data is excellent for most cases, except for the oblate case at $a/b = 10$ and $\sigma = 0.125$. The legend is shown only for (a) as all the symbols refer to the same quantities in all plots.

6.3 Drag corrections from near-wall effects

The approach discussed in Section 6.2 is formally valid only for the case of a particle immersed in a uniform unbounded flow. In many practical situations, however, the particles transported in the flow will interact with other elements of the flow domain, such as walls or other obstacles and it is important to understand the limitations in the applicability of the methods proposed in this work when particles are located in proximity of a wall. The aim of this Section is to demonstrate that the drag corrections derived in Section 6.2 can adopted also in non-ideal situations where the unbounded flow condition is no longer valid, provided that the particle-based Kn is large and that the particle size is much smaller than the typical size of the system in order to maintain the Point-Particle approximation.

We tackle the problem by evaluating the impact of the presence of a wall on the drag experienced by an ellipsoidal particle translating parallel to it. This condition is easily achievable by performing simulations in the reference frame of the particle, so that it is sufficient to modify the setup discussed in Section 6.2 by adding solid walls on the direction orthogonal to $\hat{y}$ moving with the same ambient velocity of the flow (see Figs. 6.8 and 6.7). In this way the problem is analogous to the one of a particle translating

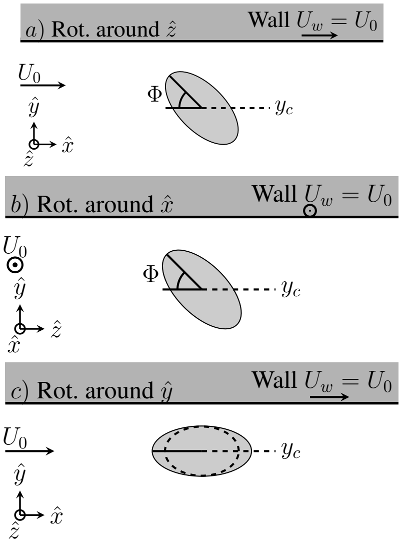

Figure 6.7: Sketch of the simulation setup: a prolate ellipsoidal particle with aspect ratio $a/b = 2$ is immersed in a uniform flow with ambient velocity U_0. The center of the particle, y_c, is located in proximity to a solid, fully diffusive ($\sigma = 1$) wall translating at a velocity $U_w = U_0$. In this way the problem is analogous at the one of a particle translating with uniform velocity $-U_0$ parallel to the wall. We investigate orientation effects with respect to rotations around the three main Cartesian axes $\hat{z}$ (a), $\hat{x}$ (b) and $\hat{y}$ (c), for different values of y_c (for simplicity, the rotation angle is always labeled as Φ). Note that in case (b) the major radius a is always orthogonal to the flow direction. Free stream and periodic boundary conditions are applied on the directions orthogonal to $\hat{x}$ and $\hat{z}$, respectively.

with a velocity $-U_0$ parallel to the wall. All the simulations are performed with the same criteria discussed in Section 6.2, with the exception that now the particle center is located close to the upper edge of the simulation box, at which a solid moving wall condition is applied.

To validate the simulation setup, we compute the drag acting on a sphere translating parallel to the wall in the collisionless regime and compare with the results from Godwami *et al.* [182]. The comparison is shown in Fig. 6.8, where it can be seen that the drag acting on the spherical particle measured from our DSMC simulations correctly reproduces the analytical expression obtained in [182].

We now proceed in investigating the effects on the drag force experienced by an ellipsoidal particle translating in the vicinity of a wall. Due to the large number of parameters, we will restrict our study to a prolate ellipsoid with aspect ratio $a/b = 2$ and by assuming that all the solid surfaces (i.e. both wall and particles) are fully

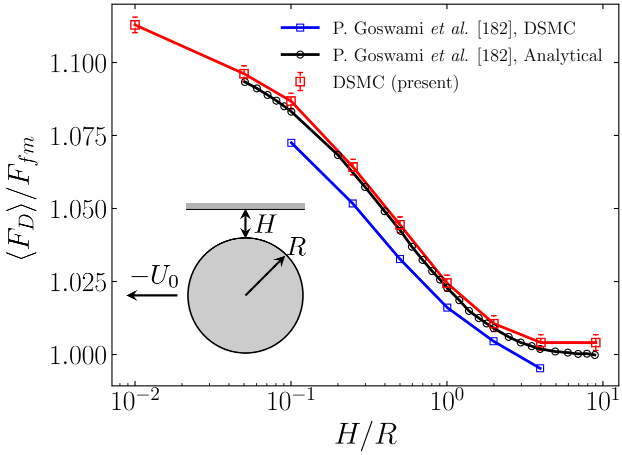

Figure 6.8: Drag force experienced by a spherical particle with radius $R = 0.25\mu$m translating with uniform velocity $-U_0$ parallel to a wall, for different values of the distance from the wall expressed by H/R. Results from DSMC simulations (red) are compared with the analytical results obtained from Goswami *et al.* [182] and their DSMC method (blue). All solid surfaces are considered fully diffusive ($\sigma = 1$).

diffusive ($\sigma = 1$). The focus on the prolate case limits our claims to this specific geometry, however we expect similar results for the oblate case and for the other aspect ratios.

In our first analysis, we perform simulations varying the orientation and the distance of the particle from the top wall of the simulation box, addressing separately three different cases of rotation around the x, y and z axes. Due to the presence of the wall, in fact, the symmetry of the system is no longer conserved and rotations around different axes are expected to produce different results. For the sake of simplicity, we focus on the rotations around the three main Cartesian axes, where for the case of rotation around the x axis the ellipsoidal particle major axis is orthogonal to the flow direction (constant angle of attack). A sketch of the simulation setup is presented in Fig. 6.7.

In Fig. 6.9 we compare the drag force experienced by the particle, at fixed $Kn = 10$, for different orientations and different vertical locations of the particle (i.e. different distances from the wall). The drag force is normalized with respect to the drag force relative to the unbounded case to emphasize the effects introduced by the wall, while the vertical position of the center of the particle, y_c, is normalized with respect to the simulation box size, L. The largest value of y_c/L is chosen so that the particle is in contact with the wall at $\Phi = 90°$ (with the exception of case (c), where y_c is chosen

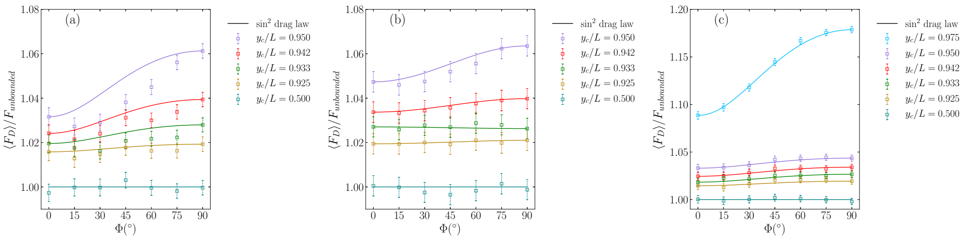

Figure 6.9: Drag force experienced by an ellipsoidal particle with aspect ratio $a/b = 2$ translating with uniform velocity parallel to a wall at fixed $Kn = 10$, for different vertical locations y_c/L, where y_c is the vertical coordinate of the center of the particle and L is the dimension of the simulation domain. The drag force is evaluated at different orientations Φ with respect to the ambient flow, for rotations around the $\hat{z}$ axis (a), $\hat{x}$ axis (b) and $\hat{y}$ axis (c). Results from DSMC simulations (squares) are compared with the sine-squared drag law (solid lines) from Eq. (6.1) calculated using values from DSMC simulations at $\Phi = 0°$ and $\Phi = 90°$. It is possible to observe that Eq. (6.1) still captures the general scaling of the drag force, with the exception of case (a) and particle in close contact with the wall for which a larger deviation is evident. The error bars in this plot are obtained via ε_{95} and considering the error propagation related to the drag force ratio.

so that the particle is in contact for all values of Φ).

A deviation from the unbounded case (horizontal line in Fig. 6.9) is evident, as drag experienced by the particle increases the closer its surface gets to the wall. We observe that this drag-increase effect depends, as expected, not only to the vertical position, but also to the rotation angle Φ for cases (a) and (b), since for larger values of Φ the surface of the particle is closer to the solid wall, while for case (c) the orientation only impacts on the squeezing of the flow between the particle and the wall. Interestingly, we also observe that the general sine-squared scaling is maintained if the drag force evaluated at $\Phi = 0°$ and $\Phi = 90°$ are used in Eq. (6.1), and the largest variations from it appear in case (a) for particle in close contact with the wall . The drag increase induced by the plane wall quickly vanishes as the particle moves away from it, to the point that for $y_c/L = 0.925$ (which corresponds to a wall distance equivalent to the particle major radius, a) such effects are already lower than 2%.

In the last analysis of this work, we compare the drag force experienced by the near-wall particle for three values of Kn, i.e. $Kn = 10$ (free molecular regime), $Kn = 2$ and $Kn = 1$ (transitional regime). The vertical position of the particle, y_c/L, is chosen so that the particle is in contact with the wall at $\Phi = 90°$ for the cases of rotation around the $\hat{z}$ (a) and $\hat{x}$ (b) axes , while it is always in contact for the case of rotation around the $\hat{y}$ axis (c). To better resolve the physics in the gap between the particle and the solid wall and improve the signal-to-noise of DSMC simulations, we

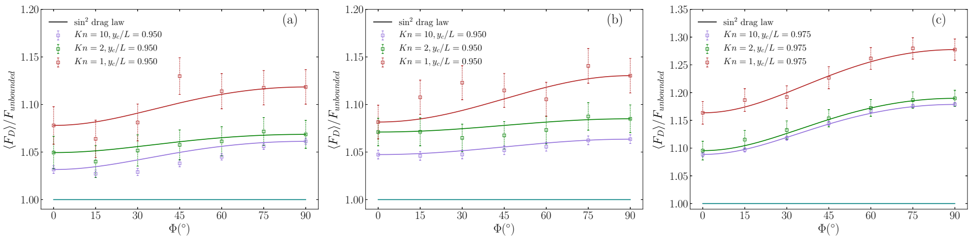

Figure 6.10: Drag force experienced by an ellipsoidal particle with aspect ratio $a/b = 2$ translating with uniform velocity parallel to a wall for $Kn = 10$ (purple), $Kn = 2$ (green) and $Kn = 1$ (red). The drag force, normalized with respect to the unbounded case, is evaluated at different orientations Φ with respect to the ambient flow, for rotations around the $\hat{z}$ axis (a), $\hat{x}$ axis (b) and $\hat{y}$ axis (c), while the vertical position y_c/L is fixed so that the particle has one point of contact with the wall for $\Phi = 90°$ in cases (a) and (b)($y_c/L = 0.95$), and is always on contact for case (c) ($y_c/L = 0.975$). Results from DSMC simulations (squares) are compared with the sine-squared drag law (solid lines) from Eq. (6.1) calculated using values from DSMC simulations at $\Phi = 0°$ and $\Phi = 90°$.

increased the resolution for $Kn < 10$. For the case with $Kn = 2$ it was sufficient to increase the PPC number to 150, while for the case with $Kn = 1$ we also increase the spatial resolution. In the latter case we set a linear domain size of 256 grid cells, leading to a particle major radius $a = 12.7$ (in cell units); the PPC number is set to 100.

As it can be seen from the results in Fig. 6.10, the drag increase, with respect to the unbounded case, exhibits a weak dependence on the Knudsen number, especially when $Kn > 1$. In the worst case scenario ($\Phi = 90°$ and rotation around $\hat{z}$ axis), the deviation with respect to the unbounded case is about 27% for the case at $Kn = 1$ and it quickly drops to 19% for the case at $Kn = 2$; after this, it remains roughly constant up to $Kn = 10$, where we measure an increase of about 18%. Near-wall effects appear, thus, to be weak enough to be considered negligible for the vast majority of applications involving the transport of micro- and nano-metrical ellipsoidal particles in highly rarefied regimes, as the average residence time of particles in areas very close to the wall (on the order of the particle characteristic size) is typically very limited, allowing the drag corrections of Section 6.2 to be applied without introducing large errors also in bounded flow situations.

6.4 Concluding remarks

We propose a new formulation and derivation of heuristic predictive models for the drag coefficients of prolate and oblate ellipsoidal particles under rarefied conditions in a range of particle-based Kn that includes the transition and the free-molecular regimes. The predictive models are based on a perturbative approach, where rarefaction effects on ellipsoidal particles are represented as perturbation with respect to the spherical case and such perturbations are obtained through a fit of DSMC simulation data.

We firstly show that the new models are designed to recover the free-molecular and continuum asymptotic limits, potentially providing a valid baseline to improve the fitting procedure and extend the model to the whole range of Knudsen. We then obtain predictive models for a wide range of particle aspect ratios (including complex shapes such as needles and flakes), and TMAC effects. For nano-metric particles, in fact, a larger fraction of specular reflection can occur at the gas-particle interface and it is important to correctly capture these effects to obtain accurate predictions. The models obtained with this procedure show robust performances in reproducing DSMC data, also outside of the range of Kn used for the fitting procedure.

The results from this Chapter, albeit currently focused for isothermal problems, can be used to further improve the available models of particle transport in rarefied gas flows. Using the derived predictive models it is now possible, in fact, to include the full dynamics of prolate and oblate particles under the influence of the local fluid velocity field in Euler-Lagrangian simulations typically employed for different modern applications, such as contamination control in high-tech mechanical systems and, potentially, in aerospace engineering. In relation to aerospace applications, the predictive models derived in this work show robust capability in reproducing the drag experienced by particles also when compressibility effects are present, so that the proposed method to derive such models can be regarded as a valid way of working for further developments (such as the inclusion of local temperature variations on the particle surface) to extend their applicability range.

In the last part of this Chapter we show that the aforementioned models, formally derived for the case of unbounded flow, can be applied also in cases where the unbounded condition is not strictly preserved. We do so by investigating the effects induced on the drag experienced by the particles by the presence of a wall, showing that while near-wall effects increase the drag force, this effects is rather limited for large Knudsen number, and it quickly decays as the particle moves away from the wall. For the worst case scenario of a particle in contact with the wall, we measured a maximum drag increase of roughly 27% at $Kn = 1$, and such increase sharply decrease to 19% at $Kn = 2$, while for a larger value of $Kn = 10$, the maximum increase is observed to be about 18%. Considering the rapid decay of drag-increase effects due to wall proximity, such effects can be considered negligible in the high-Knudsen range typical of the aforementioned applications as the particle residence time in the near proximity of walls is on average limited.

6.5 Appendix A

In this Appendix we will discuss the torque on the simulated particles as measured from our DSMC simulations and the applicability the predictive model derived in this work to the lift coefficient. For Stokes flows, the torque should vanish identically [44]. Due to the finite Reynolds number of our simulations($Re = 0.1$) we measure a torque of the order of $\sim 10^{-17}$, which is about 8 orders of magnitude smaller than the typical drag force signal ($\sim 10^{-9}$) and 7 orders of magnitude smaller than the typical lift force signal ($\sim 10^{-10}$). In Fig. 6.11 we present a comparison of the drag force, lift force and torque (along $\hat{z}$) as a function of the angle of attach Φ for a prolate ellipsoid with different aspect ratios, for the test case with $Kn = 7$ and $\sigma = 0.375$ (similar conclusions are valid for the other cases). As it can be seen from the figure, while it is possible to observe a parabolic profile of the torque profile that resembles the $\sim \sin\Phi\cos\Phi$ scaling discussed in [183, 184], the torque signal from our simulations is too small to be properly resolved and it can be considered as indistinguishable from noise around a zero-value. For this reason torque effects can be considered negligible in the scope of this work.

In relation to the lift coefficient, in [152] we showed that it is possible to predict the lift coefficient, C_L, of an arbitrary shape particle from the sine-squared drag law by just knowing $C_{D,0^\circ}$ and $C_{D,90^\circ}$. The sine-squared drag law for the lift coefficient reads:

$$C_L(\Phi) = (C_{D,0^\circ} - C_{D,90^\circ}) \sin\Phi\cos\Phi. \tag{6.10}$$

In Fig. 6.12 we repeat the validation proposed in Fig. 6.6 focusing this time on comparing C_L from our DSMC simulations with Eq. (6.10), where $C_{D,0^\circ}$ and $C_{D,90^\circ}$ are obtained from our predictive model. The lift coefficient is defined as: $C_L = \mathbf{F}_L/(0.5A\rho U_0^2)$, where $\mathbf{F}_L$ is the lift force as measured from DSMC simulations.

As it can be seen from Fig. 6.12, the match between DSMC simulations and our predictive model is excellent, with the exception of the prolate case at $Kn = 1$, $a/b = 2$ and $\sigma = 0.125$, in which the lift force signal was at the limit of the numerical resolution. The predictive model obtained in this work can, thus, be employed to also predict the lift coefficient for the investigated class of particles.

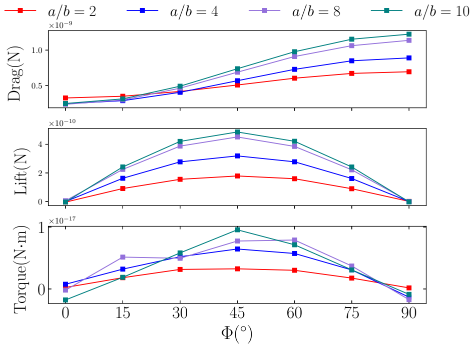

Figure 6.11: Comparison of drag force, lift force and torque along $\hat{z}$ acting on a prolate ellipsoid with different aspect ratios at fixed $Kn = 7$ and $\sigma = 0.375$.

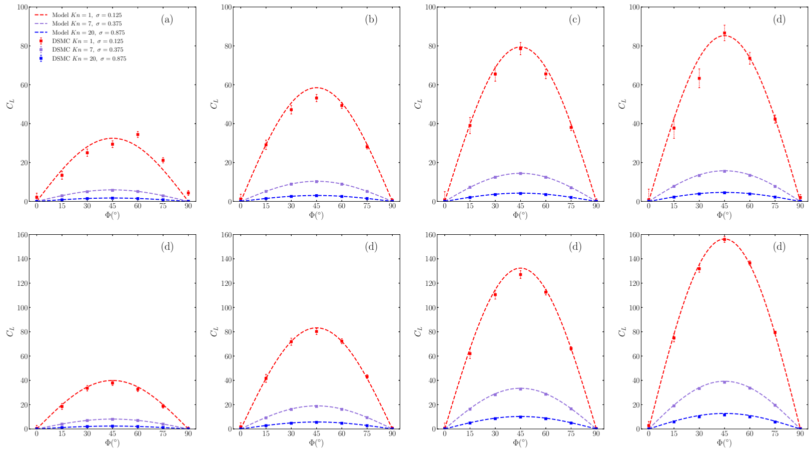

Figure 6.12: Comparison between DSMC simulations (squares) and model predictions (solid lines) of the lift coefficient C_L of a prolate (a, b, c, d) and an oblate (e, f, g, h) ellipsoid, for $a/b = 2$ (a,e), $a/b = 4$ (b, f), $a/b = 8$ (c, g) and $a/b = 10$ (d, h). Every set of tests has been performed with different values of Kn and σ that were not used during the fitting process. The match between the model predictions and DSMC data is excellent for most cases, except for the prolate case at $Kn = 1$, $a/b = 2$ and $\sigma = 0.125$, where the lift signal was small enough to be at the limit of the DSMC simulation accuracy. The legend is shown only for (a) as all the symbols refer to the same quantities in all plots.

Chapter 7

Concluding remarks and outlook

In the present thesis, we focused on the modelling of interactions between fully-resolved particles and gas flows in the framework of two kinetic solvers based on the numerical solution of the Boltzmann Equation, namely the Lattice-Boltzmann Method (LBM) and the Direct Simulation Monte Carlo (DSMC) method. The reason behind this choice, as stated in Chapter 1, is not only related to the predisposition of these numerical approaches to describe arbitrary shaped solid particles without complex re-meshing of the simulation domain, but also because they individually excel in modelling flows at different rarefaction levels. The LBM is, in fact, an efficient solver for continuum flows which can include multiphase, particle-laden flows, while the DSMC is the most reliable solver to capture rarefaction effects beyond the slip flow regime. Additionally, their common root to the discretized Boltzmann equation opens promising possibilities toward the development of a hybrid method that could, in principle, include the aforementioned individual features into a single framework, able to correctly and efficiently model flows ranging from the continuum to the free-molecular regimes. In this Chapter, we first summarize the main results obtained by applying the developed particle-transport algorithms in the LBM and DSMC to different scenarios involving the interactions between particles and flows. We then highlight possible outlooks from the presented work, such as the development of a hybrid LBM-DSMC method that embeds fully-resolved particle description, or the direct application of some of the results of this work to Euler-Lagrangian Point Particles simulations, which are typically employed in the high-tech industry to address contamination control.

7.1 Conclusions

In this thesis, we present a methodology to capture two-way coupled fluid-particle interactions based on the combination of a ray-tracing technique, to compute intersection points, and a double reference system approach, to compute momentum exchange, for the LBM and DSMC numerical schemes. We show that the two methods can, in fact, employ the same fundamental scheme to describe a fully-resolved solid particle coupled with the external flow, with only minor modifications mostly related to the different boundary treatments. In both methods, in fact, it is necessary to compute exact intersection points between impinging particles and the solid surface during the streaming step, and this can be done by applying the same ray-tracing solution. Once the intersection points are evaluated, then standard boundary conditions are applied in the reference frame centered on the particle origin and the total momentum transferred during collision is accumulated. By repeating this procedure for all the impinging molecules, the total force and torque on the particle can be computed and used to integrate its position, velocity and orientation, or simply used to perform aerodynamics studies. One of the main aspects of this implementation is related to the possibility to efficiently describe mesh-less particles with any shape that can be described analytically, without introducing any overhead on the computation arising from the necessity to re-mesh the simulation grid accordingly to the particle instantaneous location.

In Chapter 4, we then apply this approach to couple flow and particles in the LBM to accurately investigate the numerical accuracy offered by different boundary schemes applied at the fluid-solid interface in dynamic conditions. We do so by introducing a novel adaptive treatment of the simulation box boundaries, which allows to strongly suppress boundary effects due to the finite size of the simulation domain on the dynamics of spherical and ellipsoidal particles free to move in an unbounded fluid under Stokes flow conditions. We apply this technique to isolate the influence of particle resolution by performing fine measurements of the accuracy convergence of the particle dynamics in two specific conditions, i.e. the settling of a particle in unbounded flow and the rotation of an ellipsoidal particle in shear flow, down to very low resolutions. We firstly compare the accuracy between two widely used fluid-solid interaction models, namely Bounce-Back (BB) and Equilibrium Interpolation (EI), and then we propose a third model called Complete Equilibrium Interpolation (CEI), that allows to detect momentum exchange also between two fluid nodes, in the case in which the particle surface is occupying a position between the two. We show that CEI is not only able to detect particles as small as one lattice grid spacing, but also to provide higher accuracy in cases where the particle size is only a few lattice nodes.

In Chapter 5, we shift our focus on the DSMC method to perform aerodynamics studies on ellipsoidal particles immersed in uniform ambient flow under rarefied conditions. We propose a methodology to derive a heuristic model to predict the drag and lift coefficients for ellipsoidal particles in a range of Knudsen ($1 \leq Kn \leq 20$) that includes the transition and the free-molecular regimes. The heuristic model is obtained by the fitting of data from DSMC simulations and it shows robust performances in predicting drag and lift coefficients in the investigated range of Kn, as well as outside of the range of Kn used for its derivation.

In Chapter 6, we further develop this study first by improving the mathematical formulation behind the heuristic predictive model, which is now designed to recover the free-molecular and continuum asymptotic limits, potentially providing a valid baseline to improve the fitting procedure and extend the model to the whole range of Kn. We then apply the model to a wide range of particle aspect ratios, and momentum accommodation effects. In the last part of Chapter 6 we also show that the heuristic models, formally derived for the case of unbounded flow, can also be applied in cases where the particle is located in the vicinity of a solid wall. We do so by investigating the effects induced on the drag experienced by the particles by the presence of a wall, showing that while wall vicinity leads to a drag increase, such effects can, in general, be considered negligible for most cases of interest. As it will be shown in the Outlook Section, the results from this work can be used to further improve the available models of particle transport in rarefied gas flows, as the full dynamics of prolate or oblate particles under the influence of the local fluid velocity field can now be included in the aforementioned Euler-Lagrangian simulations typically employed for different modern applications, such as contamination control in high-tech mechanical systems or in aerospace engineering applications.
In relation to the research questions raised in the Introduction of this thesis work (Chapter 1), we can provide the following answers:

- **Mesh-free uniform approach for flow-particle interactions:** we successfully developed an approach to model fully-resolved particles in the framework of the LBM and DSMC. This approach can be employed to develop hybrid LBM-DSMC algorithms that include fully-resolved particle transport capabilities.

- **Investigate accuracy of LBM particle transport algorithms in dynamics conditions:** we propose solid benchmarks to assess the accuracy of particle dynamics in different conditions. Such benchmarks are based on a novel definition of boundary conditions applied at the simulation box that allows to mimic unbounded fluid behavior.

- **Improve Euler-Lagrangian Point Particles simulations of non-spherical particles in rarefied conditions:** we employ the numerical schemes developed in this work to derive heuristic models that allow to predict the drag force experienced by a large class of ellipsoidal particles as a function of rarefaction and their orientation with respect to the flow. These models can be directly used in Euler-Lagrangian Point Particles simulations to potentially include the full dynamics of prolate or oblate particles.

7.2 Outlook

The numerical techniques and results presented in this work may offer the basis for different applications, as well as for improvements and extensions. In the following of this Section, we will address some possible new directions.

Integrate fully-resolved particle transport in LBM-DSMC Hybrid scheme: The possibility to couple LBM and DSMC solvers to retain DSMC capabilities to capture rarefaction and non-equilibrium effects with the LBM numerical efficiency in the flow regions that are, instead, in near-continuum regime has been mentioned several times in the manuscript. Such hybrid model is mostly referring to the work by Di Staso [20, 31, 32], where it is shown how to efficiently couple these two numerical schemes on the same computational grid. The flow Knudsen number is used as the parameter to select which region of the domain must be assigned to each individual solver. The coupling is then performed via the use of buffer regions, where the probability distribution obtained from DSMC is converted into the discretized distribution used in the LBM. The numerical schemes proposed in this work to model two-way coupled interactions between flow and fully-resolved particles can, in principle, be included in the hybrid solver. This process may be facilitated by the similarities in the proposed methods in terms of its implementation in the framework of the LBM and DSMC. A schematic representation of the basic idea behind the implementation of such model for particle transport in the hybrid LBM-DSMC scheme is presented in Fig. 7.1. Similarly to what is already done for the standard hybrid method, regions of high Knudsen would be adaptively evaluated and assigned to DSMC, while the low Knudsen region will be assigned to LBM. If the solid particles are in the DSMC region, then the DSMC algorithm to compute momentum exchange between flow and particle is used, otherwise the LBM counterpart will be employed. Clearly, this is a simplistic view of a complex topic, and different difficulties may arise, such as modelling thermal components, different timescales between solvers, derivation of an efficient algorithm to dynamically assign flow regions to different solvers and many more questions that must be carefully considered.

Adaptive boundary treatment of simulation box to evaluate accuracy in different conditions: The method proposed in Chapter 4 to evaluate the accuracy of the dynamics of solid particles can be extended to more complex scenarios to accurately assess novel numerical schemes. This approach is based on the imposition on the simulation external boundaries of the Stokes flow solution, using parameters obtained from the motion of the particle itself. One example can be connected with the afore-

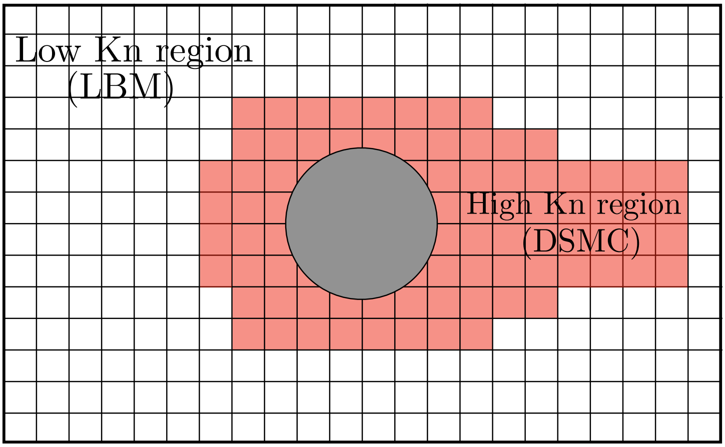

Figure 7.1: Sketch of hybrid LBM-DSMC numerical scheme including fully-resolved particle transport algorithm. Flow regions with high Knudsen number are assigned to DSMC, while regions in continuum or near-continuum conditions are assigned to the LBM. The two-way particle transport algorithm corresponding to the specific region the particle is occupying will be used to evaluate momentum exchange between flow and the solid particle.

mentioned LBM-DSMC hybrid scheme for particle transport: the settling of a particle in rarefied condition can be addressed using the hybrid scheme and the measured velocity around the particle can be used as input for the Stokes velocity field to impose on the boundary. Such implementation may be an interesting starting point to benchmark hybrid models in dynamics conditions.

Implementation of DSMC-derived heuristic model in Euler-Lagrangian Point Particles simulations: A relevant application of the results discussed in Chapters 5 and 6 consists in the use of the heuristic models for drag and lift coefficients, derived from DSMC simulations, to include shape and rarefaction effects in Euler-Lagrangian Point Particles simulations, typically employed in the industry to assess contamination from micro- and nano-metric particles. A practical example of such application is presented in Fig. 7.2, where micro-metric particles are released in a low pressure rectangular channel flow with an initial velocity opposed to the flow. The particle-based Knudsen number is $Kn_p \sim 1000$ and corrections to the drag force are in free-molecular regime. We then apply the heuristic models from Chapter 6 to correct the drag force (lift is neglected) experienced by the particles, mimicking the behavior of different oblate ellipsoidal particles with different aspect ratios and same volume.

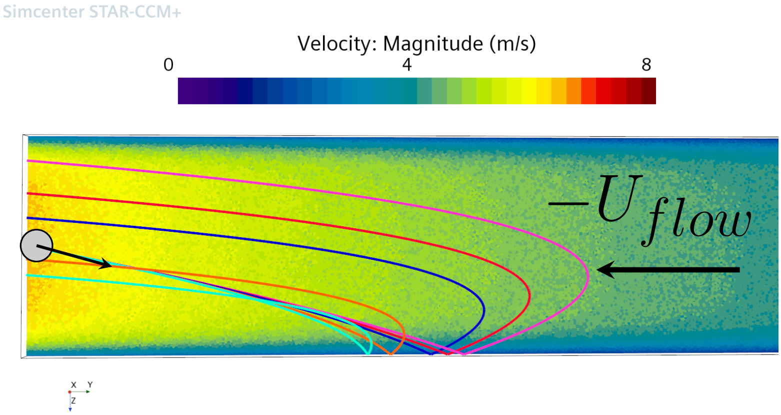

Figure 7.2: Simulation results of particle release in rectangular low-pressure Poiseuille flow with channel dimensions of $0.1m \times 0.01m \times 1m$. The flow is in the $-y$ direction and is generated by applying inlet and outlet pressures of 5 and 2 Pa, respectively. Particles are then released from the outlet center with a velocity of $(0, 5, 1)$m/s. Different shape and rarefaction corrections from Chapter 6 are applied to the drag coefficient of the particles, which undergo different trajectories (solid lines) depending on the applied corrections. We are simulating spherical (blue, and oblate particles with aspect ratios $a/b = 2$ (magenta), $a/b = 4$ (red), $a/b = 8$ (orange) and $a/b = 10$ (cyan). Particles are assumed to be always aligned with the relative velocity, so that only the drag correction relative $0°$ is applied. Elastic specular bouncing is imposed on contact with the solid walls. Note that only the last part of the channel (near the outlet) is included in the figure for better visibility of the trajectories of the particles.

For simplicity, we assume that particles are always aligned with the relative velocity. As it can be seen from the trajectories represented in Fig. 7.2, the dynamics of the particles can be greatly influenced when shape (and correct shape-related rarefaction effects) is included in the model. It is worth mentioning, however, that in the current state many physical parameters of great importance, such as particle rotation, effective orientation, bouncing on solid walls and lift effects, are neglected. The study of such effects and their inclusion in this framework is left for future studies.

Bibliography

[1] C. Wang, S.K. Friedlander, and Lutz Mädler. *China Particuology*, **3**(5):243, (2005).

[2] J. H. Seinfeld and S. N. Pandis. *Atmospheric Chemistry and Physics*. John Wiley and Sons, New York, (1998).

[3] F. Charles. *Modélisation mathématique et étude numérique d'un aérosol. Application à la simulation du transport de particules de poussière en cas d'Accident de perte de vide dans ITER*. PhD thesis, (2009).

[4] F. Doisneau, F. Laurent, A. Murrone, J. Dupays, and M. Massot. *J. Comput. Phys. (C)*, **234**:230, (2013).

[5] E. Ferrari and L. Pareschi. *J. Numer. Methods Fluids*, **57**(6):269, (2006).

[6] Georg Dettleff and Martin Grabe. Basics of plume impingement analysis for small chemical and cold gas thrusters, (2011).

[7] X. Fu, Y. Huang, L.Hu, H. Xie, and W. Chen. *Flow Meas. Instrum*, **53**:190, (2017).

[8] K. D. Cummings *et al.* In *Photomask Technology 2008*, volume **7122**, page 71222G. International Society for Optics and Photonics, SPIE, 2008.

[9] M. van de Kerkhof, E. Galutschek, A. Yakunin, S. Cats, and C.Cloin. In *Systems Contamination: Prediction, Control, and Performance 2020*, volume **11489**, page 114890K. International Society for Optics and Photonics, SPIE, 2020.

[10] C. Kleinstreuer, Z. Zhang ans Z. Li, W. L. Roberts, and C. Rojas. *Int J. heat Mass Transfer*, **51**:5578, (2008).

[11] C. A. Ruge, J. Kirch, and C. M. Lehr. *Lancet Respir. Med.*, **1**:402, (2013).

[12] C. C. Smutnew, M. Grant, and P. S. Kinsey. *Ther. Deliv.*, **4**:939, (2013).

[13] F. Torretti, J. Sheil, and R. Schupp *et al. Nat. Commun.*, **11**:2334, (2020).

[14] V. I. Azarov and N. Y. Joshi. *J. Phys. B: . Mol. Opt. Phys.*, **26**:3495, (1993).

[15] W. Svendsen and G. O'Sullivan. *Phys. Rev. A*, **50**:3710, (1994).

[16] S. S. Churilov and A. N. Ryabtsev. *Phys. Scr.*, **73**:614, (2006).

[17] I. Y. Tolstikhina, S. S. Churilov, A. N. Ryabtsev, and K. N. Koshelev. Euv sources for lithography, chap. 4, (2066).

[18] H. Ohashi *et al. J. Phys. B: . Mol. Opt. Phys.*, **43**:065204, (2010).

[19] F. Torretti *et al. Phys Rev. A*, **95**:042503, (2017).

[20] G. Di Staso. *Hybrid discretizations of the Boltzmann equation for the dilute gas flow regime*. PhD thesis, (2018).

[21] R. Glowinski. *Annu. Rev. Fluid Mech.*, **24**:167, (1992).

[22] M. Vinokur. *J. Comput. Phys.*, **81**:1, (1989).

[23] D. Burnett. *Proc. Lond. Math. Soc.*, **40**:382, (1936).

[24] H.S.Y. Zheng. *Cont. Mech. Thermodyn.*, **16**:97, (2004).

[25] M.S. Shavaliyev. *J. Appl/ Maths. Mechs.*, **57**:773, (1993).

[26] A.V. Bobylev. *Sov. Phys. Dokl.*, **27**:29, (1982).

[27] J. H. Seinfeld and S. N. Pandis. *Macroscopic transport equations for rarefied gas flows: Approximation methods in kinetic theory*. Heidelberg: Springer-Verla, (2005).

[28] M. R. A. Abdelmalik and E. H. van Brummelen. *J. Stat. Phys.*, **164**(1):77, (2016).

[29] M. R. A. Abdelmalik and E. H. van Brummelen. *Comput. Math. Appl.*, **72**(8):1988, (2016).

[30] M. R. A. Abdelmalik and E. H. van Brummelen. *Comput. Methods Appl. Mech. Eng.*, **325**:219, (2017).

[31] G. Di Staso, H.J.H. Clercx, S. Succi, and F. Toschi. *J. Comput. Sci.*, **17**:357, (2016).

[32] G. Di Staso, S. Srivastava, E. Arlemark, H.J.H. Clercx, and F. Toschi. *Comput. Fluids*, **72**:492, (2018).

[33] G.A. Bird. *Molecular gas dynamics and the direct simulation of gas flows*. Oxford: Clarendon University Press, (1994).

[34] C. Cercignani. *The Boltzmann Equation and its applicaitons*. Berlin: Springer, 1988.

[35] C. Cercignani. *Mathematical Methods in Kinetic Theory*. Plenum Press, 1990.

[36] C. Cercignani. *Rarefied gas dynamics*. Cambridge: Cambridge University Press, 2000.

[37] S. Succi. *The Lattice Boltzmann Equation for fluid dynamics and beyond*. Oxford University Press, (2001).

[38] S. Succi. *The Lattice Boltzmann Equation: For Complex States of Flowing Matter*. Oxford University Press, (2018).

[39] J. Liouville. *J. Math. Pures App.*, **3**:342, (1838).

[40] M. Born and H.S. Green. *Proc. Roy. Soc. A.*, **188**(1012):10, (1946).

[41] L. Boltzmann. *Sitzungsberichte der Akademie derWissenschafter*, **66**:275, (1872).

[42] W.F. Phillips. *Phys Fluids*, **18**:1089, (1975).

[43] Z. Guo, B. Shi, T. Zhao, and C. Zheng. *Phys. Rev. E*, **76**:056704, (2007).

[44] É. Guazzelli, J.F. Morris, and S. Pic. *A Physical Introduction to Suspension Dynamics*. Cambridge Texts in Applied Mathematics. Cambridge University Press, 2011.

[45] J. Happel and H. Brenner. *Low Reynolds Number Hydrodynamics*. Prentice-Hall, Englewood Cliffs, (1965).

[46] A. Oberbeck. *J. für die Reine und Angew. Math.*, **81**:62, (1876).

[47] G. B. Jeffery and L. N. G. Filon. *P. Roy. Soc. A-Math. Phy.*, **102**(715):161, (1922).

[48] S.K.P. Sanjeevi and J.T. Padding. *J. Fluid Mech.*, **820**:R1, (2017).

[49] S.K.P. Sanjeevi, J.A.M. Kuipers, and J.T. Padding. *Int. J. Multiph. Flow*, **106**:325, (2018).

[50] R. Narasimha. *J. Fluid Mech,*, **12**(2):294, (1962).

[51] J.C. Maxwell. *Phil. Trans. Soc.*, **157**:49, (1867).

[52] C. Cercignani. *Transp. Theory Stat. Phys.*, **2**(1):27–53, (1972).

[53] P.S. Epstein. *Phys. Rev.*, **23**(6):710, (1924).

[54] B.E. Dahnekë. *J. Aerosol Sci.*, **4**:147, (1972).

[55] C. Cercignani and A. Daneri. *J. Appl. Phys*, **9**:1764, (1997).

[56] W. D. Huang, D.B. Bogy, and A. L. Garcia. *Phys. Fluids*, **34**(6):3509, (1963).

[57] Y. Sone. *Phys. Fluids A*, **1**(363), (1989).

[58] T. Ohwada, Y. Sone, and K. Aoki. *Phys. Fluids A*, **1**(12):2042, (1989).

[59] S. Takata, Y. Sone, and K. Aoki. *Phys. Fluids A*, **5**:716, (1993).

[60] R. A. Millikan. *Phys. Rev.*, **23**:710, (1911).

[61] R. A. Millikan. *Phys. Rev.*, **22**:1, (1923).

[62] E. Cunningham. *Proc. R. Soc. Lond.*, **83A**:357, (1910).

[63] M. Knudsen and S. Weber. *Ann. Phys.*, **36**:981, (1911).

[64] Y. Ishida. *Phys. Rev.*, **21**:550, (1923).

[65] J. M. Eglin. *Phys. Rev.*, **22**:161, (1923).

[66] L. J. Lassalle. *Phys. Rev.*, **17**:354, (1921).

[67] K. S. Van Dyke. *Phys. Rev.*, **21**:500, (1923).

[68] D. J. Rader. *J. Aerosol Sci.*, **21**(2):161, (1989).

[69] M. D. Allan and O. G. Raabe. *Aerosol Sci. Technol.*, **4**:269, (1985).

[70] X. Xheng and Z. Silber-Li. *Appl. Phys. Lett.*, **95**:124105, (2009).

[71] X. Shen and D.B. Bogy. *J. Tribol.*, **125**:358, (2003).

[72] S. Zhang and D.B. Bogy. *Phys. Fluids*, **9**:1265, (1997).

[73] K. Zhang, H.-B. Xiong, and Z.-M. Shao. *J. Zhejiang Univ.-Sci. A*, **17**(9):733, (2016).

[74] O. Abouali, A. Nikbakht, G. Ahmadi, and S. Saadabadi. *Aerosol Sci. tech.*, **43**(3):205, (2009).

[75] B.E. Dahnekë. *J. Aerosol Sci.*, **4**:163, (1972).

[76] R. L. Buckley and S. K. Loyalka. *J. Aerosol Sci.*, **20**(3):347, (1989).

[77] H. Wang. *Ann. N. Y. Acad. Sci*, **1161**(1):484, (2009).

[78] R. M. MacMeccan, J. R. Clausen, G. P. Neitzel, and C. K. Aidun. *J. Fluid Mech.*, **618**:13, (2009).

[79] S. Melchionna. *Macromol. Theor. Simul.*, **20**, (2011).

[80] N. Nguyen and J. C. Ladd, A. *J. Fluid Mech.*, **525**:73, (2005).

[81] H. Haddadi, S. Shojaei-Zadeh, and J. F. Morris. *Phys. Rev. Fluids*, **1**:024201, (2016).

[82] M. Do-Quang, G. Amberg, G. Brethouwer, and A. V. Johansson. *Phys. Rev. E*, **89**(1):013006, (2014).

[83] A. T. Cate, J. J. Derksen, L. M. Portela, and H. E. A. Van Den Aakker. *J. Fluid Mech.*, **519**:233, (2004).

[84] L.-P. Wang, C. Peng, Z. Guo, and Z. Yu. *J. Fluids Eng.*, **138**(4):041306, (2015).

[85] O. B. Usta, J. E. Butler, and A. J. C. Ladd. *Phys. Fluids*, **18**(3):031703, (2006).

[86] H. Haddadi and D. Di Carlo. *J. Fluid Mech.*, **811**:436, (2017).

[87] W. Wagner. *J. Stat. Phys.*, **66**:1011, (1992).

[88] T. Krüger, H. Kusumaatmaja, A. Kuzmin, O. Shardt, G. Silva, and E. M. Viggen. *The Lattice Moltzmann Method, Principles and Practice*. Springer Cham, (2017).

[89] P.L. Bhatnagar, E.P. Gross, and M. Krook. *Phys. Rev.*, **94**:511, (1954).

[90] K. N. Premnath and J. Abraham. *J. Comput. Phys.*, 224(2):539, (2007).

[91] H. Chen R. Zhang, X. Shan. *Phys. Rev. E*, **74**:046703, (2006).

[92] S. Chapman. *Phil. Trans. R. Soc. A*, 216:279, (1916).

[93] S. Chapman. *Phil. Trans. R. Soc. A*, 217:115, (1917).

[94] D. Enskog. *Dissertation*, (1917).

[95] D. Enskog. *Arkiv Mat. Astr. Fys.*, 16, (1921).

[96] E. M. Viggen. *The Lattice Boltzmann method: fundamentals and acoustic*. PhD thesis, (2014).

[97] S. Chapman and T.G. Cowling. *The mathematical theory of non-uniform gases: an account of the kinetic theory of viscosity, thermal conduction and diffusion in gases*. Cambridge: Cambridge University Press, 3rd ed., (1970).

[98] H. Grad. *Commun. Pure Appl. Math.*, **2**:331, (1949).

[99] T. Shao, T. Chen, and R. Frank. *Math. Comp.*, **18**:598, (1964).

[100] C. Coreixas, G. Wissocq, G. Puigt, J.-F. Boussuge, and P. Sagaut. *Phys. Rev. E*, **96**, (2017).

[101] G. Pontrelli, A. Montessori, I. Halliday, M. Lauricella, S.V.Lishchuk, T. Spencer, and S. Succi. *Numerical Methods and Advanced Simulation in Biomechanics and Biological Processes*. Academic Press, (2017).

[102] G. Di Staso, H.J.H. Clercx, S. Succi, and F. Toschi. *J, Comput, Sci,*, **17**:357, (2016).

[103] I. Ginzbourg and P. M. Adler. *J. Phys. II France*, **4**:191, 1994.

[104] A.J.C. Ladd. *J. Fluid Mech.*, **271**:285, 1994.

[105] X. He, Q. Zou, L. S. Luo, and M. Dembo. *J. Stat. Phys.*, **87**:115, 1997.

[106] A. J. C. Ladd. *J. Fluid Mech.*, **271**:311, 1994.

[107] C. K. Aidun, Y. Lu, and E.-J. Ding. *J. Fluid Mech.*, **373**:287, (1998).

[108] B. Chun and A. J. C. Ladd. *Phys. Rev. E*, **75**:066705, (2007).

[109] P. Lallemand M. Buozidi, M. Firdaouss. *Phys. Fluids*, **13**(11):3452, (2001).

[110] P. Lallemand and L. Luo. *J. Comput. Phys.*, **184**:406, (2003).

[111] D. d'Humières I. Ginzburg. *Phys. Rev. E*, **68**:066614, (2003).

[112] P.-H. Kao and R.-J. Yang. *J. Comput. Phys.*, **227**(11):5671, (2008).

[113] J. Wu and C.K. Aidun. *Int. J. Numer. Meth. Fluids*, **62**:765–783, (2010).

[114] D. Goldstein, R.Handler, and L.Sirovich. *J. Comput. Phys.*, **105**(2):354–366, (1993).

[115] X.D. Niu, C. Shu, Y.T. Chew, and Y. Peng. *Phys. Lett. A*, **354**:173, (2006).

[116] C.S. Peskin. *J. Comput. Phys.*, **25**:220, (1977).

[117] C. Peng, O. M. Ayala, and L.-P. Wang. *Comput. Fluids*, **192**:104233, (2019).

[118] E. Haines T. Akenine-Möller. *Real-Time Rendering*. A K Peters, (2002).

[119] E. P. Muntz. *Ann. Rev. Fluid. Mech.*, **21**:387, 1989.

[120] G. A. Bird. *J. Fluid. Mech.*, **30**:479, 1967.

[121] M. S. Ivanov and S. V. Rogasinsky. *Sov. J. Numer. Anal. Math. Modelling*, **2**:453, 1988.

[122] S. K. Stefanov. *SIAM J. Sci. Comput.*, **33**:677, 2011.

[123] A. L. Garcia. *Numerical Methods for Physics (2nd Edition)*. Prentice-Hall, Inc., USA, 2nd edition, (1999).

[124] N. G. Hadjiconstantinou, A. L. Garcia, M. Z. Bazant, , and G. He. *J. Comput. Phys.*, **187**:274, 2003.

[125] W. Jin, J.R. Ommen, and C.R. Kleijn. *Comput. Phys. Commun*, **212**:146, (2017).

[126] C. Kleinstreuer and Y. Feng. *J. Biomech. Eng.*, **135**(2):021008, (2013).

[127] P. Sharma and M. Khare. *Transp. Res. D*, **6**(3):179, (2001).

[128] T.D. AlMomani, S.C. Vigmostad, V.K. Chivukula, L. Al-zube, O. Smadi, and S. BaniHani. *Crit. Rev. Biomed. Eng.*, **5**(40):427, (2012).

[129] A. K. Bates, M. Rothschild, T. M. Bloomstein, T. H. Fedynyshyn, R. R. Kunz, V. Liberman, and M. Switkes. *IBM J. Res. Dev.*, **45**(5):605, (2001).

[130] N. van Doremalen, T. Bushmaker, D. H. Morris, M. G. Holbrook, A. Gamble, B. N. Williamson, A. Tamin, J. L. Harcourt, N. J. Thornburg, S. I. Gerber, J. O. Lloyd-Smith, E. de Wit, and V. J. Munster. *N. Engl. J. Med.*, **382**(16):1564, (2020).

[131] S. Asadi, N. Bouvier, A. S. Wexler, and W. D. Ristenpart. *Aerosol Sci. Tech.*, **54**(6):635, (2020).

[132] C. K. Aidun and J. R. Clausen. *Annu. Rev. Fluid Mech.*, **42**(1):439, (2010).

[133] L.P. Wang, C. Peng, Z. Guo, and Z. Yu. *Comput. Fluids*, **124**:226, (2016).

[134] H. Brenner J. Happel. *Low Reynolds number hydrodynamics*. Mechanics of Fluids and Transport Processes. Springer Netherlands, 1983.

[135] T. Krüger, F. Varnik, and D. Raabe. *Phys. Rev. E*, **79**(4):046704, (2009).

[136] M. S. Ingber and L. A. Mondy. *J. Rheol.*, **38**(6):1829, (1994).

[137] H. Huang, Y. Wu, and X. Lu. *Phys. Rev. E*, **86**(4):046305, (2012).

[138] J. Feng, H. H. Hu, and D. D. Joseph. *J. Fluid Mech.*, **261**:95–134, (1994).

[139] H.H. Hu, D.D. Joseph, and M.J. Crochet. *J. Fluid Mech.*, **3**:285–306, (1992).

[140] J. Feng, H. H. Hu, and D. D. Joseph. *J. Fluid Mech.*, **277**:271–301, (1994).

[141] H. Li, X. Lu, H. Fang, and Y. Qian. *Phys. Rev. E*, **70**:026701, (2004).

[142] B. Wen, C. Zhang, Y. Tu, C. Wang, and H. Fang. *J. Comput. Phys.*, **266**:161–170, (2014).

[143] C. K. Aidun and E-J. Ding. *Phys. Fluids*, **15**:1612, (2003).

[144] C. Zettner and M. Yoda. *Exp. Fluids*, **30**:346–353, (2001).

[145] E-J. Ding and C. K. Aidun. *J. Fluid Mech.*, **423**:317–344, (2000).

[146] A. Haider and O. Levenspiel. *Powder Technol.*, **102**(715):161, (1922).

[147] G.H. Ganser. *Powder Technol.*, **2**(143):161, (1993).

[148] A. Hölzer and M. Sommerfeld. *Comput. Fluids*, **3**(38):572, (2009).

[149] M. Zastawny, G. Mallouppas, F. Zhao, and B. Van Wachem. *Int. J. Multph. Flow*, **39**:227, (2012).

[150] P.A. Nikrityuk A. Richter. *Powder Technol.*, **249**:463, (2013).

[151] R. Ouchene, A. Taniere, and B. Arcen. *Comput. Fluids*, **13**:53, (2015).

[152] C. Livi, G. Di Staso, H. J. H. Clercx, and F. Toschi. *Phys. Rev. E*, **103**:013303, (2021).

[153] S. Zhang and D.B. Bogy. *Phys. Fluids*, **9**:1265, (1997).

[154] V.C Liu, S.C. Pang, and H. Jew. *Phys. Fluids*, **8**:788, (1965).

[155] M.J. Baines, I.P. Williams, A.S. Asebiomo, and R.L. Agacy. *Mon. Not. R. Astron. Soc.*, **130**(1):63, (1965).

[156] M.A. Gallis, J.R. Torczynski, and D.J. Rader. *Phys. Fluids*, **13**:3482, (2001).

[157] M.A. Gallis, D.J. Rader, and J.R. Torczynski. *Aerosol Sci. Tech.*, **36**(12):1099, (2002).

[158] L. Lees. *J. Soc. Indust. Appl. Math.*, **13**(1):278, (1965).

[159] L. Lees and C.Y. Liu. *Phys. Fluids*, **5**(10):1137, (1962).

[160] J. Halbritter. *Z. Naturforsch.*, **29a**:1717, (1974).

[161] S.K. Stefanov. *Phys. Fluids*, **31**:067104, (2019).

[162] G. Karniadakis, A. Beskok, and N. Aluru. *Microflows and Nanoflows. Fundamentals and Simulation*. New York: Springer-Verlag, (2005).

[163] M. Reese, M.A. Gallis, and D.A. Lockerby. *Phil. Trans. R. Soc. Lond. A*, **361**:2967, (2003).

[164] R. Wilmoth, A. Carlson, and G. LeBeau. *AIAA Meeting Papers on Disc.*, **96**:1812, (1996).

[165] G.J. LeBeau. *Comput. Methods. Appl. Mech. Engrg.*, **174**:319, (1999).

[166] C. Zhang and T.E. Schwartzentruber. *Comput. Fluids*, **69**:122, (2012).

[167] J.M. Burt, E. Josyula, and I.D. Boyd. *J. Thermophys. Heat Transfer*, **26**:258, (2012).

[168] S. Shrestha, S. Tiwari, A. Klar, and S. Hardt. *J. Comput. Phys.*, **292**:239, (2015).

[169] T. Baier, S. Tiwari, S. Shrestha, A. Klar, and S. Hardt. *Phys. Rev. Fluids*, **3**:094202, (2019).

[170] A.K. Chinnappan, R. Kumar, V.K. Arghode, and R.S. Myong. *Phys. Fluids*, **31**:037104, (2019).

[171] I.N Ivchenko, S.K. Loyalka, and R.V. Tompson Jr. *Analytical Methods for Problems of Molecular Transport*. Fluid Mechanics and Its Applications. Springer Netherlands, (2007).

[172] S. tao, H. Zhang, and Z. Guo. *J. Aerosol Sci.*, **103**:105, (2017).

[173] S. J. Plimpton, S.G. Moore, and A. Borner. *Phys. Fluids*, **31**:086101, (2019).

[174] R. Ouchene, , M. Khalij, B. Arcen, and A. Taniere. *Powder Technol.*, **303**:33, (2016).

[175] L. Schiller and A.Z. Naumann. *Ver. Deut. Ing.*, **77**:318, (1933).

[176] F. Bernard, A. Iollo, and G. Puppo. *Eur. J. Mech. B/Fluids.*, **63**:25, (2017).

[177] Tadd R. Yeager, Douglas H. Fontes, Philip Metzger, and Michael P. Kinzel.

[178] Y. Feng *et al. J. Aerosol Sci.*, **123**:185, (2018).

[179] P. Spijker, A. J. Markvoort, S. V. Nedea, and P. A. J. Hilbers. *Phys. Rev. E*, **81**:011203, (2010).

[180] T. Liang, Q. Li, and W. Ye. *Phys. Rev. E*, **88**:013009, (2013).

[181] D. Kalempa and F. Sharipov. *J. Fluid. Mech.*, **900**:A37, (2020).

[182] P. Goswami, T. Baier, S. Tiwari, C. Lv, S. Hardt, and A. Klar. *J. Fluid Mech*, **883**:A47, (2020).

[183] R.G. Cox. *J. Fluid Mech.*, **23**:625, (1965).

[184] L.G. Leal. *J. Fluid Mech.*, **69**:305, (1975).

Curriculum Vitae

Cosimo Livi was born on 20-07-1989 in Bagno a Ripoli, Italy.
After finishing the Scientific High School in 2009 at Liceo Scientifico Amedeo Di Savoia Duca D'Aosta in Pistoia, Italy, he studied Physics at University of Pisa, Italy. In 2013 he graduated at the Bachelor program and continued his studies by completing, in 2016, the Master in Physics within the group of Andrea Macchi on Laser Acceleration of ultra-thin foils. After his first Master, in 2018 he also obtained a second Master in High Performance Computing at the International School for Advanced Studies in Trieste, Italy. From 2018 he started a PhD project at the Eindhoven University of Technology, the Netherlands, of which results are presented in this dissertation. Since 2021 he is employed as Design Engineer in the Flow Modelling group at ASML.

List of publications and conferences

This thesis is based on the following publications

- C. Livi, G. Di Staso, H. J. H. Clercx and F. Toschi. Influence of numerical resolution on the dynamics of finite-size particles with the lattice Boltzmann method, *Phys. Rev. E* **103**, 013303, 2021. **(Chapter 4)**
- C. Livi, G. Di Staso, H. J. H. Clercx and F. Toschi. Drag and lift coefficients of ellipsoidal particles under rarefied flow conditions, *Phys. Rev. E* **105**, 015306, 2022. **(Chapter 5)**
- C. Livi, G. Di Staso, H. J. H. Clercx and F. Toschi. Modelling drag coefficients of ellipsoidal particles in rarefied flow conditions, *Submitted to Phys. Rev. E.* **(Chapter 6)**

Conferences contributions

- C. Livi, G. Di Staso, H. J. H. Clercx and F. Toschi. Talk: Resolution analysis of particle transport dynamics for the Lattice-Boltzmann Method. 72nd Annual Meeting of the APS Division of Fluid Dynamics, Seattle, Washington, USA, November 2019.
- C. Livi, G. Di Staso, H. J. H. Clercx and F. Toschi. Talk: Derivation of a predictive model for drag and lift on ellipsoidal particles from DSMC simulations. 73rd Annual Meeting of the APS Division of Fluid Dynamics, Virtual, November 2020.
- C. Livi, G. Di Staso, H. J. H. Clercx and F. Toschi. Talk: Derivation of a predictive model for drag and lift on ellipsoidal particles from DSMC simulations. 74th Annual Meeting of the APS Division of Fluid Dynamics, Phoenix, Arizona, USA, November 2021 (Virtual participation).
- C. Livi, G. Di Staso, H. J. H. Clercx and F. Toschi. Poster: Analysis of resolution effects on the dynamics of finite-size particles with the Lattice-Boltzmann Method. Physics@Veldhoven 2020, Veldhoven, The Netherlands, January 2020.

Acknowledgments

The Ph.D. years have been among the most intense and fruitful years of my life, also thanks to the guidance I have received and the examples I have met, professionally and not, during this journey.

First of all, I would like to thank my supervisor Federico Toschi, who invited me to join his team after an informal meeting in Trieste, which changed my life. I accepted his proposal and moved out of Italy for the first time to the Netherlands. Apparently, I liked it here as I am still here after almost six years and enjoying my job and career in ASML as Design Engineer. Federico not only launched my career in the field of gas modeling, but inspired me with intelligent ideas and smart solutions while encouraging me to develop my own way of thinking and independence. I clearly see now the fruit of our collaboration, and I am grateful for having had this opportunity; thank you! The second person I would like to thank is Herman, my second supervisor. Herman, you, more than anyone else, helped me develop sharp writing and thinking which pushed my research to a higher level. Additionally, you supported me in the most critical times of the PhD, where felt overwhelmed, and motivated me to keep pushing.

I would like to thank Gianluca Di Staso, whose expertise and knowledge remain a model to follow as our collaboration continues in our current jobs. Thank you, Gianluca, for the precious feedback, discussions and insights that I continue to receive from you, I hope there will be many more in the future!

My appreciation extends to the members of my committee, Alejandro Garcia, Alexey Lyulin, Harald van Brummelen and Chris Kleijn, for reading and evaluating my thesis.

To the colleagues and former colleagues from the Fluid and Flows group: Abheeti, Alessandro, Arnab, Andrés, Felix, Gianmarco, Giorgia, Haijing, Hanneke, Jonathan, Karun, Kim, Lenin, Maarten, Marjan, Matteo, Matias, Ralf, Rik, Rudie, Samuel, Steven, Vignesh and Xiao. Thank you for contributing to the great vibe that the office had!

Andres, Jonathan and Laura, thank you for the amazing adventures we had together, which contributed to making this experience unforgettable. Our crazy climbing expeditions with a van full of people (and a dog) are, for sure, among the best memories of this entire time. Jonathan, I hope we will meet again soon! Laura, we started the Ph.D. about the same time, and soon you became one of my closest friend out of Italy. Your appreciation of life always fills me with positive energy and we really had amazing times, from the Taiji lessons (that you actively contributed to create by motivating me to teach) to the salsa and techno parties, up until the aforementioned adventures with the van. Thank you for all this!.

I want to thank my Italian friends John, Kekko, Lorenzo, James, Gianmarco and Omar. You surely are the lifetime friends one can only hope for, and an example of intelligence and passion. It is literally impossible to recall all the adventures we had together and it is a gift for me to come back to Italy and meet you like if I was never abroad. Omar, John, now that you also live abroad, our chances to meet are much lower; we need to find a solution to that.

A special mention goes to my girlfriend, Adriana. You were with me for almost all this journey and supported me from within the domestic walls. My successes could not have been achieved without your kindness and love, and I am really grateful I have such an exceptional partner. We had (and still have, and, I am sure, will keep having) so much fun together that sometimes you make me forget all the difficult parts of life. From parties together to our ultra-adventurous travels (Iceland on top), on-the-road and skiing trips (where I finally managed to learn how to sky), you make my life exceptional, and I can't thank you enough for this. During COVID, you also allowed me to stay with you in Ghent, which soon became my favorite city of the Benelux. There I met Bianca, Lorenz, Nuria, Jindirch, Dani, José and all the rest of the Belgian crew. Thank you guys for the amazing times we spent together, looking forward to meeting you all again soon.

To my parents, Angela e Marcello, thank you for your endless guidance, patience, kindness, creativity and faith. I shall be forever indebted with you for always being there for me, encouraging me with words of wisdom in the darkest moments and for having given me the best possible education I could receive. Family is not just mother and father, and I would like to thank Alessandra, for all the kindness she gives not only to me, but to the whole family, and Virginia and Martina for being the most lovely acquired sisters I could have possibly desired. Thank you all for making my life exceptional!